Final report

1. Project details

Project title	EUDP 12-I,Avanceret sol-ressource vurdering og vejrvarsling (*English title: Advanced solar resource assessment and forecasting)*
Project identification (program abbrev. and file)	EUDP 64012 – 0136
Name of the programme which has funded the project	EUDP (60.74%); DMI (32.35%); DTU (6.91%)
Project managing company/institution (name and address)	Danmarks Meteorologiske Institut (DMI) Lyngbyvej 100, 2100 Kbh. Ø
Project partners	DMI DTU Civil Engineering (DTU Byg)
CVR (central business register)	DMI: 18159104 DTU Byg: 30060946
Date for submission	2016-03-30

2. Short description of project objective and results

Advanced solar resource assessment and forecasting is necessary for optimal solar energy utilization. This work has been done in the framework of the IEA SHC Task 46 expert group, and has been based on a focused analysis of both historic and new detailed measurements, and the newest theoretical models for modelling solar resources.

2.1. Kort beskrivelse af projektets formål og resultater (på dansk)

Avanceret sol-ressource vurdering og vejr-varsling er nødvendigt for optimal udnyttelse af alle former for solenergi. Dette arbejde er gjort i dialog med partnere i IEA SHC Task 46 ekspert gruppen, der er fokuseret på disse emner. Projektet inkluderer både historiske og nye målinger og modellering med de nyeste teoretiske modeller.

3. Executive summary

This project is an international collaboration project. Specifically it is the Danish contribution to the International Energy Agency (IEA) Solar Heating and Cooling Programme (SHC) Task 46: "Solar Resource Assessment and Forecasting". It has had two major goals: 1) To understand short-term resource variability caused by clouds; 2) To assess the application of short term forecasts for planning the operation of multiple solar energy systems.

The concrete deliverables consist of:

- The solar irradiance platform at DTU Byg has been upgraded with directional measurements of solar irradiances from 16 directions simultaneously with 1 minute resolution. Several challenges with ensuring the quality of these measurements occurred. This was finally complete in the second half of 2014, since when good quality measurements have

made from 8 azimuthal directions covering 1/8th of the sky each. Since March 2015 data have been gathered from all 16 instruments where the additional 8 measure the upper 1/16th fractions of the sky.

- A parametrization of directional irradiances from across the sky has been made. This is used to expand the Danish Design Reference Year (DRY) data sets based on data from 2001-2010.
- An analysis of the impact of simulating the performance of solar collectors with long-term data sets has been made. This includes also the "untypical" months that are not included in DRY data sets, and is done for 6 Danish and 3 Greenlandic stations. It shows the short-comings of using typical single year data sets such as the DRY data set.
- Methods for estimating the potentially available solar resources at the surface from satellite images have been tested. These images are taken once every 15 minutes with the SEVIRI instrument onboard the Meteosat second generation geostationary satellite (MSG). They have a spatial resolution of 6-7 km for the Danish area. Tests show that the images therefore cannot capture the effects of fractional cloud cover on the solar resource.
- Theoretical investigations have been made at DMI of both the directional and spectral distributions of the solar irradiances. Less focus have been on these, since the empirical directional data were prioritized, and since the weather model benchmarking was a more general focus in the Task 46 group.
- Benchmarking of global radiation as forecast with Danish, German and international weather prediction models has been performed in framework of the Task 46 expert group. This benchmarking quantifies the uncertainty of both global and regional weather models as a function of the forecast length. As a novelty intra-daily resource variability has also been benchmarked against the measured variability.
- At DMI work has progressed with assimilation clouds in the rapid-update cycle (RUC) HIRLAM weather model. This is now run once every hour and gives output with 10 minute resolution. For the first 6 hours the global radiations forecasts are significantly improved as compared with the standard HIRLAM weather model.

3.1. Executive summary (på dansk)

Dette projekt er et internationalt samarbejdsprojekt. Mere specifikt er det det danske bidrag til det Internationale Energi Agenturs (IEA) "Solar Heating and Cooling Programme (SHC) " Task 46, der handler om sol-ressource-vurderinger og -vejrudsigter. Det internationale projekt har to overordnede mål: 1) At øge forståelsen af variabiliteten af sol-ressourcen på korte tidsskaler (minutter) pga. fraktionelle skyer; 2) At vurdere usikkerheden og variabiliteten i prognoser af globalstråling og betydningen af disse for driften af grid med flere sol-energi kilder.

De konkrete leverancer fra vores projekt er:

- Ved DTU Byg er klimastationen blevet udbygget med nyudviklede retningsbestemte pyranometre. 16 af disse er blevet bygget og måler nu retningsbestemte sol-irradianser med 1 minuts opløsning fra 16 himmelretninger samtidigt. Det var mange udfordringer ved få disse nye målere til at virke korrekt og kvalitetssikre dataene. Disse var løst fra og med anden halvdel af 2014. Siden da har vi taget målinger fra 8 azimut-retninger, der hver dækker 1/8 af himlen. Siden marts 2015 er kvalitetssikrede målinger blevet lavet fra alle 16 instrumenter. Heraf måler de sidste 8 de øvre 1/16 af himlen.
- Parameteriseringer af de direktionelle irradianser fra et helt års målinger er blevet lavet. Disse er brugt til at udvide de danske Design Referenceår (DRY), der er baseret på data fra 2001-2010.
- Vi har undersøgt betydningen af af bruge langtids (mange år) meteorologisk datasæt til at simulere ydelsen fra solvarme-anlæg. Langtids-simuleringerne inkludere også "utypiske" måneder, der er udeladt fra DRY datasættene. Disse analyser er blevet gjort for 6 danske stationer og 3 grønlandske stationer. De viser begrænsninger i at udføre tests kun baseret på DRY datasættene.

- Metoder til estimering af de potentielt tilgængelige sol-ressourcer ud fra satellit-billeder er blevet afprøvet. Vi har brugt satellit-billeder fra Meteosat Second Generation (MSG) satelliterne, der bliver taget hvert 15. minut. De har en rumlig opløsning på 6-7 km for det danske område. Dette gør, at man ikke kan opløse fraktionelt skydække og den betydelige effekt, som dette har på sol-ressourcen og variabiliteten af denne.
- Teoretiske undersøgelser ved DMI af både retnings- og spektral-fordelingen af sol-irradianserne er blevet foretaget. Dette er gjort vha. detaljerede strålingstransport-beregninger for en antaget horisontalt ensartet atmosfære. Det er blevet vist, at denne antagelse ikke passer overens med de empiriske data fra DTU's målestation i alle tilfælde. Igen er det især det fraktionelle skydække, der er udfordringen.
- Usikkerhederne af globalstrålingen, som forudsagt med flere forskellige numeriske vejr-modeller, er blevet testet op mod målinger fra flere europæiske lande. Dette er blevet gjort i bredt regi i Task 46 ekspert-gruppen. Usikkerhederne og hvordan disse øges med længden af prognosen er blevet kvantificeret for flere globale og regionale vejr-modeller. Som noget nyt er den prognosticerede variabilitet i løbet af dagen i forhold til den målte variability også blevet testet.
- Ved DMI er den forsatte udvikling af den såkaldte rapid-update cycle (RUC) HIRLAM vejr-model blevet koblet op mod projektet. Fokus er i denne forbindelse på bedre assimilering af skydata. RUC-modellen køres nu 1 gang i timen og giver output af både globalstråling og diffuse irradianser med 10 minutters opløsning. I løbet af de første 6 timer af prognosen er RUC-modellens prognoser af globalstråling klart bedre end den almindelige HIRLAM model's prognoser.

4. Project objectives

The project objectives and milestones have overall been achieved. When it comes down to each of the specific workpackages, some of these have been prioritized during the course of the project. This regards in particular the measurements (WP3) and the analysis of these (WP7), and the weather model verification (WP10).

One major issue occurred when DTU with short noticed decided to renovate the building that houses the measurement platform. This had to be taken down for several months and re-wired for newly installed controlling equipment. This delayed our measurements and caused a gap in these. We are thankful to the EUDP project agency for prolonging our project with 6 months in this regard.

5. Project results and dissemination of results

Our results have been (and will be) reported in the annual and semi-annual SHC Task 46 reports. This is scheduled to end in 2016 and the final report will be published at the end of 2016 or in 2017. The weather model verification results from DMI are used in the more detailed mid-term report: "Best Practices Handbook for the Collection and Use of Solar Resource Data for Solar Energy Applications" that was published by NREL (Golden, CO 80401, USA) in 2015. Our results have also been published in peer-review journals and presented at conferences such as: The International Conference on Solar Heating and Cooling for Buildings and Industry, and the Annual Meeting of the European Meteorological Society. We have also presented our results at smaller meetings in Denmark when possible. Many of the peer-review publications are still going through review, which can be a lengthy process. Thus, these will be published also in 2016 and 2017.

A dedicated project website has been made: irradiance.dmi.dk. At this automatically updated, forecast verifications, directional irradiance measurements from the DTU Byg platform, and near real-time satellite derived data can be seen.

6. Utilization of project results

The DRY data set is widely used by research institutes and companies throughout the country for simulating solar energy systems and buildings. Our updates for this data set and our suggestion of using long-term data sets for large-scale designs are likely to be used widely also.

Similarly, DMI's weather forecasts are used by several companies for solar resource forecasting. With our improvements and recommendations, we expect this use to grow and to be done in a better fashion.

Better solar resource assessment in Denmark overall becomes more important as the implementation of solar energy systems in the country grows. Given the grid couplings to Northern Germany forecasting of solar energy production in this region is also important, in particularly with regards to the photovoltaic electricity production.

7. Project conclusion and perspective

We have (at DTU Byg) successfully managed to build an irradiance monitoring system with which the directional distributions of solar irradiances across the sky can be monitored with high temporal resolution (1 minute). We have used these data to expand the current Design Reference Year (DRY) data sets with directional irradiance information. Much more can be learned from these data over the coming years that is important for the solar resource assessment in fractional cloud cover cases.

With new methods for quantifying the uncertainty in numerical weather forecasts, we have (at DMI) highlighted the need for further improvements that should be made to these forecasts. In particular, both hourly and daily cloud forecasts should be improved.

We have done theoretical work on spectrally resolved solar irradiances. Given the importance of this for photovoltaic systems, this work should be expanded.

Solar resource assessment and forecasting in Denmark - EUDP project 64012-0136

Kristian Pagh Nielsen[1]
Elsa Andersen[2]
Janne Dragsted[2]
Claus Pedersen[1]
Peter Thejll[1]
Simon Furbo[2]

1) Danish Meteorological Institute (DMI), Department of Research and Development, Lyngbyvej 100, 2100 København Ø.
2) The Technological University of Denmark, Department of Civil Engineering, Brovej 119, 2800 Kgs. Lyngby.

Content

Nomenclature

I_d	horizontal diffuse irradiance at the surface, (W/m^2)
DfHI	horizontal diffuse irradiance abbreviation, (W/m^2)
I	global horizontal irradiance at the surface, (W/m^2)
GHI	global horizontal irradiance abbreviation, (W/m^2)
I_b	direct horizontal irradiance, (W/m^2)
DrHI	direct horizontal irradiance abbreviation, (W/m^2)
DNI	direct normal irradiance abbreviation, (W/m^2)
ρ	clear sky index: GHI relative the GHI in theoretical clear sky conditions, (-)
K_T	clearness index: GHI relative to the GHI above the atmosphere, (-)
μ_o	cosine of the solar zenith angle, (-)
SZA	solar zenith angle abbreviation, (°)
S_o	solar constant adjusted for Earth-Sun distance, (W/m^2)
SA	solar azimuth angle abbreviation, (°)
DA	dome center azimuth angle abbreviation, (°)

1. Installation and test of pyranometers

This section describes the work carried out in WP2: 'Installation and test of pyranometers'.

Here the experimental set-up used to investigate how the diffuse solar irradiance is distributed across the sky is described.

The investigation is carried out by means of 16 individual horizontal pyranometers measuring solar irradiances from 16 different parts of the sky.

The fractional measurements are compared to measurements of the global horizontal irradiance (GHI).

The measurements are carried at the climate station at DTU Byg in Lyngby Denmark. The latitude and longitude of the installation are 55.8 N and 12.5 E respectively.

1.1 Measurement equipment

All the instruments used in this investigation are high quality instruments from the company Kipp and Zonen. The instrument are:

- 16 pyranometers, type CMP 11 used for measuring horizontal irradiance from different parts of the sky
- A sun tracker, type SOLYS 2 including a pyrheliometer, type CHP 1 for measuring direct normal irradiance, a CMP 11 for measuring the horizontal diffuse irradiance (DfHI) and a sun sensor that fine tunes the tracking perfectly
- 1 pyranometer type CM 11 for measuring the GHI

The data acquisition equipment is from the company National Instruments and comprises a compactRIO control and monitoring system and I/O modules of the type NI9214 for voltage measurements.

The measurement instruments are connected to the data acquisition equipment by long unbroken cables. The cables are twisted pairs with 80% braid coverage. The data logger is placed in an Electromagnetic Compatibility, EMC cabinet. All connections are carried out with shielded plugs. In this way electrical noise from the surrounding, cannot disturb the measurements.

Table 1.1 shows data of the high resolution instruments and data acquisition equipment used for the investigation of the diffuse irradiance distribution over the entire sky dome.

Table 1.1 Data of instruments and data acquisition equipment.

Parameter	Type	Resolution	Response time	Accuracy
Pyranometer	CMP 11	0.1 W/m^2	< 5 seconds	1.4 %
Pyranometer	CM 11	0.1 W/m^2	< 5 seconds	1.4 %
Pyrheliometer	CHP 1	0.1 W/m^2	< 5 seconds	1 %
I/O module	NI9214	-	< 1 second	8 µV ≈ 1 W/m^2

1.2 Experimental setup

Figure 1.1 shows a picture of the climate station. Along the circumference of climate station, the 16 individual pyranometers that measure horizontal solar irradiances from 16 different parts of the sky can be seen. The sun tracker is located in the north-west corner and can therefore not be seen in the picture.

Figure 1.1: The climate station at the Technical University of Denmark. Latitude: 55.6°N. Longitude: 12.5°E.

Figure 1.2 shows pictures of the sun tracker and the measurement equipment mounted on the tracker. The tracker has an integrated GPS receiver that allows the tracker to automatically determine its location and the time and operate according to this. The tracker also makes use of a solar sensor that fine tunes the tracking perfectly. The refraction is taken into consideration by the tracker when the geometric solar altitude is between 0°-25° by means of the Michalsky algorithm (Michalsky 1988; Reda & Andreas 2004, 2007). Hence, the tracker follows the visible sun when the geometric solar altitude is between 0°-25°. The tracker is further equipped with a shading ball assembly used for DfHI measurements.

The pyranometer used to measure the DfHI is mounted on the top plate on the tracker. The shadow ball screens of the beam irradiance and the pyranometer measures only the DfHI. The pyrheliometer that measures the direct normal irradiance is mounted on the left side of the tracker. The view angle from the pyrheliometer to the sky is 5° and the view angle from the pyranometer to the shadow ball is 5°. In this way, the pyrheliometer measures the amount of solar irradiance that is screened of by the shadow ball. Here we define the view angle as the total angle. Thus, the half-angle aperture is 2.5°.

Figure 1.2: The SOLYS 2 tracker. On the top mounting plate, the pyranometer that measures the DfHI can be seen. On the left side of the tracker, the solar sensor and the pyrheliometer that measured the beam normal irradiance can be seen. Below the pyrheliometer, the solar sensor can be seen.

The 16 pyranometers are mounted along the circumference of the climate station. Domes are mounted over each pyranometer with dome openings that form only a fraction of the sky.

8 of the domes have 45° openings from horizon to zenith, corresponding to 1/8 of the sky. 8 of the domes have 45° openings but only viewing from about 45° to zenith, corresponding to the upper 1/16 of the sky, see figure 1.7. The domes all point in different directions. Consequently, fractional solar irradiance is received from the whole sky dome.

Figure 1.3 shows a top view of the climate station with the domes. The pyranometers are inside the domes and cannot be seen in the figure. In the north-west corner of the climate station the sun tracker is located.

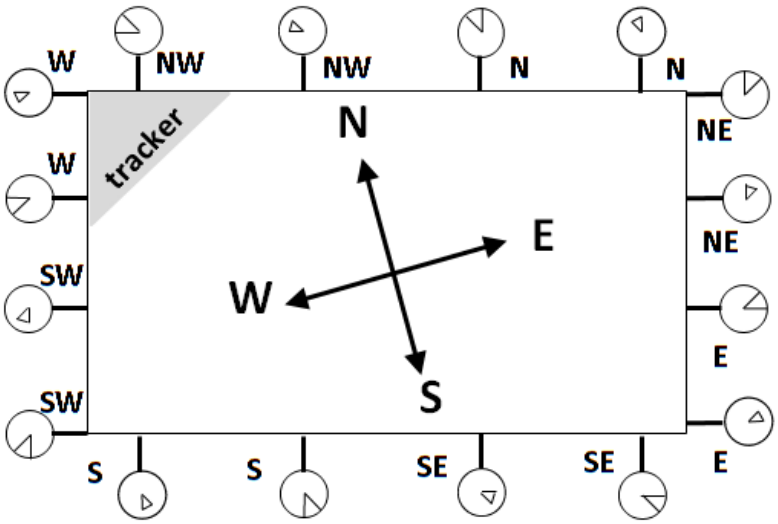

Figure 1.3: Top view of the domes with different opening areas and different orientation along the circumference of the climate station.

Figure 1.4 shows top views of the orientation of the domes with 1/16 opening area and the domes with 1/8 opening area. Left: top view of the domes with 1/16 opening area and the orientation of the different dome openings. Right: top view of the domes with 1/8 opening area and the orientation of the different dome openings. The top view figures show the azimuth angles of the different opening where -90°=East, 0°=South, 90°=West, ±180°=North. The domes with 1/16 opening areas are not oriented as precise as the domes with 1/8 opening areas and some overlaps between the different dome openings are seen.

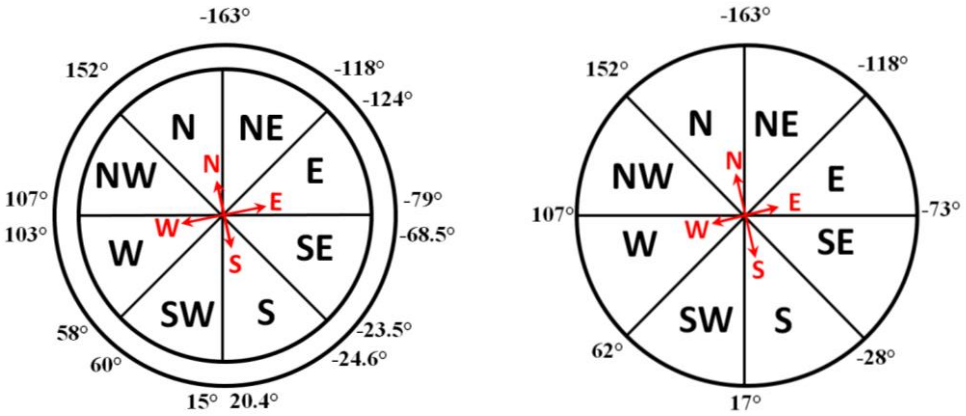

Figure 1.4: Left: top view of the domes with 1/16 opening areas and the orientation of the different dome openings. Right: top view of the domes with 1/8 opening areas and the orientation of the different dome openings.

Figure 1.5 shows the experimental set-up with a dome with opening area corresponding to 1/8 part of the sky mounted over a pyranometer. The dome is held in position with a metal plate with multiple holes which allows for good ventilation inside the dome. The domes are made of acrylic. The domes are painted shiny white on the outside in order to reflect the solar irradiance and thereby avoid heating. On the inside, the domes are painted black with a deep-black optical paint with a low reflectance. The metal plate is painted with the same paint as the inside of the dome. The reflection from the black paint is < 5%. Black felts fabric covers the gap between the metal plate and the pyranometer in the center of the set-up. In this way, the interior is all black.

Figure 1.5: Experimental set-up with a pyranometer and a dome with 1/8 opening.

Figure 1.6 shows pictures of the two kinds of domes used. Left picture shows the dome with an opening corresponding to 1/8 part of the sky and right picture shows the dome with an opening corresponding to 1/16 part of the sky (before the dome was painted).

Figure 1.6: Left: dome with 1/8 opening area. Right: dome with 1/16 opening area.

Figure 1.7 shows the geometry of the dome with 1/16 opening area. The domes are half balls. The inner radius is 145.6 mm. The dome material thickness is 2.9 mm. The geometry result in the angles α_1 and α_2 being 28.3° and 42.3° respectively. The angle α_1 correspond the solar elevation angle where rays from the sun disc starts to shine on the pyranometer while the angle α_2 correspond the solar elevation angle where rays from the sun disc shine on the whole pyranometer.

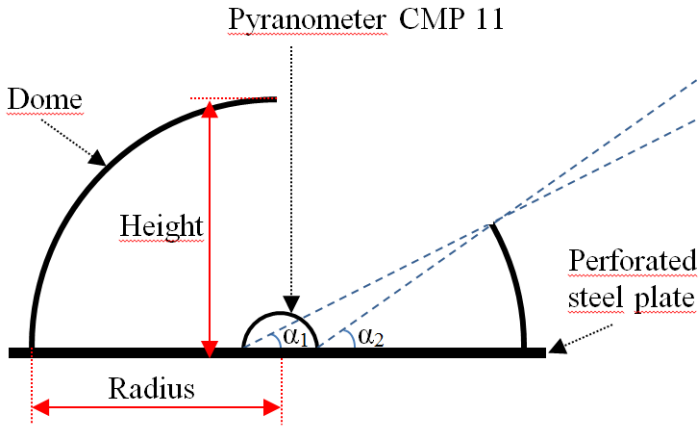

Figure 1.7: cross section view of the dome with 1/16 opening area and the pyranometer in the center.

1.3 Side-by-side measurements of 16 pyranometers

Initially side-by-side measurements are carried out in order to verify that all pyranometers give a similar response under identical weather conditions. The measurement system reports 1-minute values from all the instruments.

Figure 1.8 shows a picture of the experimental set-up for side-by-side measurements.

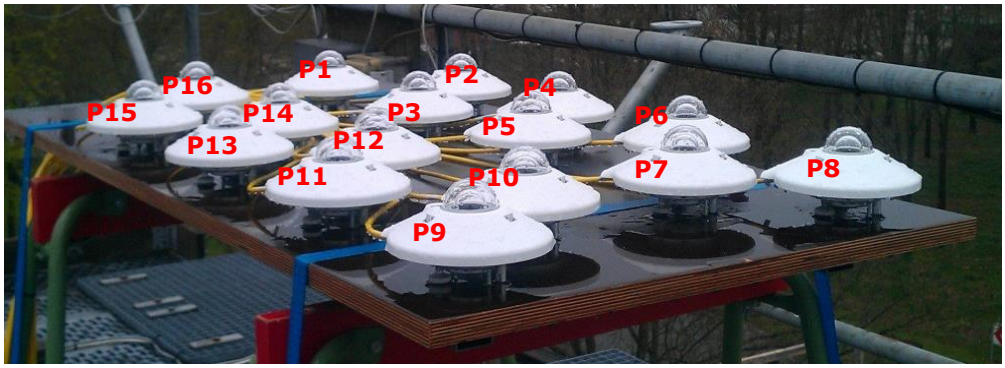

Figure 1.8: Experimental set-up for side-by-side measurements.

Figure 1.9 – Figure 1.10 show results of the side-by-side tests on June 7, 2013.

Figure 1.9 shows the GHI from all 16 pyranometers during the day. From Figure 1.9 it is clear to see how the railing on the climate station alternately causes shading on the pyranometers early in the morning and late in the afternoon. During the morning and the afternoon, the sky is clear without clouds. Therefore this period is used to compare the readings from the 16 pyranometers. During the middle of the day, the weather conditions are cloudy and therefore not suitable for comparing the readings from the 16 pyranometers. The reason is that clouds may cause shading on some pyranometers while not on others and because clouds may reflect additional solar radiation to some of the pyranometers.

Figure 1.10 shows the irradiance of each pyranometer relative to the average irradiance of 16 pyranometers. From Figure 1.10 it can be seen that the relative deviation varies with the irradiance magnitude. As expected, the relative deviation is higher for low irradiance levels than for high irradiance levels. The relative deviation lies within the accuracy of the measurements. All the pyranometers are considered suitable for the investigation of how the diffuse solar irradiance is distributed over the sky dome.

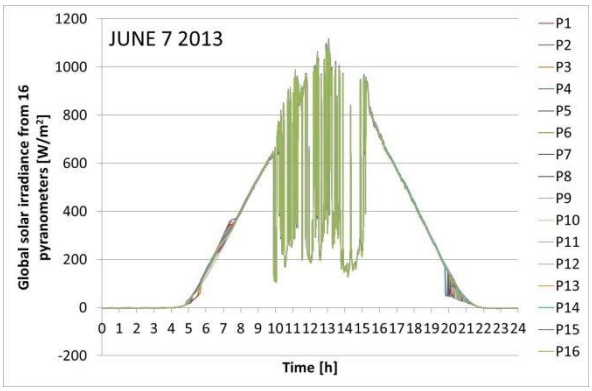

Figure 1.9: Side-by-side measurements of GHI with 16 pyranometers.

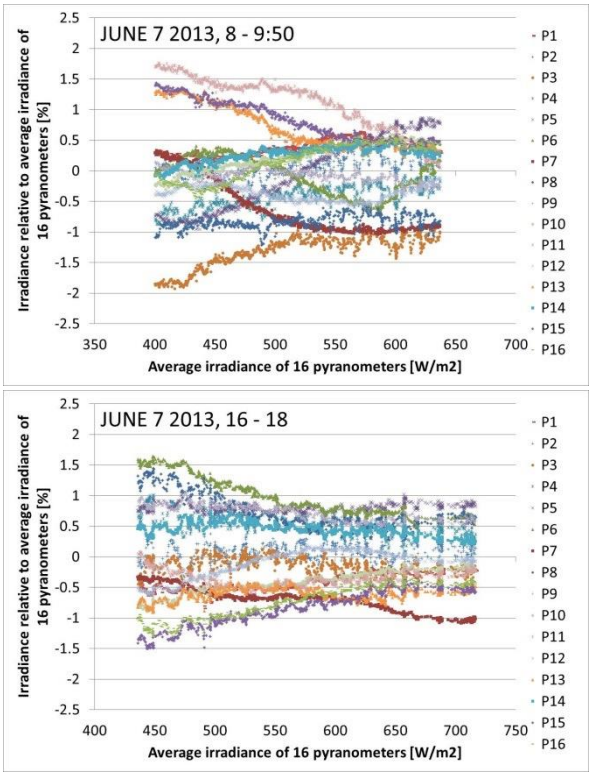

Figure 1.10: Relative irradiance deviation from average irradiance of 16 pyranometers during morning and afternoon under clear sky conditions.

1.4 References

Michalsky, J. J.. The astronomical Almanac's algorithm for approximate solar position (1950-2050), Sol. Energy, 40, 227-235. 1988.

Reda, I., A. Andreas. Solar position algorithm for solar radiation applications, Sol. Energy, 76 (5), 577-589, 2004.

Reda, I., A. Andreas. Corrigendum to "Solar position algorithm for solar radiation applications" [Solar Energy 76 (2004) 577–589], Sol. Energy, 81 (6), 838. 2007.

2. Irradiance measurements

This section describes the work carried out in WP3 'Results from pyranometers'. The aim is here to analyze the measurements of the DfHI from different parts of the sky.

The analysis is performed on 1-minute measurements from one whole year from March 2015 to February 2016.

2.1 Analysis method

The fractional horizontal measurements are exposed to horizontal screening and shading caused by the domes and reflections from the inside of the domes. This results in differences between the sum of the fractional measurements and the GHI.

The measurements used in the analysis have first been filtered through the Baseline Solar Radiation Network, BSRN filter, described by Roesch et al. (2011).

Secondly, the differences between the sum of the (1/8) fractional measurements and the GHI have been plotted against the GHI. The relationship is approximately linear. A robust linear regression has been performed on the data. In this way all the error sources are accounted for in one step. All individual fractional measurements have been corrected according to the regression result.

Finally, the horizontal direct irradiance has been subtracted from the corrected fractional measurements whenever the solar azimuth angle was within the opening angles of the domes. In this way, the fractional horizontal diffuse irradiances have been derived.

2.2 Horizontal screening

Figure 2.1 shows a 360° view from the center of the climate station, seen from the level of the pyranometers with the domes. It is clear to see that a small part of the horizon is screened of by tree tops and towards south by a neighbor building. The tree tops cause a horizontal screening of up to 3° except for one tree top towards southeast that causes a horizontal screening of up to 6°. The neighbor building towards south causes a horizontal screening of up to 3.5°. The pyranometer and the pyrheliometer mounted on the tracker have a clear view to the horizon without any shading.

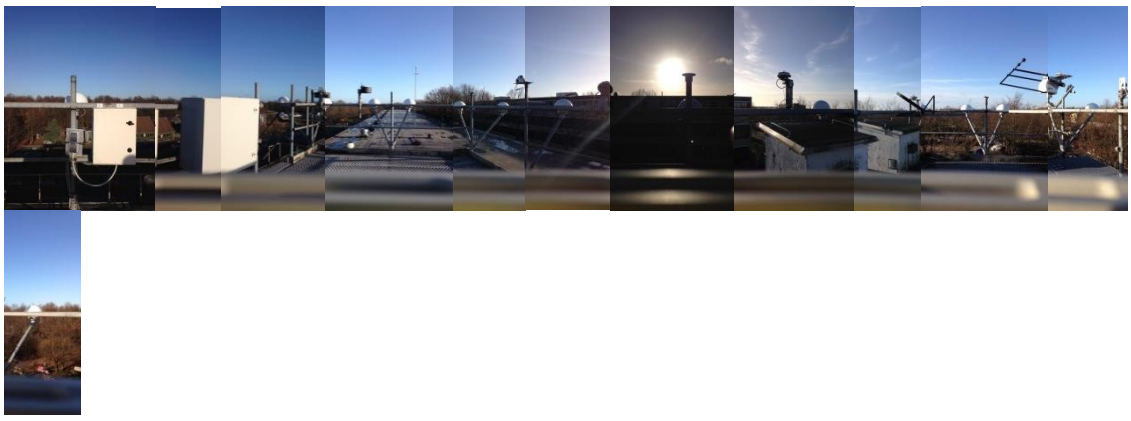

Figure 2.1: 360° view from the climate station (seen from North to North), seen from the pyranometers with the domes.

Due to the horizontal screening, all data for solar zenith angles greater than 85° are ignored.

2.3 Shading by dome

The fractional horizontal diffuse irradiance is calculated by subtracting the horizontal beam irradiance from the fractional measurement which is exposed to beam irradiance. The geometry of the domes result in shadows on the pyranometer close to the beginning and the end of the dome opening, see Figure 2.2. From the figure it is easy to see that the dome shades the pyranometer when the azimuth angle of the sun is close to the azimuth angle of the beginning and the end of the dome opening. The sun has to move 7.2° from the dome opening until the pyranometer is fully illuminated by the sun.

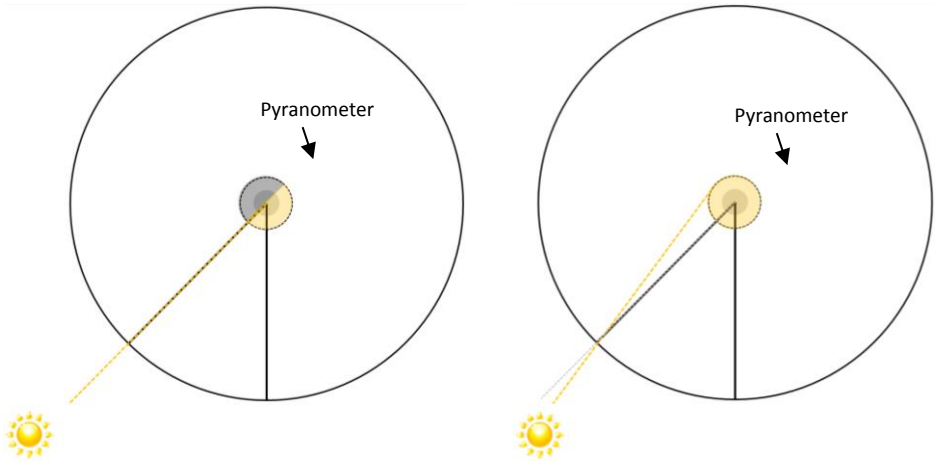

Figure 2.2: Top view of dome with 1/8 opening and pyranometer in the centre of the dome as the sun passes the opening of the dome. Left: The pyranometer is only half illuminated by the sun due to shading by the dome. Right: The pyranometer is fully illuminated by the sun.

Measurements from the areas shaded by the dome are ignored.

2.4 BSRN filter

The measurements have been filtered through the Baseline Solar Radiation Network, BSRN filter described by Roesch et al. (2011). The applied filters are described in the Table 2.1 and Table 2.2 below.

Table 2.1: The table shows the lower and upper limits for the "physically possible" intervals used in flagging the radiation quantities. S_o is the solar constant adjusted for Earth-Sun distance. μ_o is the cosine of the solar zenith angle. Parameters: GHI: Global irradiance, DfHI: Horizontal diffuse shortwave irradiance, DrHI: Horizontal direct shortwave irradiance.

Parameter	Lower bound	Upper bound
GHI	-4 W/m^2	$1.5 \cdot S_o \cdot \mu_o^{1.2}$+100 W/m^2
DfHI	-4 W/m^2	$0.95 \cdot S_o \cdot \mu_o^{1.2}$+100 W/m^2
DrHI	-4 W/m^2	$S_o \cdot \mu_o^{1.2}$

Table 2.2: Comparison criteria used for flagging the measured irradiances. Here it is checked whether the measured DfHI is realistic compared to the measured GHI. Also, the measured GHI is compared to GHI1, which is the sum of the measured DrHI and the measured DfHI (Roesch et al. 2011). SZA is the solar zenith angle.

Conditions for test
GHI/GHI1 = 1.0 ± 8% for GHI1 > 50 W/m^2, SZA < 75°
GHI/GHI1 = 1.0 ± 15% for GHI1 > 50 W/m^2, 75° < SZA < 93°
DfHI/GHI < 1.05 for GHI > 50 W/m^2, SZA < 75°
DfHI/GHI < 1.10 for GHI > 50 W/m^2, 75° < SZA < 93°

2.5 Robust linear regression

Figure 2.3 shows the horizontal fractional diffuse solar irradiance on July 1, 2015 which is a perfectly clear sky day (left) and on July 6, 2015 which is a cloudy sky day (right). In the figures, also the sums of the horizontal fractional diffuse solar irradiances as well as the DfHI are shown. The data not shown are data from the areas, shaded by the dome edges. It is clear to see that the sum of the horizontal fractional diffuse solar irradiances is larger than the DfHI on the clear sky day. On the cloudy sky day, the same difference is not significant.

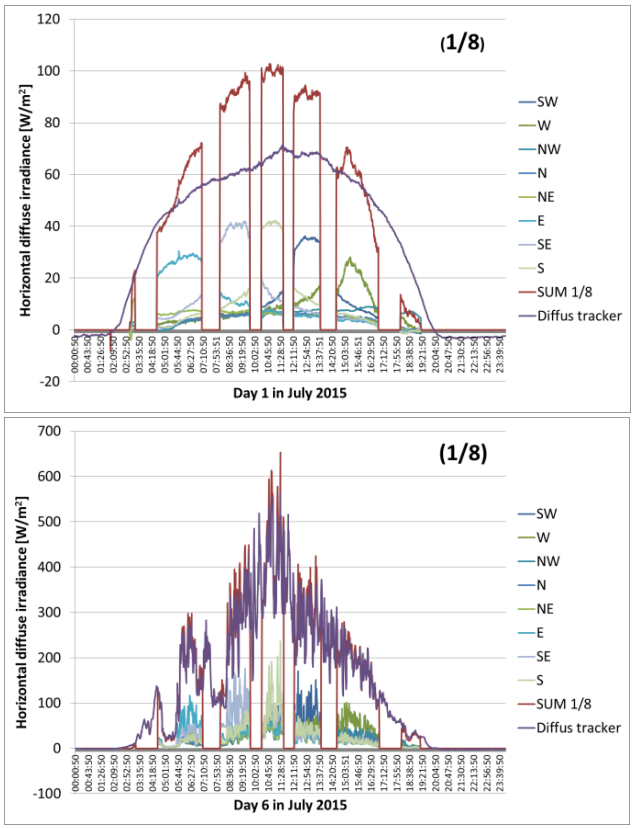

Figure 2.3: Horizontal diffuse irradiances on a clear sky day, left and on a cloudy sky day, right.

The figure 2.4 shows an analysis of the error. The error is defined as: Sum of the measured horizontal fractional solar irradiance – the measured GHI. The error is plotted against the measured GHI.

The figures show that the error exists under all weather conditions and that the relationship between the error and the GHI is approximately linear.

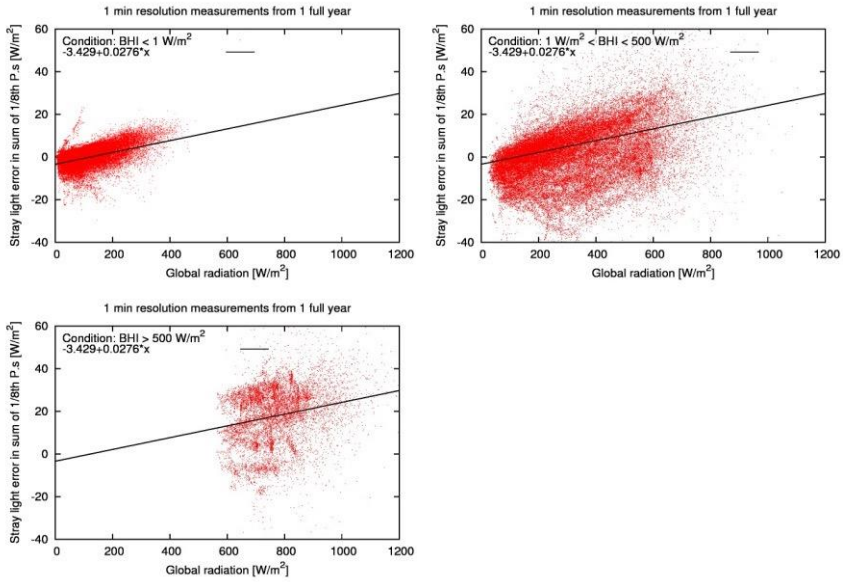

Figure 2.4: Error analysis of the horizontal fractional measurements.

A robust linear regression on the measured (1/8) data from one full year from March 2015 to February 2016 result in:

Sum(1/8).correct = sum(1/8).measured – (-3.429 + 0.0276 * GHI) (1)

Sum(1/8).correct = GHI (2)

Sum(1/8).measured = 1.0276 * GHI – 3.429 (3)

GHI = (Sum(1/8).measured + 3.429) / 1.0276 (4)

Assuming that the error is distributed according to the magnitude of the measurement of each individual (1/8) pyranometer, the corrected value of each pyranometer becomes:

(1/8).correct = ((1/8).measured + 0.429) / 1.0276 (5)

It is further assumed, that the same correction is also valid for each (1/16) pyranometer.

Figure 2.5 shows the two figures shown in Figure 2.3, but now the corrections have been applied. Now the sum of the horizontal fractional diffuse solar irradiances is similar to the DfHI. The remaining differences seen are likely to arise from the uncertainty in the levelling of the pyranometers, where a tilt of a few degrees causes errors of the order of 10 W/m^2 in the DrHI. When the DrHI is subtracted from the total fractional solar irradiances of domes pointing toward the sun, this affects the derived fractional diffuse solar irradiances. An additional uncertainty is shading and reflection of diffuse irradiance from the objects in the horizon (Figure 2.1).

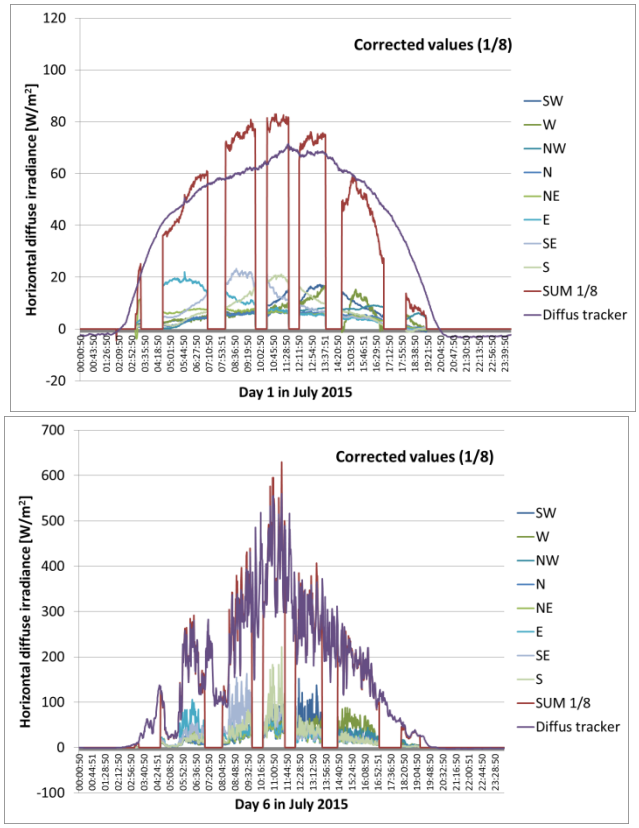

Figure 2.5: Corrected horizontal diffuse irradiance on a clear sky day, left and on a cloudy sky day, right.

2.6 Results

The results of the investigation are presented here as diffuse fraction (Id/I) against clear sky index (⟩).

The diffuse fraction, Id/I is defined as: DfHI / GHI.

The clear sky index, ⟩ is an alternative to the clearness index, K_T which is widely used in the literature. The clear sky index, ⟩ is the ratio of measured GHI to the GHI in a standard clear sky situation. The clear sky GHI can be estimated with a theoretical model and depend on the atmospheric load of ozone, aerosols, water vapor, and the solar zenith angle (SZA) (Savijärvi 1990; Gleeson et al. 2015). The advantage of using the clear sky index is that the change of air mass during the course of a day is accounted for. That is not the case for the GHI at the top of the atmosphere that is used as the denominator to the measured GHI in the clearness index.

The clearness Index, K_T is defined as the ratio of measured GHI to the corresponding GHI available on the top of the atmosphere, corrected for the varying earth-sun distance caused by earth orbit ellipticity.

In clear sky conditions the clear sky index should be 1.0 if the theoretical model and the input to this are correct; in practice, it often deviates from 1.0 because an incorrect water vapor or aerosol load is assumed. The clear sky index can also become larger than 1.0 temporarily when fractional cloud cover enhances the irradiance locally at the surface, e.g. (Almeida et al. 2014). Such overirradiance is seen in particular when the integration time of the measurements is low. In overcast situations, the clear sky index varies from being only a few percent to

being almost 1.0 depending on the optical thickness of the clouds. At extratropical latitudes it never goes to 0.0.

The individual fractional diffuse irradiances are presented for different intervals of the difference between the solar azimuth angle (SA) and the azimuth angle of the center of the dome (DA). In other words, the fractional diffuse irradiances are presented at various distances from the direction to the sun. The domes all point in different directions and the sun will shine into different domes during the day. Each dome has a first, a second, a third and a forth neighbor dome on both sides. The results present the fractional horizontal diffuse irradiance for the dome with the sun and for all the neighbor domes.

The (1/8) pyranometers all cover an individual part of the sky without any overlap. The following differences between SA and DA apply, see also figure 2.4, right:

- When -15.3°<SA-DA<15.3°, the sun shines into the dome and the result shows how much horizontal diffuse irradiance that reaches the pyranometer under the dome with the sun.
- When |29.7°|<SA-DA<|60.3°|, the result shows how much horizontal diffuse irradiance that reaches the first neighbor on both sides of the dome with the sun.
- When |74.7°|<SA-DA<|105.3°|, the result shows how much horizontal diffuse irradiance that reaches the second neighbor on both sides of the dome with the sun.
- And so forth…

The orientations of the (1/16) pyranometers have some overlap and the distance to the neighbors is individual for each dome opening. Hence the differences between SA and DA are narrower since only the intersections of the distances to the neighbors are used, see also figure 4, left.

Figure 2.6 shows the diffuse fraction for the horizontal diffuse irradiance and for the sum of the fractional horizontal diffuse irradiances for both (1/8) and (1/16) pyranometers. The figure shows that about 80 % of the diffuse irradiance comes from upper part of the sky when the clear sky index, 〉 is below 0.3. In clear sky conditions (〉≈1) less than 50 % of the diffuse irradiance comes from the upper part of the sky.

Figure 2.7 shows the diffuse fraction as function of the clear sky index, 〉 for the individual (1/8) pyranometers (left) and (1/16) pyranometers (right). The figure shows that the diffuse fraction is much higher for the pyranometers facing towards the southern part of the sky. The figure shows, as expected that in overcast sky conditions, the diffuse fraction is the same for all (1/8) pyranometers and the same for all (1/16) pyranometers.

Figure 2.8 – Figure 2.12 show the diffuse fraction as function of the clear sky index, 〉 for the individual (1/8) pyranometers (left) and (1/16) pyranometers (right) when the sun shines into the dome opening and the diffuse fraction in the first, second, third and fourth neighbor domes to the domes with the sun. It is clear to see that the diffuse fractions are strongly dependent on the distance between SA and DA and 〉. The closer the sun is to the dome opening, the higher the diffuse fraction and vice versa.

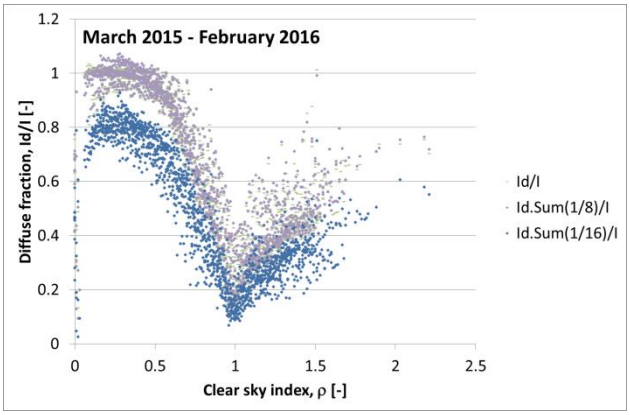

Figure 2.6: Diffuse fraction as function of clear sky index for the total measurements and for the sum of (1/8) pyranometers and (1/16) pyranometers.

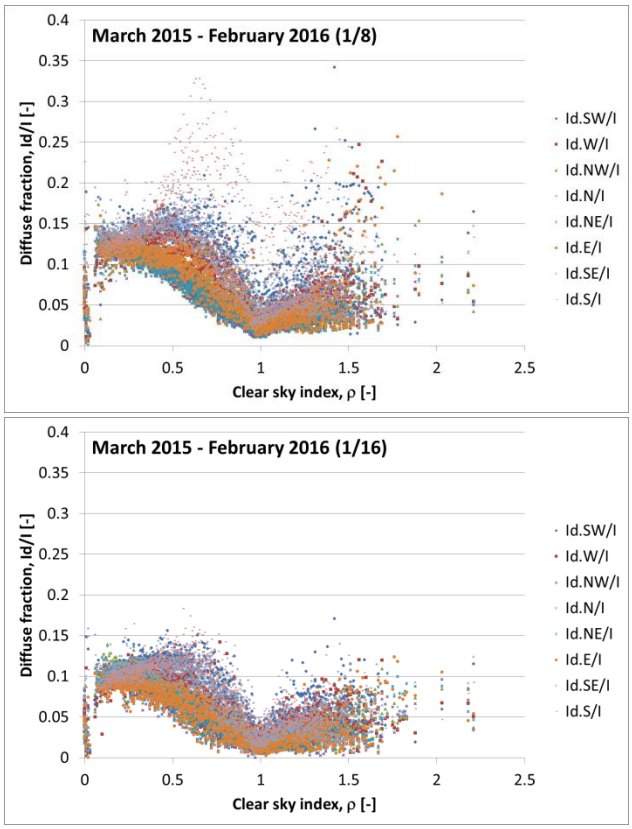

Figure 2.7: Diffuse fraction as function of clear sky index. Left: (1/8) pyranometers. Right: (1/16) pyranometers.

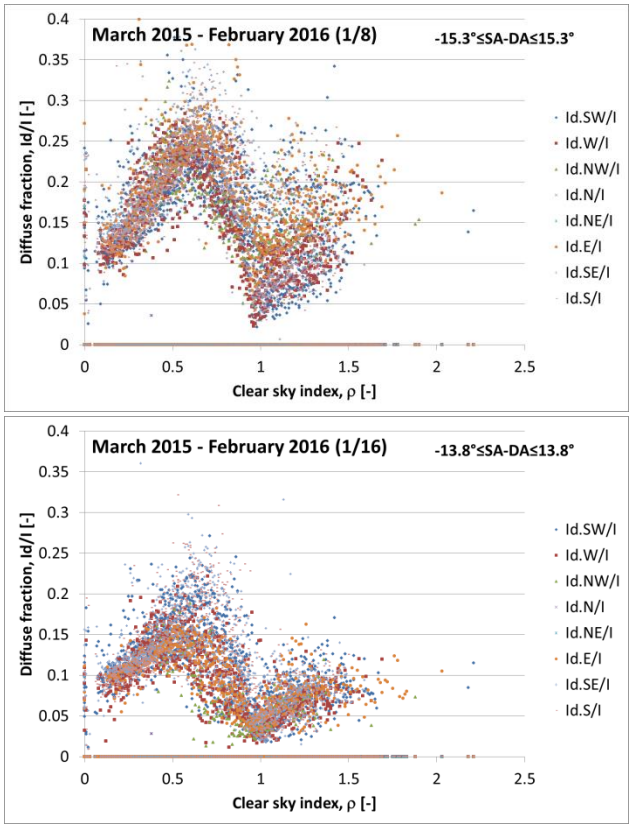

Figure 2.8: Diffuse fraction as function of clear sky index in the dome openings with the sun. Left: (1/8) pyranometers. Right: (1/16) pyranometers.

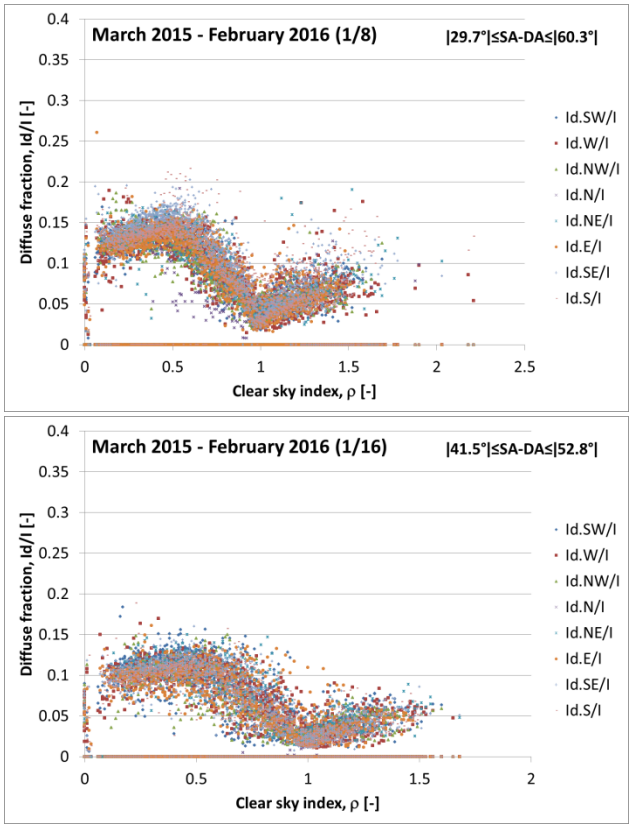

Figure 2.9: Diffuse fraction as function of clear sky index in the first neighbor dome openings to the dome opening with the sun. Left: (1/8) pyranometers. Right: (1/16) pyranometers.

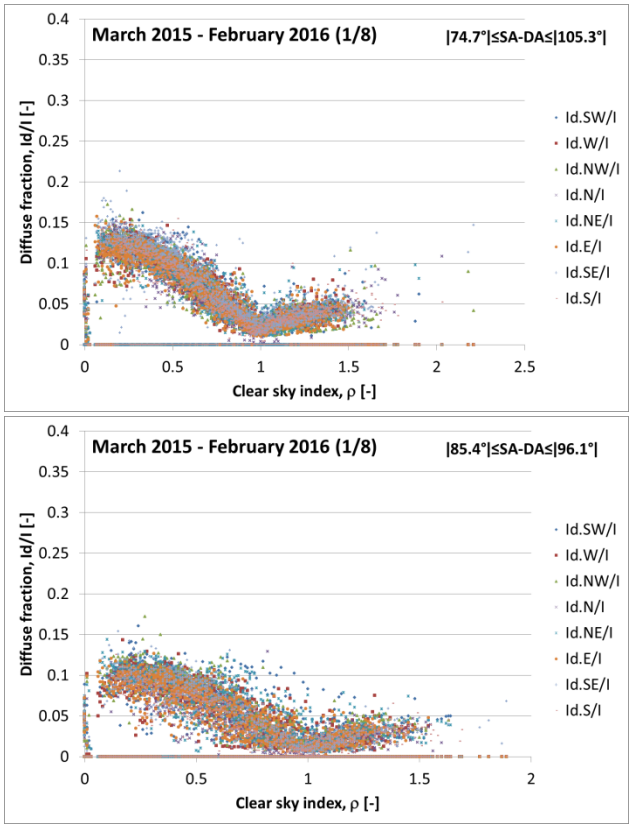

Figure 2.10: Diffuse fraction as function of clear sky index in the second neighbor dome openings to the dome opening with the sun. Left: (1/8) pyranometers. Right: (1/16) pyranometers.

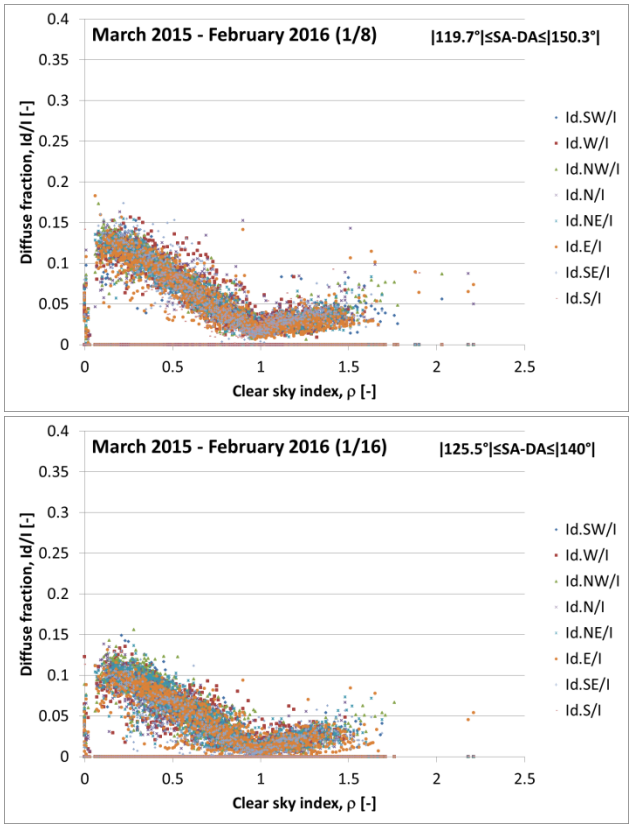

Figure 2.11: Diffuse fraction as function of clear sky index in the third neighbor dome openings to the dome opening with the sun. Left: (1/8) pyranometers. Right: (1/16) pyranometers.

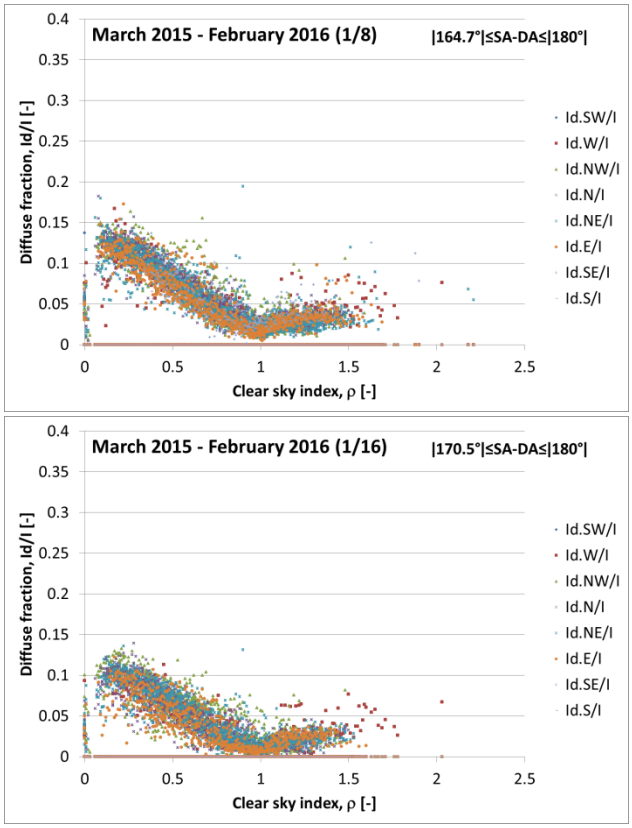

Figure 2.12: Diffuse fraction as function of clear sky index in the fourth neighbor dome openings to the dome opening with the sun: Left (1/8) pyranometers. Right: (1/16) pyranometers.

2.7 References

Almeida, M. P., R. Zilles, E. Lorenzo. Extreme overirradiance events in São Paulo, Brazil. Solar Energy, 110, 168-173, 2014.

Gleeson, E., V. Toll, K. P. Nielsen, L. Rontu, and J. Masek. Effects of aerosols on solar radiation in the ALADIN-HIRLAM NWP system. Atmospheric Chemistry and Physics Discussions, 15 (22), 32519–32560, 2015.

Roesch A. et al. Assessment of BSRN radiation records for the computation of monthly means. Atmos. Meas. Tech., 4, 339–354, 2011

Savijärvi, H. Fast Radiation Parameterization Schemes for Mesoscale and Short-Range forecast Models, J. Appl. Meteorol., 29, 437-447, 1990.

3. Theoretical study of directional and spectral solar irradiances

3.1 Introduction

The energy flux from the sun comes to us in the form of electromagnetic irradiance within the spectral range from 280 nm to 10 µm. The total energy flux integrated over the whole spectrum is referred to as the global irradiance. Global irradiance is given in units of W/m^2. It can be considered either with respect to a horizontal surface element of a tilted surface element. The latter is useful for the case for solar heating collectors or photovoltaic panels that are tilted toward the sun at fixed angles or on tracking systems. To specify when solar flux on a horizontal surface is considered the term ***Global Horizontal Irradiance (GHI)*** is used.

To a first approximation, GHI can be split into two components: ***Direct normal irradiance (DNI) and diffuse irradiance***. To a second approximation, the ***radiance*** can be considered for a 1-dimensional atmosphere. Radiance is the derivative of irradiance with respect to solid angle and a horizontal surface element. It is given in units of $W/(m^2\ sr)$. For a 1-dimensional atmosphere the angular radiance distribution can be calculated accurately with the DISORT model (Stamnes et al. 1988; Dahlback & Stamnes 1991; Lin et al. 2015). Radiances can also be calculated for 3-dimensional cases (e.g. Evans 1998; Mayer 1999), however, to do this detailed knowledge of the 3-dimensional cloud water distribution is needed. Here, we will consider only 1-dimensional cases. We use DISORT simulations to show the primary factors affecting the variability of the solar resource. Finally, we compare the theoretical 1-dimensional results to the 1-minute measurements presented in Chapter 2 and discuss the results.

3.2 Solar variability

The daily variation in the solar resource that we experience is caused by the rotation of the Earth, while the yearly variability is caused by the tilt of the rotation axis relative to the position of the Sun. Although this sounds simple calculating the accurate position of the Sun for a given time and place requires a lot more computations than simple harmonic functions for the daily and yearly variations. Blanco-Muriel et al. (2001), Grena (2008) and Reda & Andreas (2004, 2007) have written algorithms for calculating the solar vector for a given time and place. Which of these algorithms to use depends on the level of accuracy required. Be aware that the simpler algorithms are parametrizations that are only valid for a certain time period and will be less accurate after this period.

The elliptical orbit of the Earth around the Sun causes variations in the top of the atmosphere solar irradiance of 6.68% from the perihelion in early January to the aphelion in early July (Michalsky 1988). The average solar irradiance at 1 astronomical unit is estimated to be $1361\pm0.5\ W/m^2$ (Kopp & Lean 2011). Satellite measurements have shown the Sun to be remarkably stable over time. Quasi-periodical (approximately 11 year) variations occur, but the relative difference from maximum to minimum is only about 0.1%. Therefore, it is reasonable to assume that changes in the solar irradiance output do not directly affect the variability in the GHI and DNI.

3.3 Clouds

The primary factor controlling the short term variability in the GHI and DNI solar resource is clouds. Radiation sensitivity tests have been made with the HARMONIE NWP model (Nielsen et al., 2014).

In Fig. 3.1 the effect of clouds on the spectrally resolved GHI resource is shown. The solar irradiance is here divided into its direct beam (red curves) and diffuse (green curves) components. For clear sky conditions (Fig 3.1 upper left) most of the GHI comes from the direct solar beam. The diffuse component in clear sky conditions is due to Rayleigh scattering, which increases strongly with decreasing wavelength. Rayleigh scattering is what makes the sky blue. Below a thin cloud (Fig 3.1 upper right) the total GHI resource is not much smaller than in clear sky conditions, but it can be seen that the diffuse component is now much more prevalent than the direct component. For the thicker clouds (Fig. 3.1 lower panels) the direct component is no longer significant. Additionally it can be seen that the spectral shape changes as the clouds get increasingly thicker. Due to water absorption at the infrared wavelengths these are extinct before the visible and ultraviolet wavelengths in the solar spectrum. Accounting for this is important when estimation the solar lighting (illuminance) from the overall solar energy (irradiance) and when considering the solar resource for photovoltaic units that can only utilize a limited spectral range of irradiances.

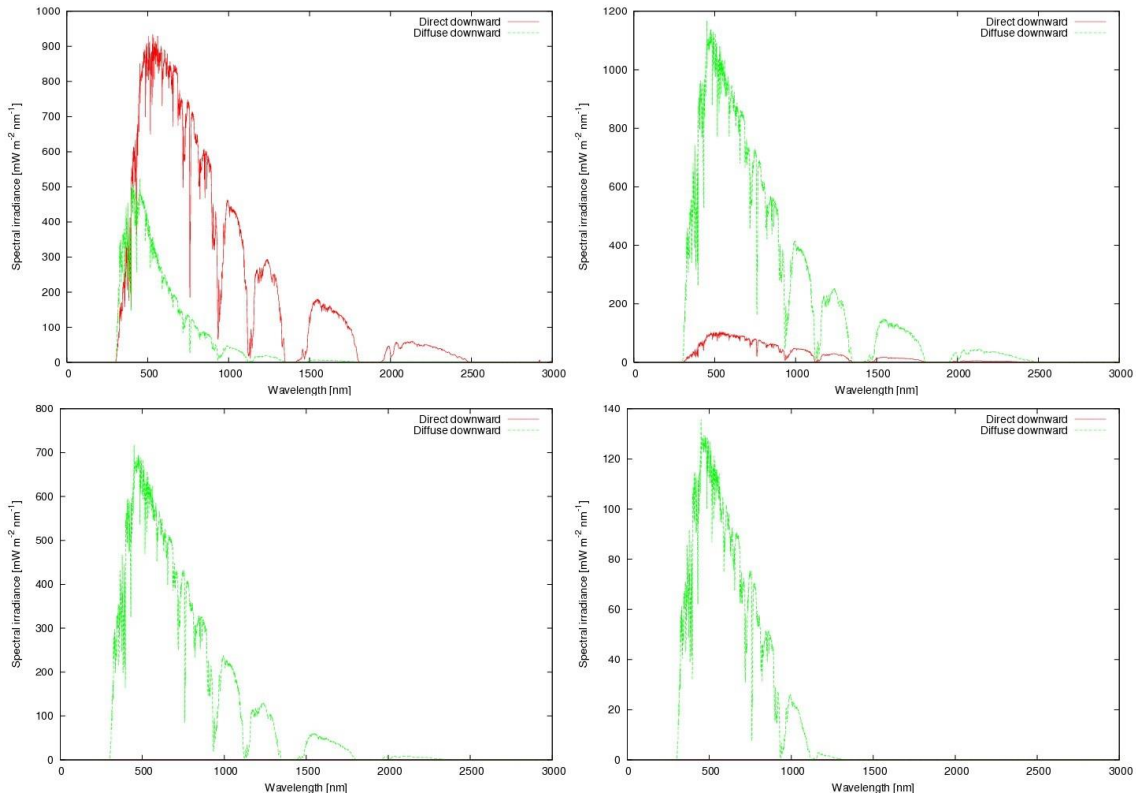

Fig. 3.1. **Upper left:** The solar spectrum at the surface in clear sky conditions. **Upper right:** The solar spectrum below a thin cloud with 10 g/m2 water droplets of average size 10 µm. **Lower left:** The solar spectrum below a cloud with 100 g/m2 water droplets of average size 10 µm. **Lower right:** The solar spectrum below a thick cloud with 1000 g/m2 water droplets of average size 10 µm.

The results in Fig 3.1 are for a given solar zenith angle, surface albedo and cloud microphysical properties. More extensive analyses of these effects on the overall GHI resource can be found in the paper by Nielsen et al. (2014). More detailed spectral analyses can be obtained by contacting Kristian P. Nielsen (kpn@dmi.dk).

Fig. 3.2 shows the theoretical scattered radiance distributions calculated with the DISORT routine in the libRadtran library (Mayer & Kylling 2005). The panels show that, even in the case of homogeneous stratiform clouds, the distribution of scattered radiance is not simple and far from uniform as is often assumed. Since DISORT calculates values for a 1-dimensional atmosphere only, these simulations are not valid for fractional cloud cover.

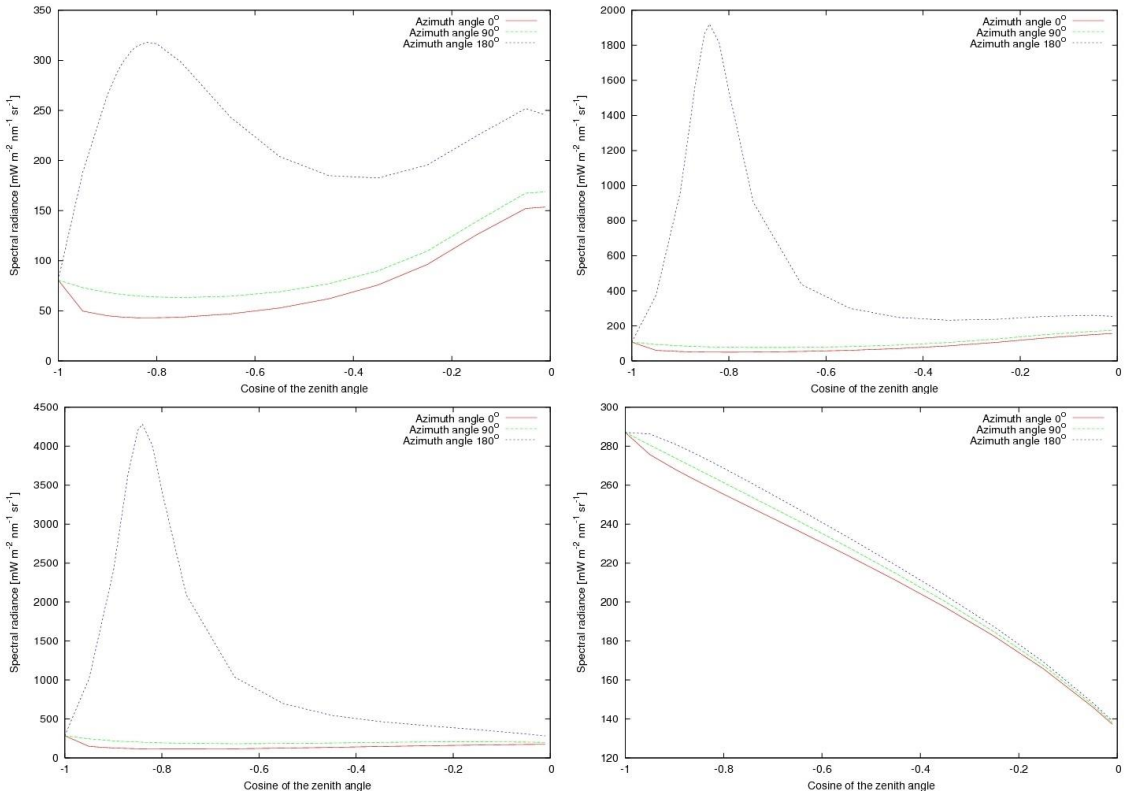

Fig. 3.2. The upper left panel shows the downward scattered radiance distribution at the surface for clear sky conditions and rural aerosols (Shettle 1989). The upper right panel shows the same beneath a liquid cloud with 1 g/m² cloud water load and an effective cloud droplet radius of 10 µm. The lower left panel shows the same for a liquid cloud with 10 g/m² cloud water load. The lower right panel shows the same for a liquid cloud with 100 g/m² cloud water load. All the calculations shown here are valid for a wavelength of 550 nm.

From Fig. 3.2 several important features of the scattered/diffuse irradiance can be seen:

1. In the clear sky case the radiance increases with a factor of three from the cosine solar zenith angle of -0.8 (corresponding to a solar zenith angle of 37°) to the horizon or cosine solar zenith angle of 0.0. This is the effect of horizontal brightening.

2. In the thin cloud and medium thick cloud cases most of the diffuse irradiance is scattered at small angles around the solar beam. This is the circumsolar irradiance. For solar heating collectors, photovoltaic units and building surfaces this should be considered as coming from direction of the sun.

3. Beneath thick clouds the radiance is approximately twice as large from straight above as compared with from the horizon.

All these three effects show the error in considering the diffuse irradiance to be evenly distributed over the sky-hemisphere.

3.4 Clear skies

The clear sky solar spectrum can be seen in the upper left panel of Fig. 3.1. This depends on gasses and aerosols in the atmosphere. The most abundant gasses Nitrogen and Oxygen determine how much solar irradiance is scattered by Rayleigh scattering in a dry atmosphere. They vary with the surface atmospheric pressure, which changes with altitude and weather

patterns. The variation of air pressures at sea levels is 10% from the lowest (around 950 hPa) to the highest (around 1050 hPa) air pressures.

Water vapour has several absorption lines in the infrared part of the solar spectrum. In a wet mid-latitude summer atmosphere (Anderson et al. 1986) water vapour absorbs up to 15% of the GHI resource (Nielsen et al. 2014). Nielsen et al. (2014) also tested the effect of reducing the ozone layer thickness from 500 Dobson Units (DU) to 100 DU. This caused the GHI to increase by 2.3%. Since 500 DU and 100 DU are extreme values of the ozone layer thickness, this can to a good approximation be assumed to be constant in GHI clear sky simulations. The variability of other gasses is of less importance for solar energy applications.

Aerosols affect the clear sky resource - in particularly in areas affected by dust storms or forest fires. The best aerosol data set currently available is the MACC reanalysis data set (Inness et al. 2013). Aerosol sensitivity tests with the HARMONIE weather prediction model used at DMI have been done by Toll & Männik (2015), Gleeson et al. (2015) and Toll et al. (2016).

3.5 Testing radiative transfer assumptions in weather prediction models

Weather prediction models and climate models need to perform a large number of radiation calculations. In a DMI two-day forecast approximately one billion solar and thermal radiation computations are made. DMI currently runs such forecasts 12 times each day. Here the DISORT model is too time-consuming. Instead the two-stream approximation is used. In this only direct solar beam irradiance, downward diffuse irradiance and upward diffuse irradiance is considered. The approximation works by considering the circumsolar irradiance to be part of the direct solar beam and the diffuse irradiance to have a constant directional distribution (Joseph et al. 1976; Ritter & Geleyn(1992); Thomas & Stamnes (2002)).

Different types of two-stream approximations exist. The most prevalent of these in atmospheric models is the Delta-Eddington approximation (Joseph et al. 1976). We have tested this against the DISORT simulations of GHI (Nielsen et al. 2014; Gleeson et al. 2015). The results are shown in Fig. 3.3.

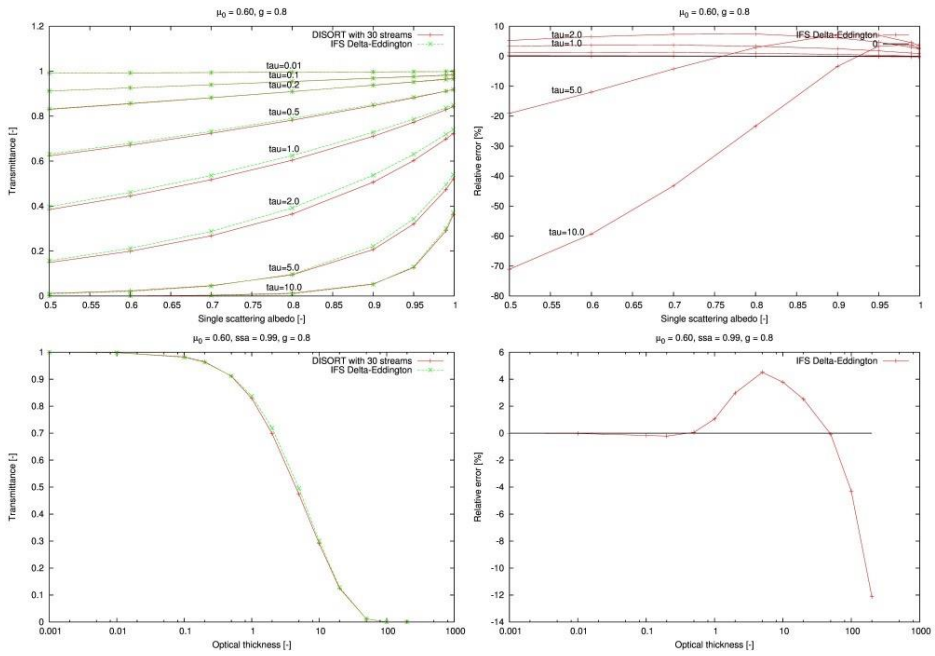

Fig. 3.3: GHI transmittance estimated with the Delta-Eddington radiative transfer scheme as compared with accurate DISORT simulations. In all cases a cosine solar zenith angle (μ_0) of 0.6 and a scattering asymmetry factor (g) of 0.8 is considered. **Upper left:** The transmittance as a

function of optical thickness (τ) and single scattering albedo. **Upper right:** As the previous panel but for the relative error of the Delta-Eddington approximation compared with DISORT. **Lower left:** The transmittance as a function of optical thickness for a single scattering albedo (ssa) of 0.99. **Lower right:** As the previous panel but for the relative error of the Delta-Eddington approximation compared with DISORT.

The relative errors in GHI transmittance of the Delta-Eddington approximation is within ±10% in these experiments for most cases. The relative error only becomes larger than this as a the transmittance tends toward zero, in which case the relative error is of little importance.

Other types of two-stream radiative transfer schemes also exist. In Fig. 3.4 tests of some of these are shown. Again the DISORT scheme is used as a reference. Details about these results can be found in the publication of Gleeson et al. (2015). Here it should only be noted that the Ritter & Geleyn (1992) two-stream radiative transfer scheme performs better than the Delta-Eddington scheme for optical thicknesses from 0.0 to 2.0. Again the largest relative errors seen in Fig. 3.4 are related to low absolute transmittances.

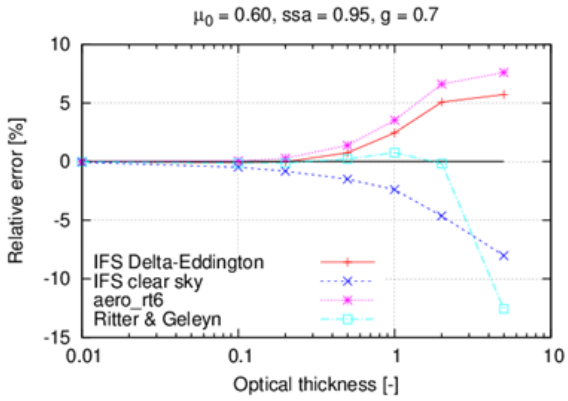

Fig. 3.4: Relative error of the tested NWP schemes relative to DISORT with respect the optical thickness (τ) for a cosine solar zenith angle (μ0) of 0.6, a single scattering albedo (ssa) of 0.95, and a scattering asymmetry factor (g) of 0.7.

3.6 Comparison of 1-D radiative transfer with measurements

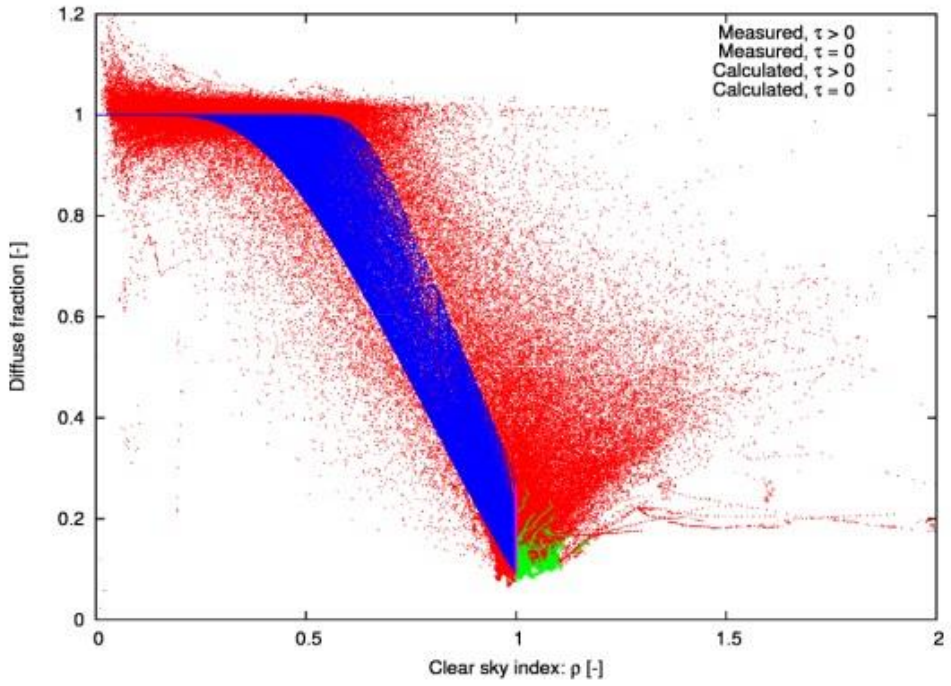

Fig. 3.5: The diffuse fraction (DfHI/GHI) plotted as a function of the clear sky index. The red and green points are measured values, while the blue and magenta points are calculated values.

Fig. 3.5 (above) shows 1-minute data measured at the DTU climate station plotted as a function of the clear sky index (the measured GHI relative to the theoretical clear sky GHI) and the diffuse fraction (the DfHI relative to the GHI). On top of the measured data calculated synthetic data are plotted. The synthetic data are fitted to the measurements by using the known solar zenith angle and varying the cloud optical thickness calculated with a 1-D radiative transfer model. ***The measurements can be divided into three groups***. In ***the first group*** a band around a diffuse fraction value of 1.0 and low clear sky indices can be seen. In ***the second group*** a broader band with descending diffuse fraction values from intermediated clear sky indices toward the clear sky index of 1.0 can be seen. A minimum of the diffuse fraction values of around 0.1 is seen at the clear sky index of 1.0. In ***the third group*** a triangle of points with higher clear sky indices than 1.0 is found. In this group the diffuse fractions are larger than at the minimum point and increase with increasing clear sky index.

Interpreting these results, we see that in ***the first group*** the calculated values have diffuse fractions of 1.0 exactly for the lowest clear sky indices. This corresponds to the overcast situation with optically thick clouds, through which no DrHI penetrates. The scatter of the measured results around the calculated values arises from the uncertainty in the measured diffuse fraction, which is the root square sum of the measurements of DrHI and DfHI. In ***the second group*** the calculated values cover a broad declining band. The decline as a function of the clear sky index arises from optically thinner clouds through which progressively more DrHI is transmitted. The width of the band corresponds to different solar zenith angles (SZAs) with the lowest SZA at the bottom of the band, for instance the minimum point in the plot corresponds to the sun at noon in midsummer on a clear sky day. In other clear sky instances (where the SZA is higher) there will be more Rayleigh scattering, and therefore relatively higher diffuse fractions. ***The third group*** of the data is not represented by the calculated values. Clearly the measured values in this group are outside the range that could be due to measurement uncertainties. The reason for this – broken cloud cover – has already been discussed in section 2.6.

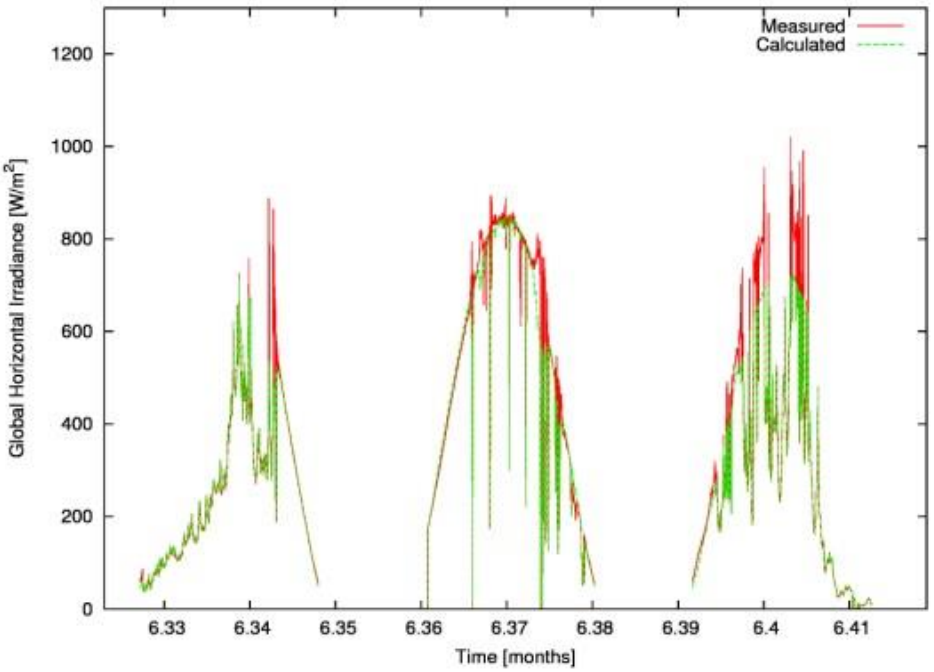

Fig. 3.6: Measured (red lines) and calculated (green lines) GHI plotted as a function of time in months. Specifically, data from the 11th, 12th and 13th of June 2015 are shown here.

In Figs. 3.6-3.8 concrete examples of days with more irradiance than can be explained with the 1-D radiative transfer model are shown. The figures show 1-minute resolution GHI, DfHI and estimated cloud optical thicknesses, respectively.

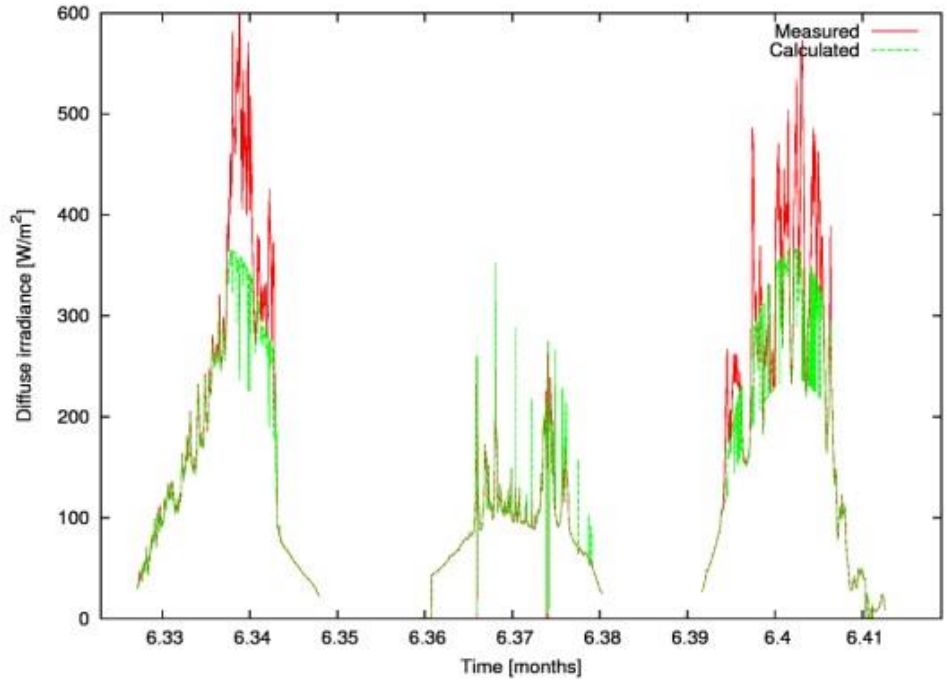

Fig. 3.7: Measured (red lines) and calculated (green lines) DfHI plotted as a function of time in months. As in Fig. 3.6 data from the 11th, 12th and 13th of June 2015 are shown.

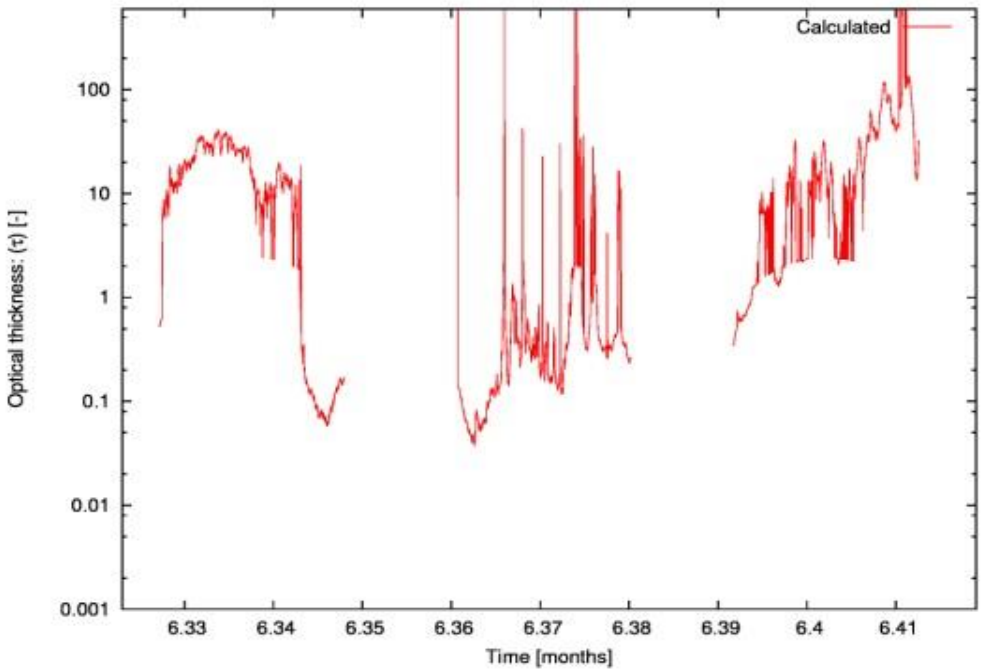

Fig. 3.8: Calculated optical thicknesses plotted as a function of time in months. As in Figs. 3.6 and 3.7 data from the 11th, 12th and 13th of June 2015 are shown.

On the 11th of June optical thicknesses of 10 to 40 are seen in the first part of the day. For these, the calculated irradiances fit the measured ones well. Then the clouds get thinner and more variable, and the DfHI achieves values in the range 400 to 600 W/m^2 that the calculated values cannot cover. Inhomogeneous cloud cover with varying thickness across the sky, is the likely explanation. In the end of the afternoon optical thicknesses of 0.05 to 0.15 are estimated. This corresponds to the background aerosol optical thickness that is present in clear sky conditions. In this case the calculated irradiances again fit the measured irradiances well.

On the 12th of June a day only a few scattered clouds occurred. This is a typical Danish summer day, where cumulus humilis are formed on a clear sky day in increasing numbers and sizes until the late afternoon when the clouds again subside and dissolve. When the cumulus clouds are

close to the solar direction both the DfHI and the GHI increase above the clear sky values. This GHI increase is not capture by the 1-D radiative transfer model. When the cumulus clouds pass in front the sun sharp drops in GHI are seen. In these situations the 1-D radiative transfer model calculated GHIs are underestimated while the DrHIs are overestimated.

On the 13th of June a more complex cloud situation with broken clouds occurs in the middle of the day. This can be seen from the high frequency variability of both GHI and DfHI. Here the 1-D calculated irradiances fit the measured irradiances poorly and often underestimate both GHI and DfHI.

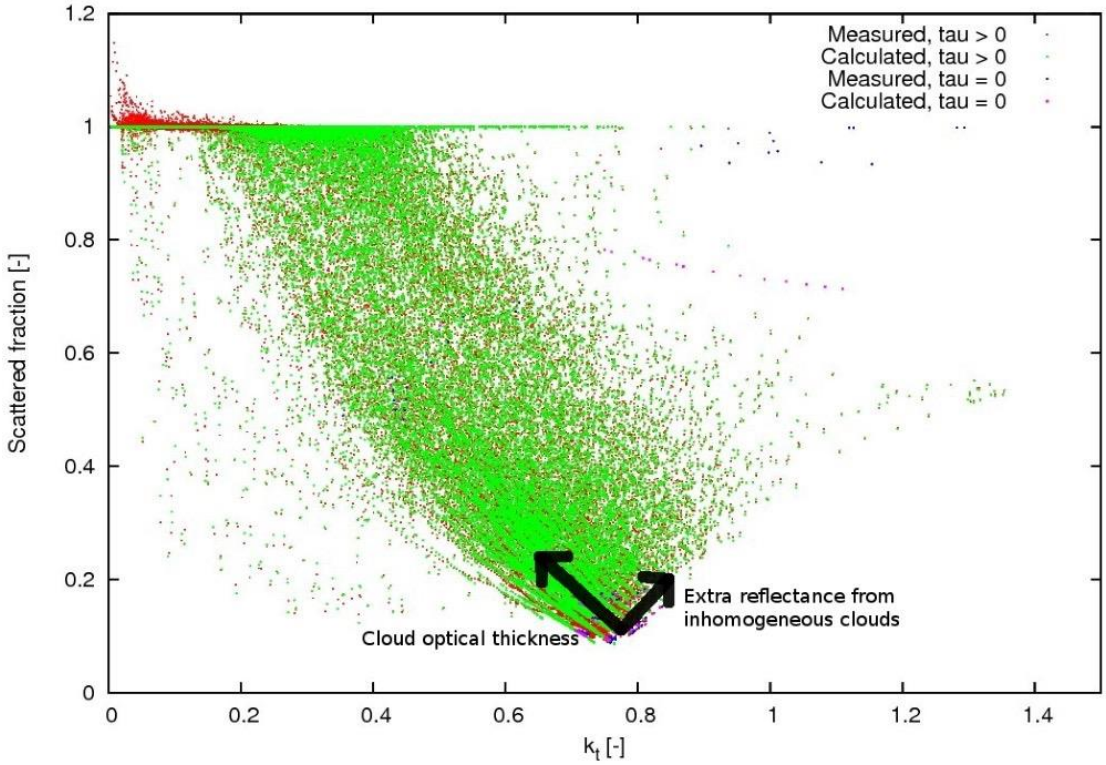

Fig. 3.9 (above) shows 2-minute data measured at the DTU climate station plotted as a function of the clear sky index (the measured GHI relative to the theoretical clear sky GHI) and the diffuse fraction. On top of the measured data calculated synthetic data are plotted. An extra term is included in these calculations to account for 3-D cloud effects. The synthetic data are fitted to the measurements from a basis made up by the cloud optical thickness calculated with a 1-D radiative transfer model and additional (or less) diffuse irradiance coming from inhomogeneous (3-D) clouds. The suggestion of using this basis is a novelty. The cloud optical thickness in the direction of the Sun can be estimated even in cases of inhomogeneous cloud covers. From theoretical calculations, the extent and magnitude of circumsolar irradiance vary as a function of this cloud optical thickness. This makes the basis useful for describing the directional distribution of solar irradiances. Additionally, it can be used to describe the full gamut of measurements in the figure unlike models that estimate the diffuse fraction only as a function of the clearness index and the solar zenith angle.

3.7 References

Anderson, G. P., Clough, S. A., Kneizys, F. X., Chetwynd, J. H. and Shettle, E. P. AFGL Atmospheric Constituent Profiles (0–120 km), Tech. Rep. AFGL-TR-86-0110, Air Force Geophysics Lab Hanscom AFB, MA, USA, 1986.

Blanco-Muriel, M., D. C. Alarcón-Padilla, T. López-Moratalla and M. Lara-Coira. Computing the solar vector, Sol. Energy, 70 (5), 431-441, 2001.

Brassuer, G. and S. Solomon. Aeronomy of the Middle Atmosphere. D Reidel Publishing Company, 3300 AA Dordrecth, Holland, 1986.

Dahlback, A. and K. Stamnes. A new spherical model for computing the radiation field available for photolysis and heating at twilight. Planet. Space Sci., 39, 671–683, 1991.

Evans, K. F. The spherical harmonics discrete ordinate method for three-dimensional atmospheric radiative transfer. J. Atmos. Sci., 55, 429–446, 1998.

Gleeson, E., V. Toll, K. P. Nielsen, L. Rontu, and J. Masek. Effects of aerosols on solar radiation in the ALADIN-HIRLAM NWP system. Atmos. Chem. Phys. Discuss., 15 (22), 32519–32560, 2015.

Grena, R. An algorithm for the computation of the solar position. Sol. Energy, 82 (5), 462-470, 2008.

Inness, A., Baier, F., Benedetti, A., Bouarar, I., Chabrillat, S., Clark, H., ... and Zerefos, C. The MACC reanalysis: an 8 yr data set of atmospheric composition. Atmos. chem. phys., 13, 4073-4109, 2013.

Joseph, J.H., Wiscombe, W.J. and Weinman, J.A. The Delta-Eddington approximation for radiative flux transfer, J. Atmos. Sci., 33, 2452–2459, 1976.

Kopp, G. and J. L. Lean. A new, lower value of total solar irradiance: Evidence and climate significance, Geophys. Res. Lett., 38 (1), L01706, 2011.

Lin, Z., S. Stamnes, Z. Jin, I. Laszlo, S.-C. Tsay, W. J. Wiscombe and K. Stamnes. Improved discrete ordinate solutions in the presence of an anisotropically reflecting lower boundary: Upgrades of the DISORT computational tool. J. Quant. Spec. Rad. Trans., 157, 119–134, 2015.

Mayer, B. I3RC phase 1 results from the MYSTIC Monte Carlo model, in I3RC workshop, Tucson, Arizona, 1999.

Mayer, B. and A. Kylling (2005): Technical note: The libRadtran software package for radiative transfer calculations – description and examples of use, Atmos. Chem. Phys. Discuss., 5, 1319–1381.

Michalsky, J. J. The astronomical Almanac's algorithm for approximate solar position (1950-2050), Sol. Energy, 40, 227-235, 1988.

Nielsen, K. P., E. Gleeson and L. Rontu. Radiation sensitivity tests of the HARMONIE 37h1 NWP model, Geosci. Model Dev., 7, 1433-1449, 2014.

Reda, I. and A. Andreas. Solar position algorithm for solar radiation applications, Sol. Energy, 76 (5), 577-589, 2004.

Reda, I. and A. Andreas. Corrigendum to "Solar position algorithm for solar radiation applications" [Solar Energy 76 (2004) 577–589], Sol. Energy, 81 (6), 838, 2007.

Ritter B. and J. F. Geleyn. A comprehensive radiation scheme for numerical weather prediction models with potential applications in climate simulations. Mon.Weather Rev., 120, 303–325, 1992.

Shettle, E. P. Models of aerosols, clouds and precipitation for atmospheric propagation studies, in: Atmospheric propagation in the UV, visible, IR and mm-region and related system aspects, 454, AGARD Conference Proceedings, 1989.

Stamnes, K., S. Tsay, W. Wiscombe & K. Jayaweera (1988): A numerically stable algorithm for discrete-ordinate- method radiative transfer in multiple scattering and emitting layered media. Appl. Opt., 27, 2502–2509.

Thomas, G. E. and Stamnes, K. Radiative Transfer in the Atmosphere and Ocean, Cambridge University Press, New York, NY, USA, 1999.

Toll, V. and Männik, A. The direct radiative effect of wildfire smoke on a severe thunderstorm event in the Baltic Sea region, Atmospheric Research, 155, 87-101, 2015.

Toll, V., Gleeson, E., Nielsen, K.P., Männik, A., Mašek, J., Rontu, L. and Post, P. Impacts of the direct radiative effect of aerosols in numerical weather prediction over Europe using the ALADIN-HIRLAM NWP system, Atmospheric Research, 172–173, 163-173, 2016.

4. Long-term meteorological data sets including 'untypical' monthly data

4.1 Introduction

This section describes the work carried out in WP6 'Analysis of measurements for untypical meteorological years for Denmark and Greenland'. When using the reference years untypical monthly weather data are removed and their effects on the performance of solar energy systems are therefore not seen. The aim is here to compare calculated performance of solar collectors based on real weather data and reference year weather data and see the effect of the untypical weather data seen in the real weather data.

The work carried out for the untypical meteorological years for Denmark is based on a previous work from 2012 were new design reference years for solar utilization were developed for 6 different locations in Denmark based on measured weather data from the period 2001 to 2010 (Furbo & Dragsted 2012). The weather data from this time period were used to calculate the performance of solar collectors and the results were then compared with the performance based on the local reference year from each location.

For the untypical meteorological years for Greenland the period 1991-2003 were used together with the reference years based on the same weather data for the locations Nuuk, Sisimiut and Uummannaq.

Nomenclature

a_1	first order heat loss coefficient, (W m^{-2} K^{-1})
a_2	second order heat loss coefficient, (W m^{-2} K^{-2})
G	global radiation, (W/m²)
I_b	beam radiation on horizontal, (W/m²)
I_d	diffuse radiation on horizontal, (W/m²)
$K_{\theta(60^\circ)}$	incidence angle modifier for diffuse radiation, (-)
p	incidence angle coefficient in the equation $K_{diff}=1-\tan(\theta/2)^p$
T_a	ambient temperature, (°C)
T_m	solar collector fluid mean temperature, (°C)
η_0	zero-loss efficiency, (-)
η	efficiency of solar collector (-)
θ	incidence angle, (°)

4.2 Weather data

4.2.1 Denmark

The weather data used in this investigation for Denmark is measured global radiation and ambient temperature from 6 different weather stations in Denmark as shown in Figure 4.1. These measured weather data sets were used to create new local reference years for solar energy utilization in order to improve the accuracy of predicted thermal performances and in order to optimize new solar collector fields (Furbo & Dragsted 2012). The measured weather data are from the period 2001-2010, although 2001 is not used in this investigation since it is an incomplete data set.

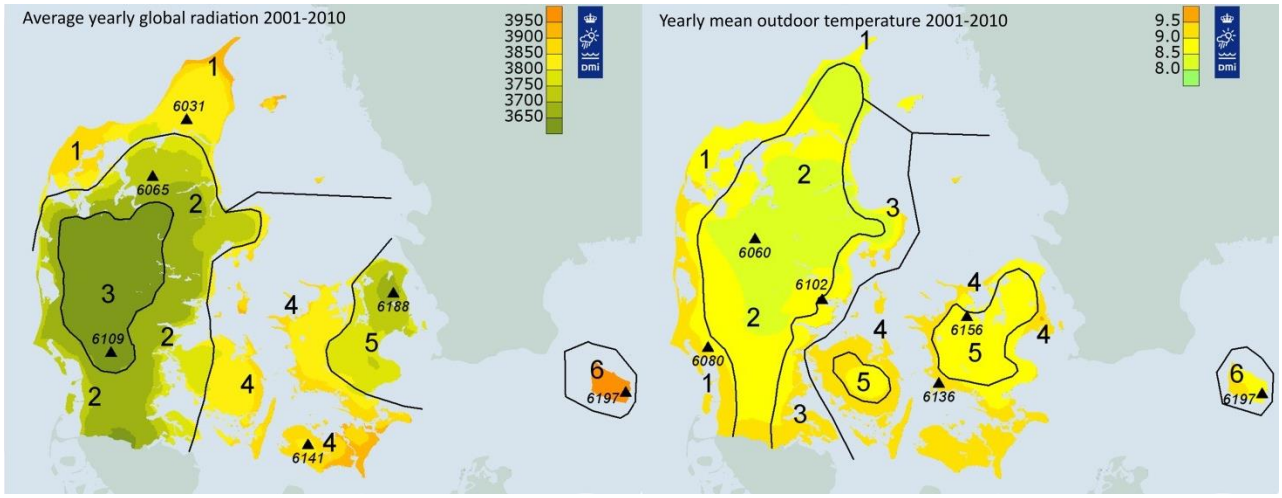

Figure 4.1 (a) Weather stations chosen for global radiation data. (b) Weather stations chosen for the ambient 2-meter temperature data. The four digit numbers are the official WMO station numbers.

The measured yearly global radiations is seen in Figure 4.2- were also the yearly global radiation for the new local reference years are shown along with the global radiation for the old Danish reference year based on data from 1975-1990 (Jensen & Lund 1995). There is a good agreement between the average measured data from 2002-2010 from each of the stations and the new local reference years. It is also seen that the new local reference years have more solar radiation compared to the old Danish reference year. It should be mentioned that there are no data available from Bornholm 2002.

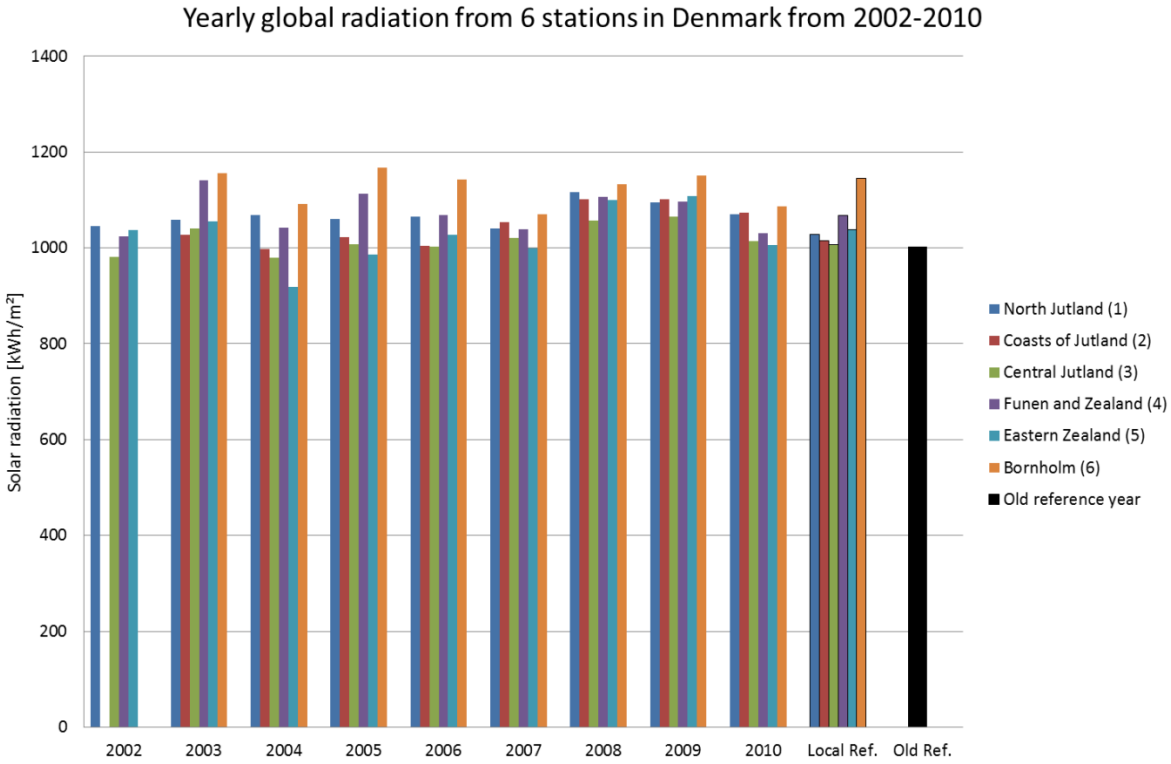

Figure 4.2 Yearly global radiation from the 6 weather stations in Denmark from the time period 2002-2010.

The figure shows that for some of the stations there is a large variation in the solar radiation from year to year. The station measuring for 'Eastern Zealand' has a max. yearly global radiation of 1108 kWh/m² per year and a min. of 918 kWh/m² per year measured in the time period, where the yearly global radiation in the new local reference year for 'Eastern Zealand' is 1038 kWh/m² per year. This is a variation of -12 % to +7 % compared to the new local refer-

ence years. Stations such as 'Bornholm' and 'Central Jutland' have much lower variations of -7 % to +2 % for 'Bornholm and' -3 % to +6 % for 'Central Jutland'.

The beam and diffuse radiation is calculated using the model 'Skartveit and Olseth' (1998) for determining the diffuse horizontal irradiance and the beam normal irradiance.

4.2.2 Greenland

The weather data used for this investigation of the effects in Greenland is measured global radiation and ambient temperature from 3 different locations on the west coast of Greenland, Nuuk, Sisimiut and Uummannaq see Figure 4.3.

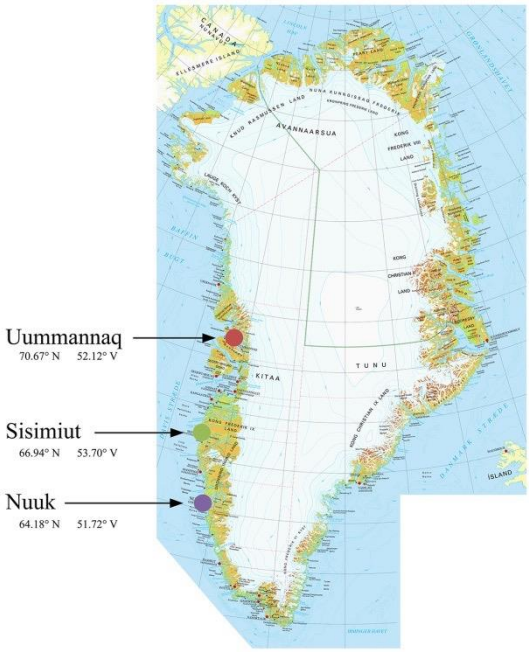

Figure 4.3 Locations investigated on the west coast of Greenland.

The measured weather data is from the time period 1991-2003. Unfortunately none of the stations have complete weather data sets. The measured global radiation is seen on Figure 4.4 were also the global radiation from each reference year is shown. The reference years are created in 2002 (Kragh et al. 2002), and selection of representative months is based on wind data which is especially seen for Nuuk were the global radiation from the reference year is much higher than the average global radiation from the measured data.

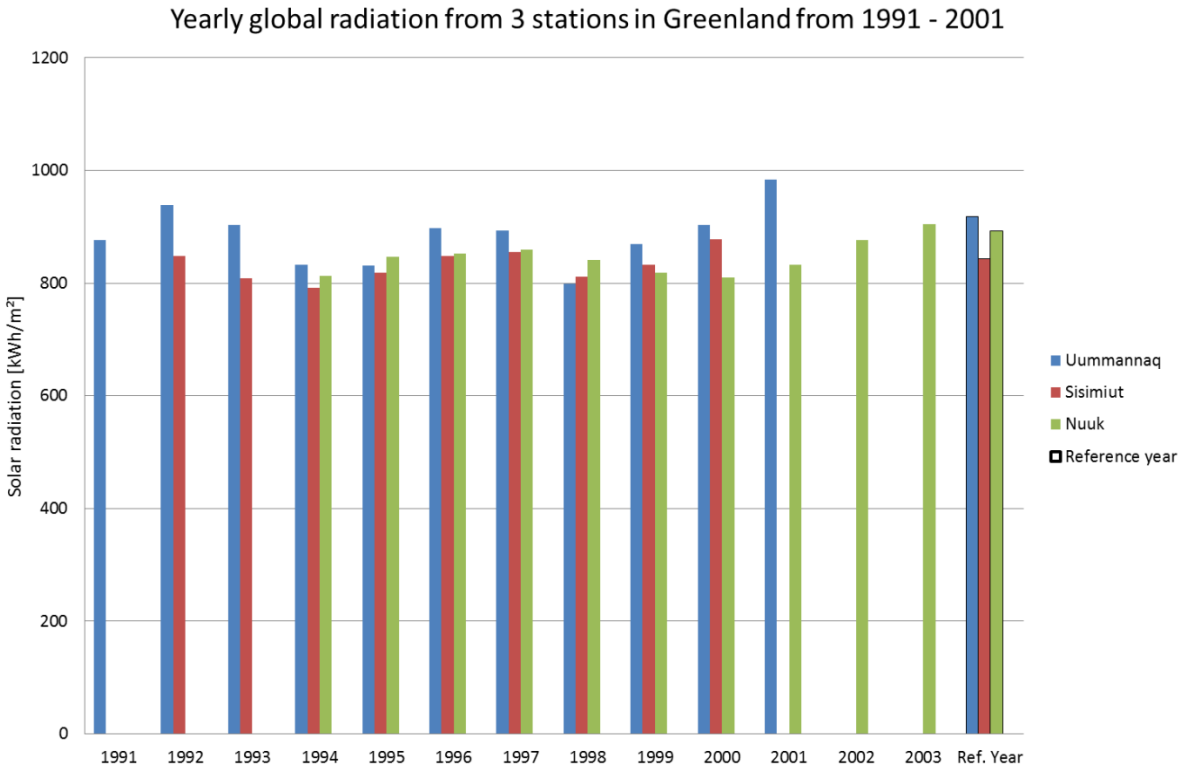

Figure 4.4 Yearly global radiation from the 3 locations in Greenland from the time period 1991-2003.

4.3 Solar Collector and calculations

The calculation of the thermal performance is carried out with a collector that has the efficien-

$$\eta = K_\theta \cdot \eta_0 - a_1 \cdot \frac{T_m - T_a}{G_{Ti}} - a_2 \cdot \frac{(T_m - T_a)^2}{G_{Ti}} \quad (1)$$

cy expression of:

The characteristics of the solar collector parameters can be seen in Table 4.1.

Table 4.1. Solar collector characteristics.

Solar collector characteristics			
First order heat loss coefficient	a_1	3.5	W/m²K
Second order heat loss coefficient	a_2	0	W/m²K²
Solar radiation on the collector	G_{Ti}	-	W/m²
Incidence angle coefficient in the equation $K_{diff}=1-\tan(\theta/2)^p$	p	3.4	-
Solar collector fluid mean temperature	T_m	40/60/80	°C
zero-loss efficiency	η_0	0.846	-

For Denmark the solar collectors are assumed to be tilted 40° and oriented due south, with a reflected irradiance calculated using the reflection coefficient of 0.2 of the ground.

For the locations in Greenland the tilt and orientation varies, see Table 4.2. The locations are influenced by the inland ice delaying the when sun rises above the ice.

Table 4.2. Collector tilt and orientation for the locations in Greenland.

Solar collector	Uummannaq	Sisimiut	Nuuk
Tilt	56 °	57 °	60 °
Orientation	10 °	13 °	5 °

The reflected irradiance is calculated using a reflection coefficient of 0.2 for the summer months and 0.7 for winter months. The definitions of summer and winter months are according to the recommendations given in (Dragsted et al. 2011).

No shadows are assumed for both Denmark and Greenland.

4.4 Results

The results of the investigation are presented here first with the Danish weather data with focus on the stationary solar collector followed by the results from the tracking solar collector. The results from the Greenland will follow.

4.4.1 Denmark

Stationary solar collector

The thermal performance is calculated with a mean solar collector fluid of 40°C, 60°C and 80°C. The results of the yearly thermal performances for all the years are shown in Figure 4.5 for the 6 different locations and with the mean solar collector fluid temperatures of 40°C, 60°C and 80°C.

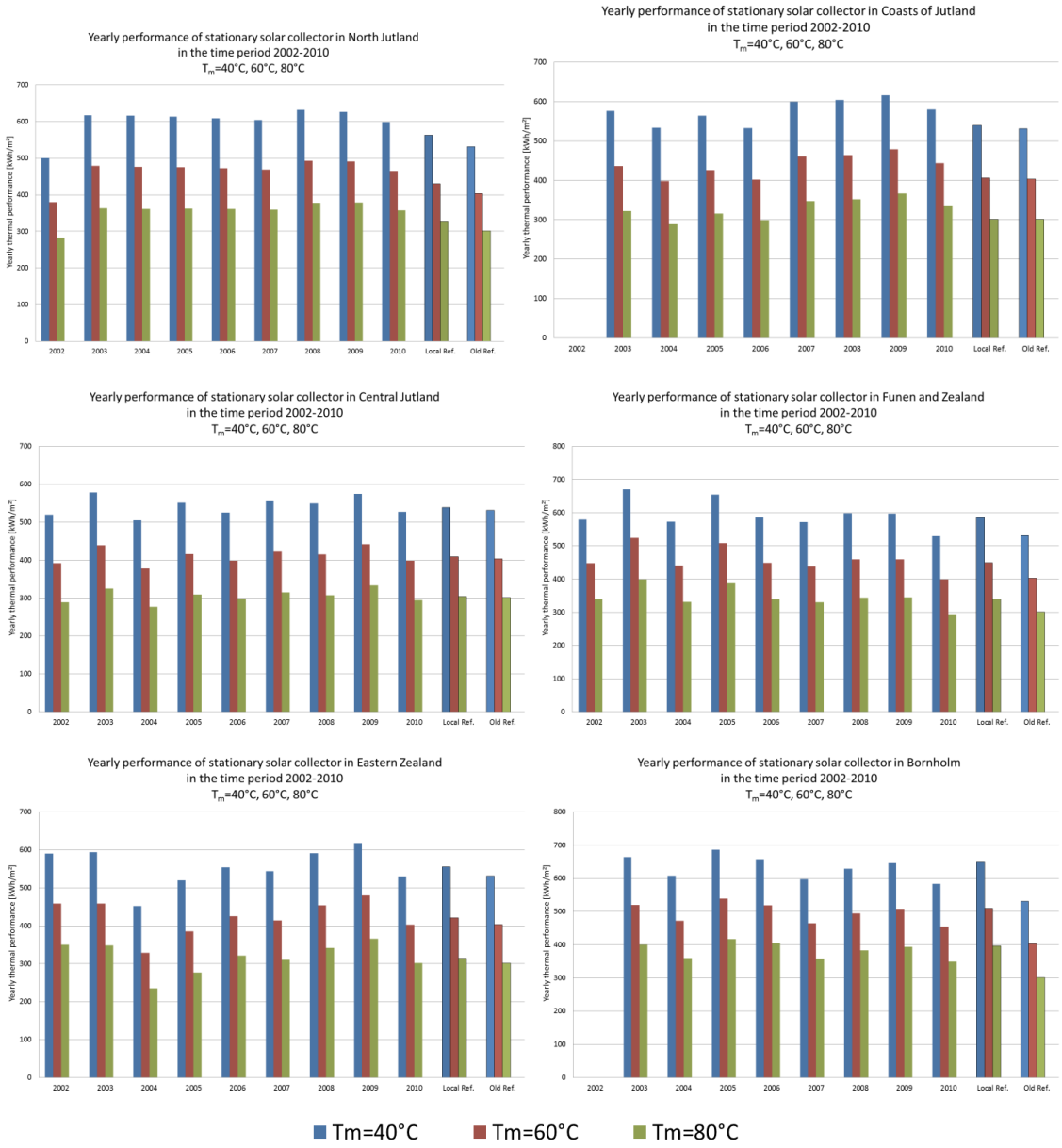

Figure 4.5 The yearly performance from a stationary solar collector for each of the locations chosen in Denmark from the time period 2002-2010.

The highest performance is as expected seen for Bornholm followed by Funen and Zealand and for all locations a mean solar collector fluid temperature of 40 °C gives the highest performance compared with the result of 60 °C and 80 °C. The figure shows that there is a strong dependency on the mean solar collector fluid temperature on the performance of the solar collectors.

The yearly thermal performance of the a stationary solar collector as a function of yearly global radiation in shown in Figure 4.6, Figure 4.7 and Figure 4.8 for the mean solar collector fluid of 40°C, 60 °C and 80 °C.

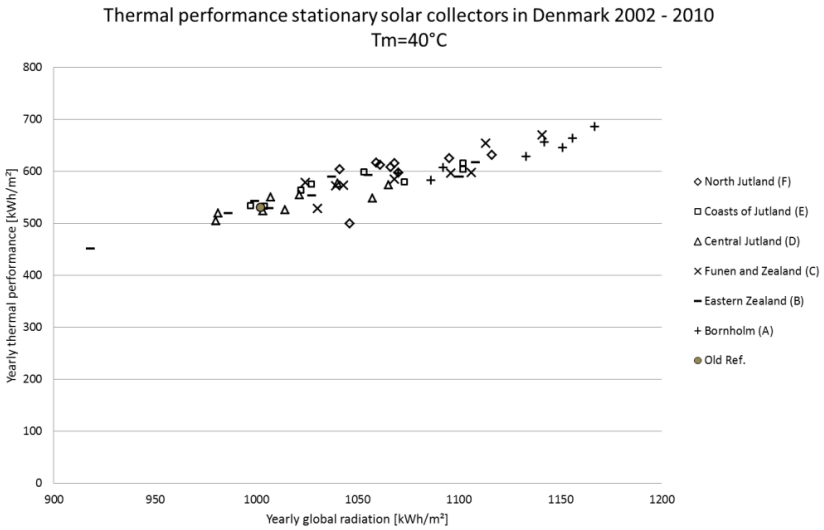

Figure 4.6 The thermal performance of a stationary solar collector as a function of the yearly global radiation in Denmark with a mean solar collector fluid temperature Tm=40°C.

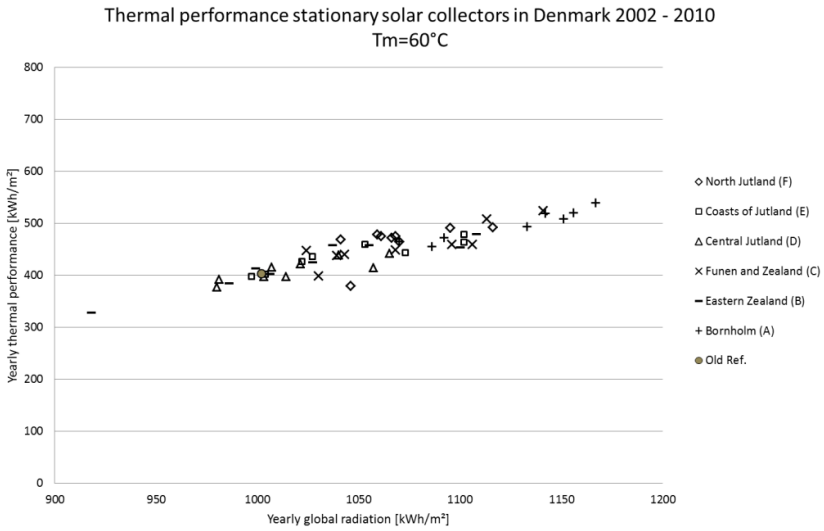

Figure 4.7 The thermal performance of a stationary solar collector as a function of the yearly global radiation in Denmark with a mean solar collector fluid temperature Tm=60°C.

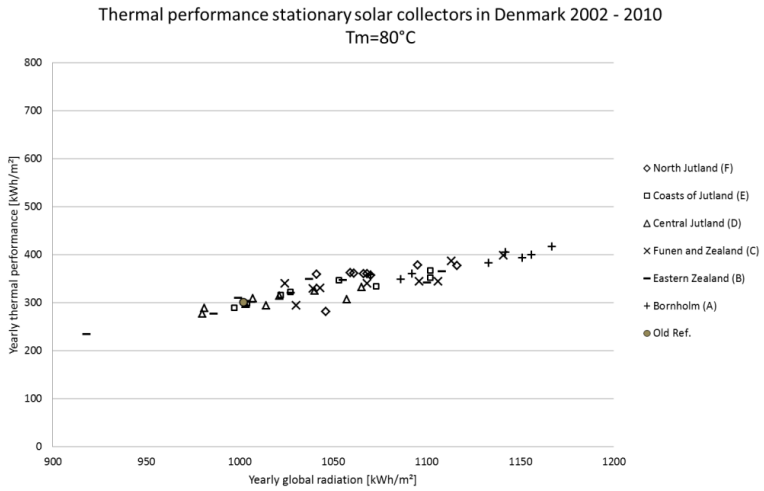

Figure 4.8 The thermal performance of a stationary solar collector as a function of the yearly global radiation in Denmark with a mean solar collector fluid temperature Tm=80°C.

Despite the difference in location, the figures show linear correlations between the yearly thermal performances and the yearly global radiations regardless of the mean solar collector fluid temperature.

The figures also show the effects of the mean solar collector fluid temperature, where an increase in temperature naturally will result in lower thermal performance.

The deviations in yearly thermal performance for each of the different stations compared to the old Danish reference year are seen in Table 4.3. The largest deviations are seen for 'Bornholm' and 'Eastern Zealand'. The large variation in thermal performances in 'Bornholm' is because of the big difference in global radiation for this location compared to the old Danish reference year, which was based on data from Eastern Zealand. For 'Eastern Zealand' the difference is mostly due to the low measured global radiation in 2004 for this location. Table 4.3. Deviation of yearly thermal performance of a stationary solar collector in 2002-2010 for each location in Denmark compared to the performance based on calculations with the old Danish reference year shows the deviation of yearly thermal performance of a stationary solar collector in 2001-2010 for each location in Denmark. For all locations the deviations become larger with an increasing mean solar collector fluid temperature.

Table 4.3. Deviation of yearly thermal performance of a stationary solar collector in 2002-2010 for each location in Denmark compared to the performance based on calculations with the old Danish reference year.

	Mean solar collector fluid temperature		
Location	T_m = 40°C	T_m = 60°C	T_m = 80°C
North Jutland	-6% to 19%	-6% to 22%	-6% to 26%
Coasts of Jutland	0% to 16%	-1% to 19%	-4% to 22%
Central Jutland	-11% to 9%	-13% to 10%	-16% to 11%
Fuenen and Zealand	0% to 26%	-1% to 30%	-2% to 33%
Eastern Zealand	-15% to 16%	-18% to 19%	-22% to 22%
Bornholm	10% to 29%	13% to 34%	16% to 39%

The comparisons between thermal performances of stationary solar collector calculations with the new local reference years and with the measured solar radiation data from 2002 to 2010 are seen in Table 4.4. Here the deviations are smallest for 'Bornholm' and 'Central Jutland', which is because these locations have the least variation in the measured yearly global radiation in the period from 2002-2012.

Table 4.4. Deviation of yearly thermal performance of a stationary solar collector in 2002-2010 for each location in Denmark compared to the performance based on calculations with the New local Danish reference years.

	Mean solar collector fluid temperature		
Location	T_m = 40°C	T_m = 60°C	T_m = 80°C
North Jutland	-11% to 12%	-12% to 15%	-13% to 17%
Coasts of Jutland	-1% to 14%	-2% to 18%	-4% to 22%
Central Jutland	-6% to 7%	-8% to 8%	-9% to 10%
Fuenen and Zealand	-10% to 15%	-11% to 17%	-13% to 18%
Eastern Zealand	-19% to 11%	-22% to 14%	-25% to 17%
Bornholm	-10% to 6%	-11% to 6%	-12% to 5%

The yearly utilization of solar radiation is shown on Figure 4.9 for varying mean solar collector fluid temperatures. The figure shows a linear increase in utilization with an increase in yearly global radiation. There is a slightly greater increase in the utilization of solar irradiance for the mean solar collector fluid temperature of 80°C compared to the lower temperatures.

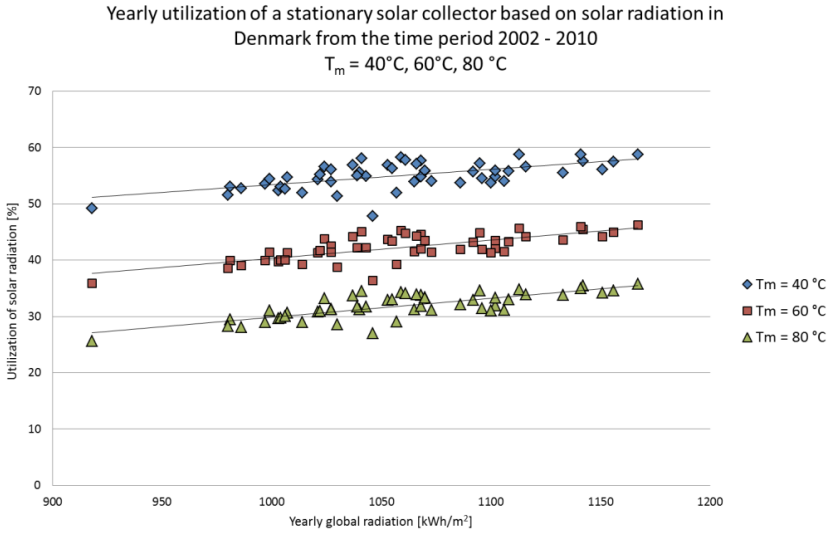

Figure 4.9 Yearly utilization of solar radiation in Denmark for 2002-2010 for a stationary solar collector with a mean solar collector fluid temperature Tm=40°C, 60°C, 80°C.

Tracking solar collector

The results of the yearly thermal performance of tracking solar collectors based on the weather data from the 6 locations in Denmark are shown on Figure 4.10 for mean solar collector fluid temperatures of 40 °C, 60 °C and 80 °C.

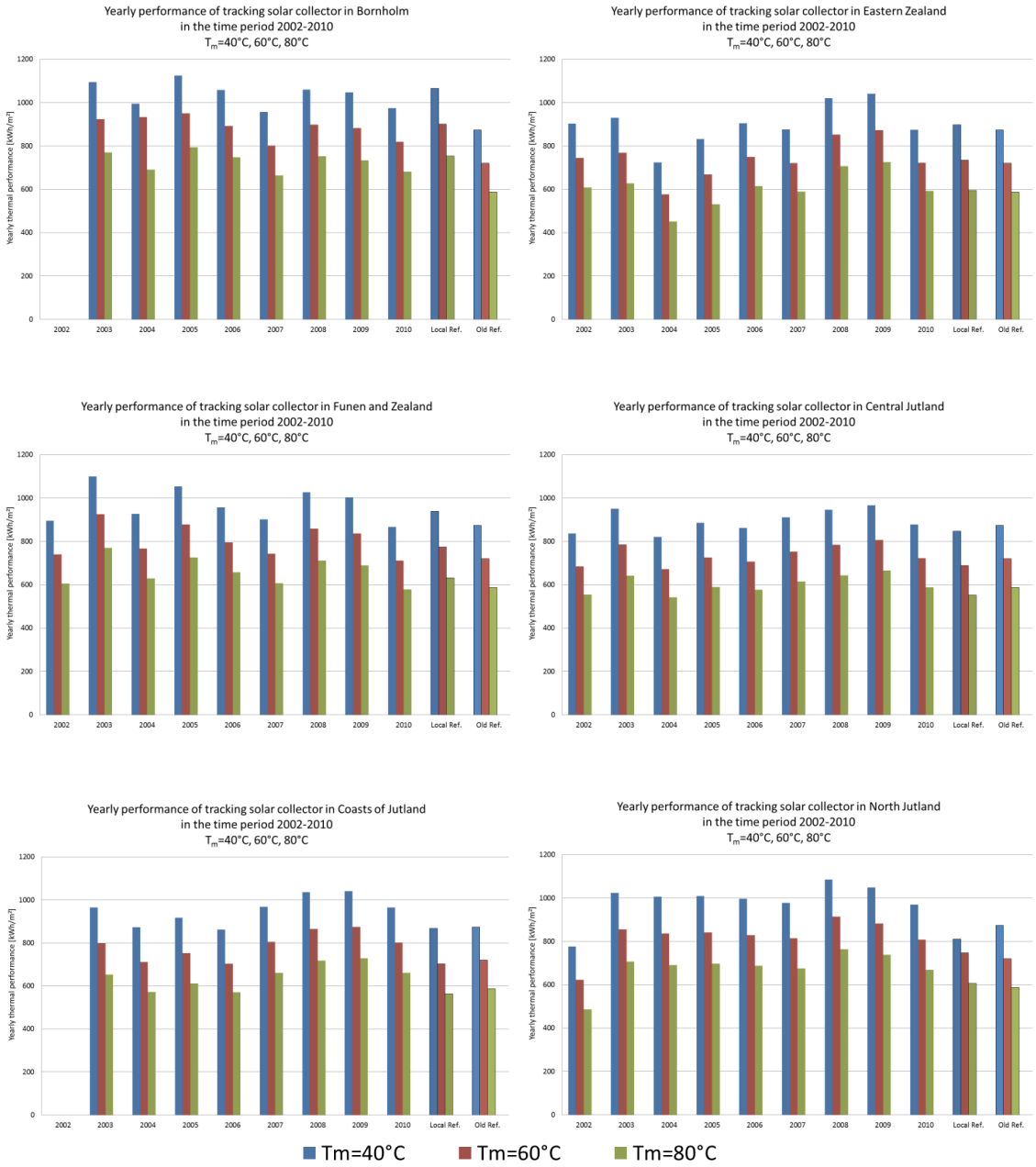

Figure 4.10 The yearly performance from a tracking solar collector for each of the locations chosen in Denmark from the time period 2002-2010.

The figure shows that Bornholm again has the highest performance, and it also shows that the large variation in performance for the different locations seen with the stationary solar collector is minimized with the tracking solar collector. The dependency of the mean solar collector fluid temperature is slightly decreased compared with the results from a stationary solar collector.

The yearly thermal performance of the tracking solar collector as a function of the yearly global radiation is shown on Figure 4.11, Figure 4.12 and Figure 4.13 for mean solar collector fluid temperatures of 40 °C, 60 °C and 80 °C.

The results show a stronger dependency of the global radiation, which is seen with steep incline of the results regardless of the location. This is true for all 3 calculated mean solar collector temperatures.

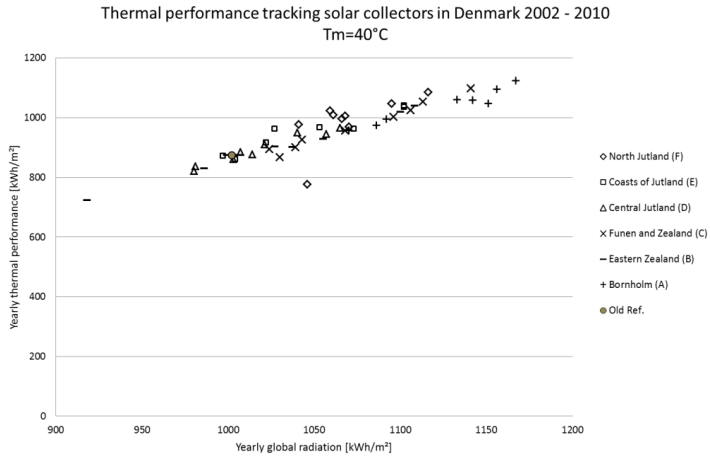

Figure 4.11 The thermal performance of a tracking solar collector as a function of the yearly global radiation in Denmark with a mean solar collector fluid temperature Tm=40°C.

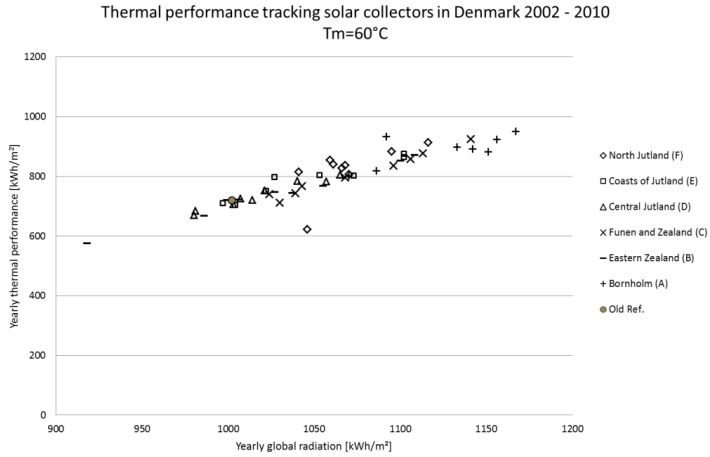

Figure 4.12 The thermal performance of a tracking solar collector as a function of the yearly global radiation in Denmark with a mean solar collector fluid temperature Tm=60°C.

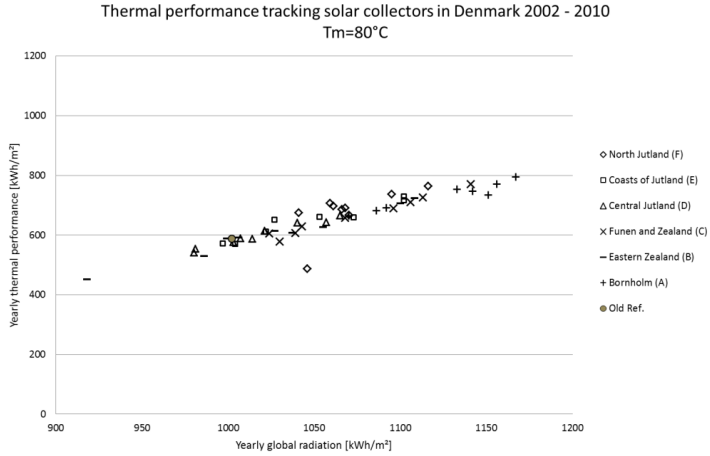

Figure 4.13 The thermal performance of a tracking solar collector as a function of the yearly global radiation in Denmark with a mean solar collector fluid temperature Tm=80°C.

The deviation in the yearly thermal performance for each of the locations compared with the

old Danish reference year is shown in Table 4.5. The largest deviation is again seen for Bornholm caused by the big difference in global radiation from Bornholm and the old reference year where the data is from Zealand.

Again for all locations the deviation becomes larger with an increasing mean solar collector fluid temperature.

Table 4.5. Deviation of yearly thermal performance of a tracking solar collector in 2002-2010 for each location in Denmark compared to the performance based on calculations with the old Danish reference year.

	Mean solar collector fluid temperature		
Location	T_m = 40°C	T_m = 60°C	T_m = 80°C
North Jutland	-11% to 24%	-14% to 27%	-17% to 30%
Coasts of Jutland	-1% to 19%	-2% to 22%	-4% to 24%
Central Jutland	-16% to 11%	-18% to 12%	-20% to 13%
Fuenen and Zealand	-2% to 26%	-3% to 28%	-3% to 31%
Eastern Zealand	-17% to 19%	-20% to 21%	-23% to 24%
Bornholm	9% to 29%	11% to 32%	13% to 35%

Table 4.6 shows the comparison between the results with the real weather data and the new local reference years. The deviation becomes smaller than when the results are compared with the old reference year which is because the global radiation in the new local reference years is a better representative for each location.

Table 4.6. Deviation of yearly thermal performance of a tracking solar collector in 2002-2010 for each location in Denmark compared to the performance based on calculations with the New local Danish reference years.

	Mean solar collector fluid temperature		
Location	T_m = 40°C	T_m = 60°C	T_m = 80°C
North Jutland	-4% to 34%	-17% to 22%	-20% to 26%
Coasts of Jutland	-1% to 20%	0% to 24%	0% to 29%
Central Jutland	-3% to 14%	-2% to 17%	-2% to 21%
Fuenen and Zealand	-8% to 17%	-8% to 20%	-8% to 22%
Eastern Zealand	-19% to 16%	-22% to 19%	-24% to 22%
Bornholm	-10% to 5%	-11% to 5%	-12% to 5%

The yearly utilization of solar radiation as a function of the yearly global radiation is shown on Figure 4.14 for mean solar collector fluid temperature of 40 °C, 60 °C and 80 °C. The figure shows a linear increase in utilization with increase in yearly global radiations.

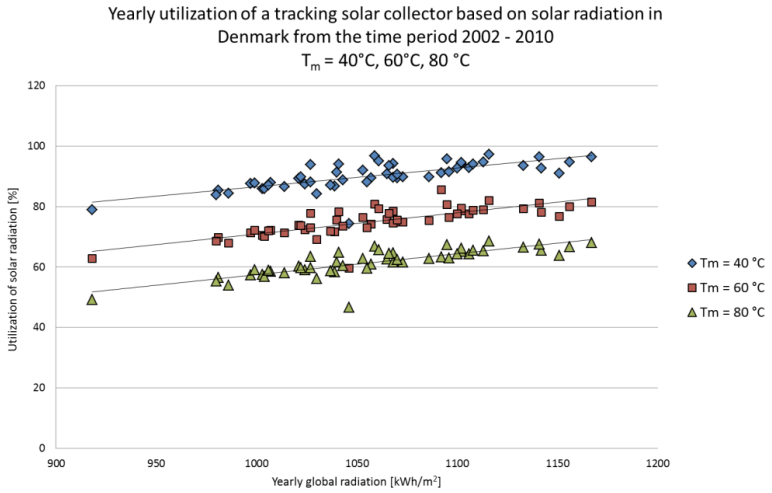

Figure 4.14 Yearly utilization of solar radiation in Denmark for 2002-2010 for a tracking solar collector with a mean solar collector fluid temperature Tm=40°C, 60°C, 80°C.

4.4.2 Greenland

Stationary solar collector

The calculated thermal performance of a stationary solar collector in 3 locations in Greenland is shown on Figure 4.15. The results from Nuuk shown a much larger performance based on the reference year compared with the real weather data. This is due to the fact that the months in the reference year are selected based on wind velocities and not solar radiation, causing the months chosen to have unrealistically large solar radiation. The same is also true for Uummannaq, where the effect of too high solar radiation data is present, but not to the same extent as Nuuk. For Sisimiut the results show that the selected months in the reference year are a better match to the measured solar radiation.

The results also show that the highest performance is seen for Uummannaq with an average yearly thermal performance around 500 kWh/m², which is explained with the higher global radiation at this location.

Figure 4.16, Figure 4.17 and Figure 4.18 show the yearly thermal performance as a function of the yearly global radiation for Nuuk, Sisimiut and Uummannaq with mean solar collector fluid temperature of 40 °C, 60 °C and 80 °C.

The figures show the same linear dependency between the yearly performance and the yearly global radiation for all three locations in Greenland, as seen for the locations in Denmark. The trends seen in Greenland has a smaller incline compared with the results from Denmark, which means that the thermal performance dependency on the global radiation is slightly less in Greenland.

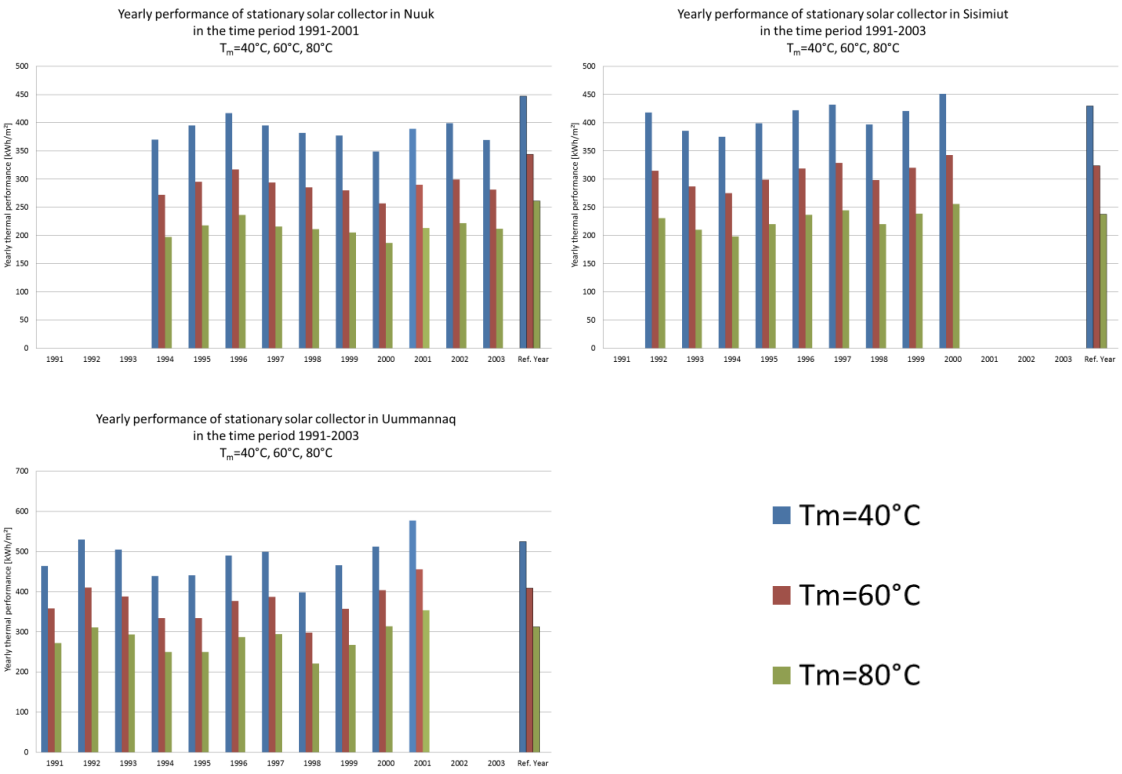

Figure 4.15 The yearly performance from a stationary solar collector for each of the locations in Greenland from the time period 1991-2003.

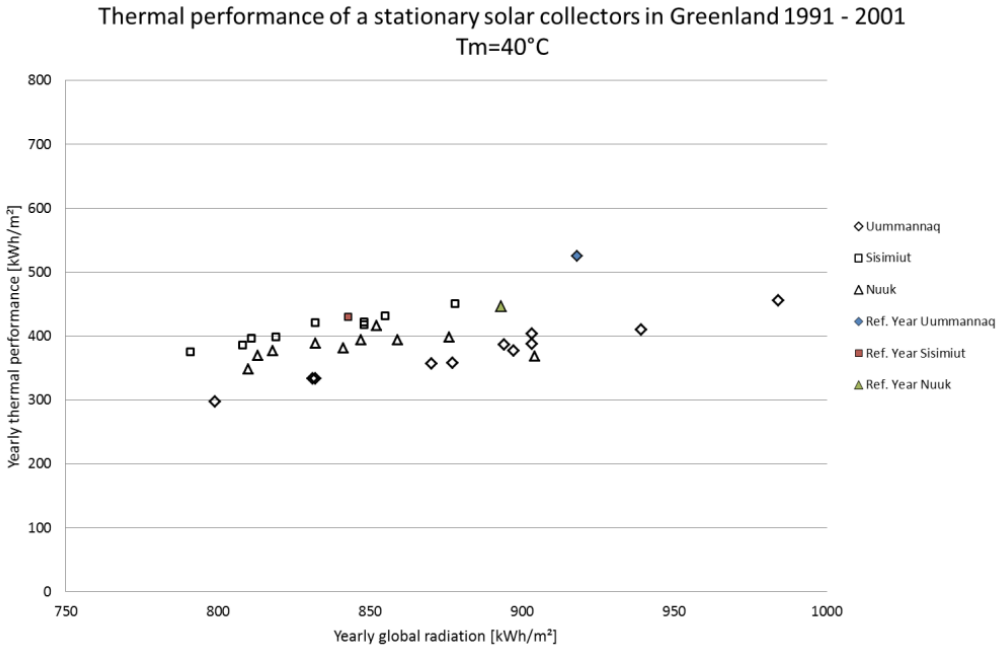

Figure 4.16 The thermal performance of a stationary solar collector as a function of the yearly global radiation in Greenland with a mean solar collector fluid temperature T_m=40°C.

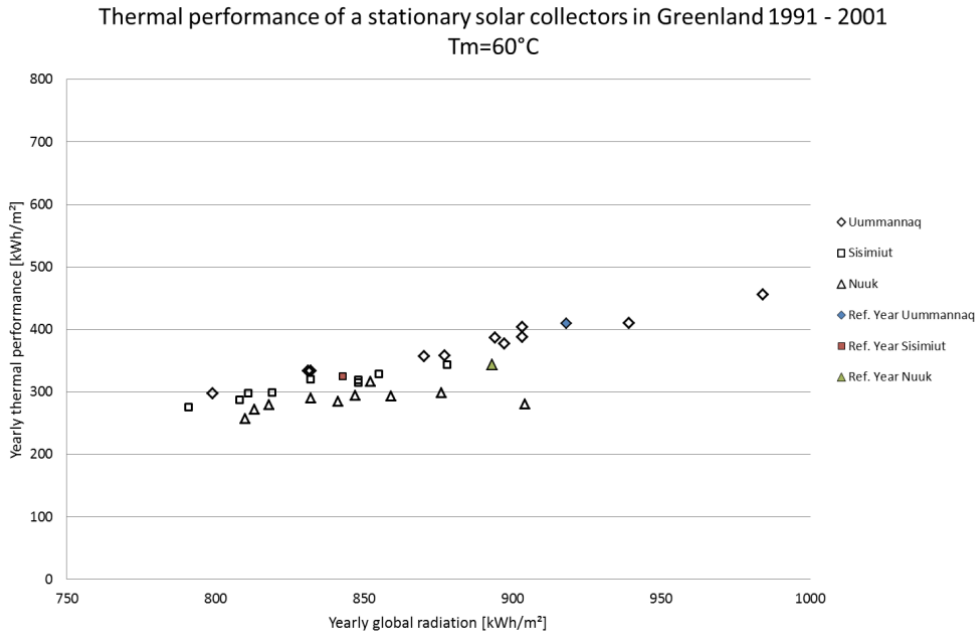

Figure 4.17 The thermal performance of a stationary solar collector as a function of the yearly global radiation in Greenland with a mean solar collector fluid temperature Tm=60°C.

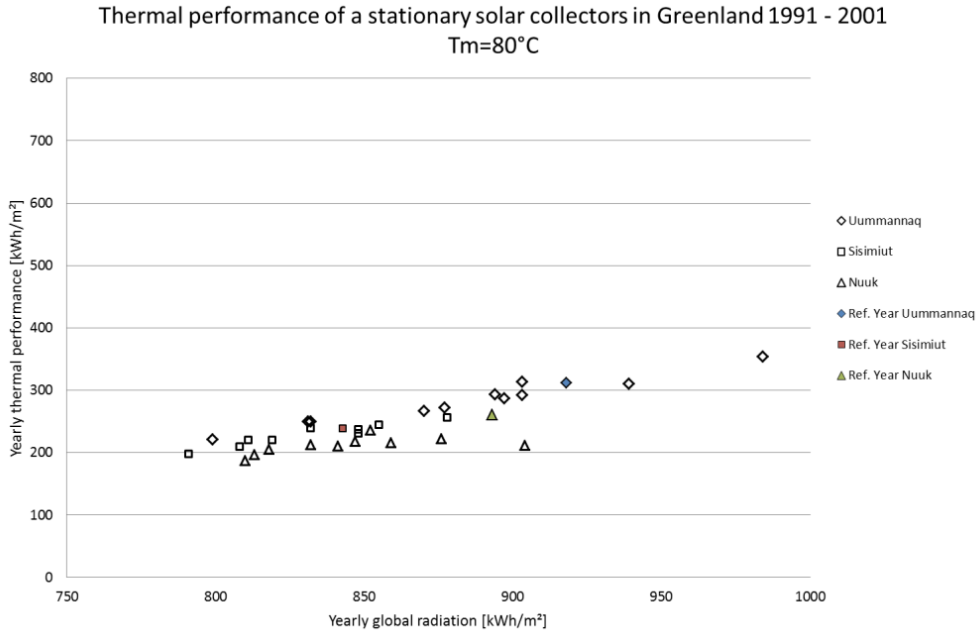

Figure 4.18 The thermal performance of a stationary solar collector as a function of the yearly global radiation in Greenland with a mean solar collector fluid temperature Tm=80°C.

The deviations between the result from the real weather data and the results from the local reference years are shown in Table 4.7. The highest deviation is seen for Uummannaq with a mean solar collector fluid temperature of 80 °C. As seen for Denmark the deviation increases with higher mean solar collector fluid temperature.

Table 4.7. Deviation of yearly thermal performance of a stationary solar collector in 1991-2003 for the locations in Greenland compared to the performance based on calculations with the local reference years for Nuuk, Sisimiut and Uummannaq.

	Mean solar collector fluid temperature		
Location	T_m = 40°C	T_m = 60°C	T_m = 80°C
Nuuk	-22% to -7%	-25% to -8%	-28% to -10%
Sisimiut	-15% to 5%	-15% to 6%	-17% to 8%
Uummannaq	-24% to 10%	-27% to 11%	-29% to 13%

The yearly utilization of solar radiation is shown on Figure 4.19 for varying mean solar collector fluid temperature. The same trends seen in Denmark are seen in Greenland with an increase in utilization with an increase in solar radiation. The dependency is stronger in Greenland as the steeper incline of trends shows.

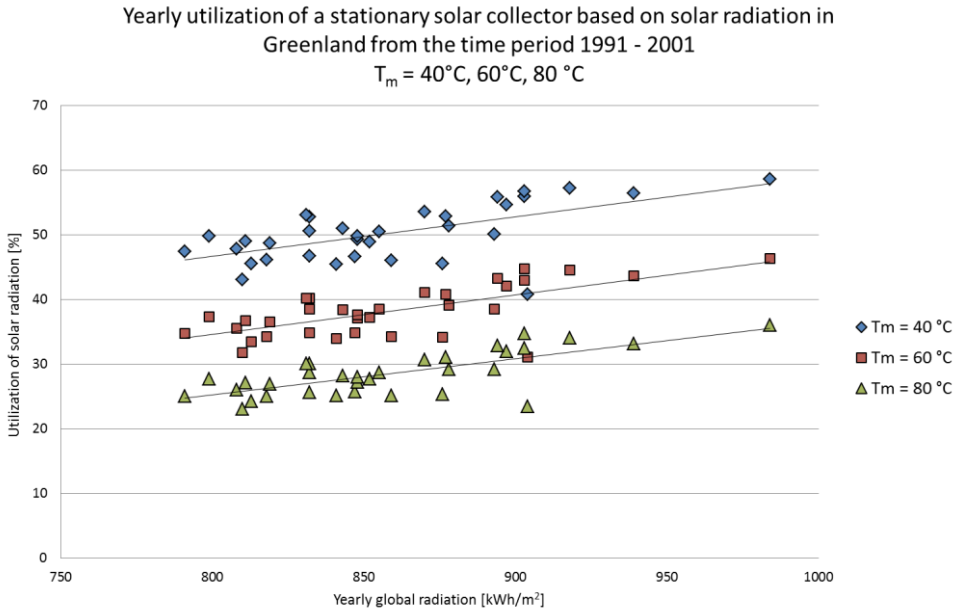

Figure 4.19 Yearly utilization of solar radiation in Greenland for1991-2003 for a stationary solar collector with a mean solar collector fluid temperature Tm=40°C, 60°C, 80°C.

Tracking solar collector

The calculations of a tracking solar collector with the Greenlandic weather data is shown on Figure 4.20 for mean solar collector fluid temperatures of 40 °C, 60 °C and 80 °C. The results show as expected an increase in performance with Uummannaq having the highest performance.

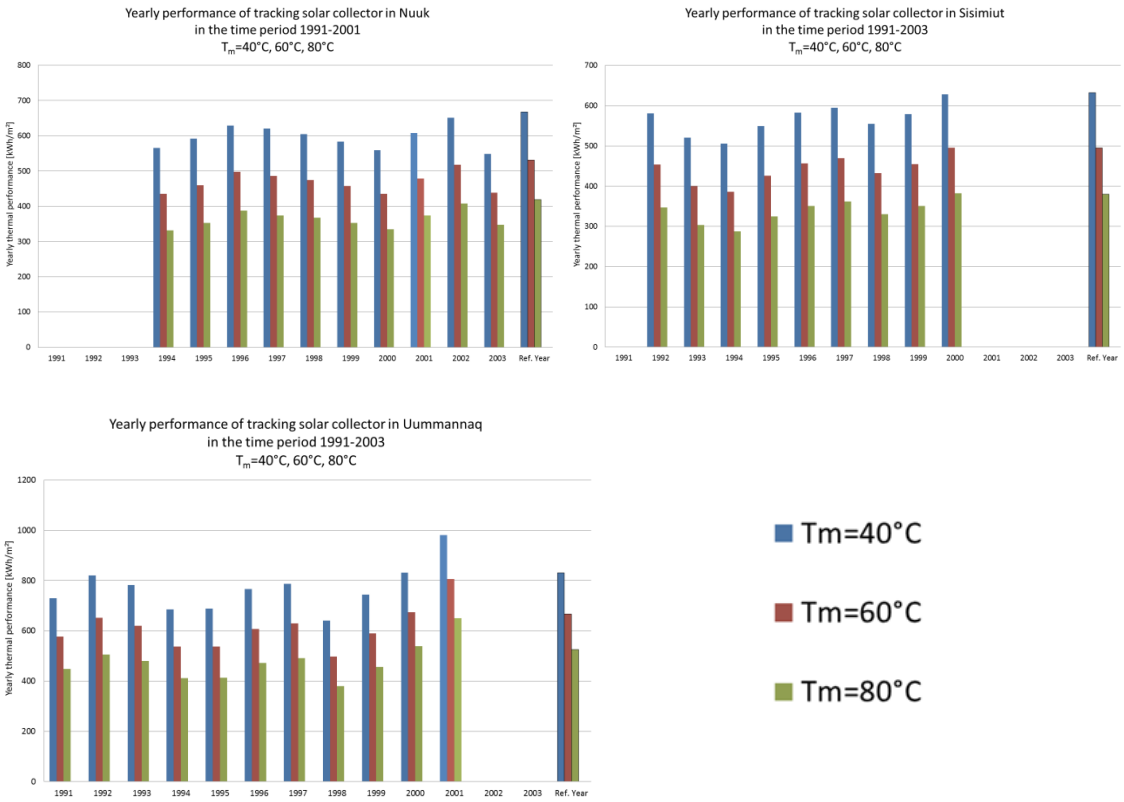

Figure 4.20 The yearly performance from a tracking solar collector for each of the locations in Greenland from the time period 1991-2003.

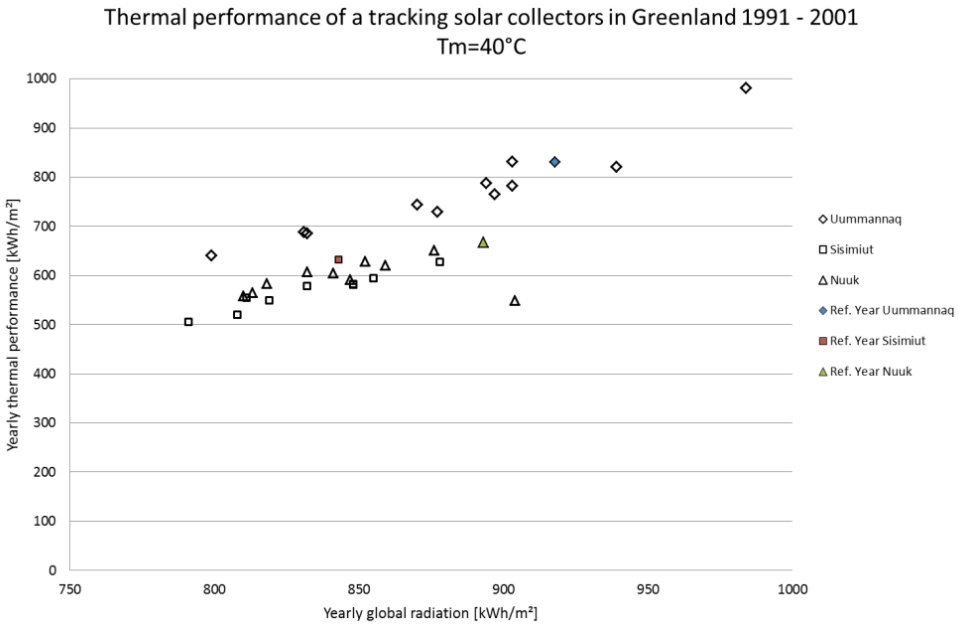

Figure 4.21 The thermal performance of a tracking solar collector as a function of the yearly global radiation in Greenland with a mean solar collector fluid temperature Tm=40°C.

The yearly thermal performance of a tracking solar collector with mean solar collector fluid temperature of 40 °C, 60 °C and 80 °C as a function of the yearly global radiation is shown on Figure 4.21, Figure 4.22 and Figure 4.23. With a tracking solar collector the dependency on the solar radiation for the thermal performance is higher compared with a stationary solar collector, which is the same seen in the results based on the Danish weather data.

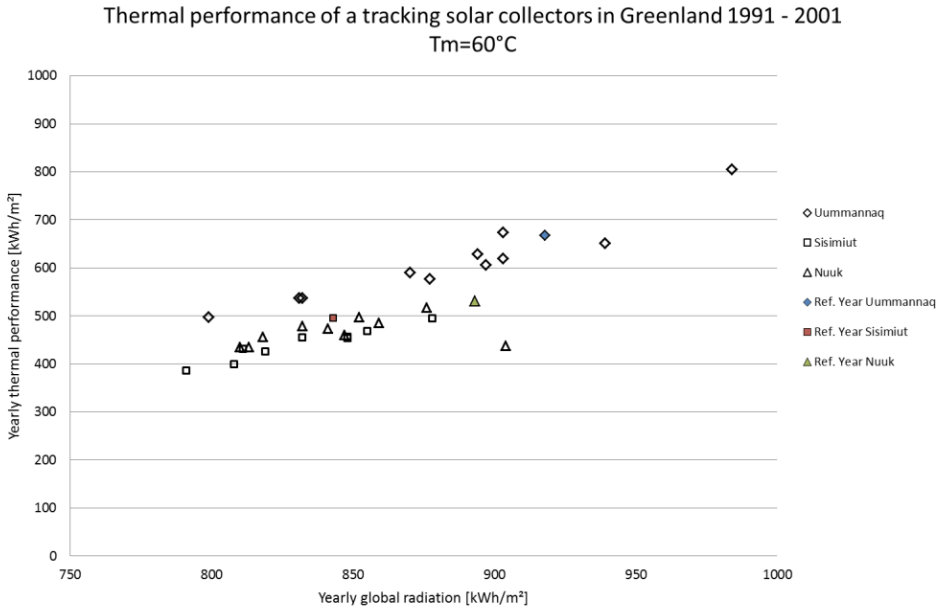

Figure 4.22 The thermal performance of a tracking solar collector as a function of the yearly global radiation in Greenland with a mean solar collector fluid temperature Tm=60°C.

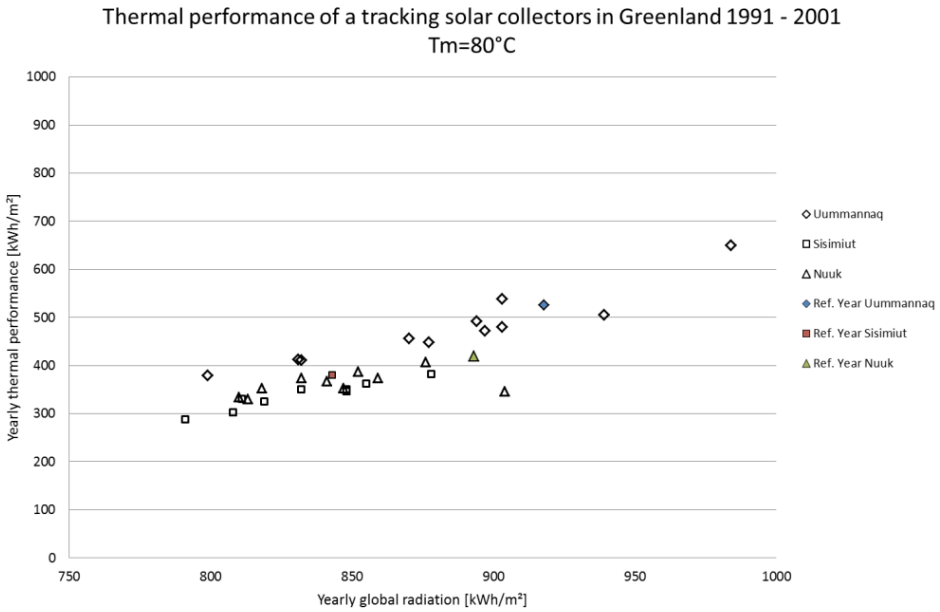

Figure 4.23 The thermal performance of a tracking solar collector as a function of the yearly global radiation in Greenland with a mean solar collector fluid temperature Tm=80°C.

The deviation between the results from the real weather data and the results based on the reference year is seen in Table 4.8. Again the results from Uummannaq have the highest deviation and again the deviation is higher for the tracking solar collector compared with the deviation with the stationary solar collector, as was the case for the Danish weather data.

Table 4.8. Deviation of yearly thermal performance of a rotating solar collector in 1991-2003 for the locations in Greenland compared to the performance based on calculations with the local reference years for Nuuk, Sisimiut and Uummannaq.

	Mean solar collector fluid temperature		
Location	T_m = 40°C	T_m = 60°C	T_m = 80°C
Nuuk	-18% to -3%	-18% to -2%	-21% to -3%
Sisimiut	-20% to -1%	-22% to 0%	-24% to 1%
Uummannaq	-23% to 18%	-25% to 21%	-28% to 24%

The yearly utilization of solar radiation is shown in Figure 4.24 for varying mean solar collector fluid temperatures of 40 °C, 60 °C and 80 °C. Again the figure shows a linear dependency between the yearly global radiation and the utilization. For the Greenlandic location a tracking solar collector has a higher increase in utilization with increasing solar radiation compared with the Danish locations.

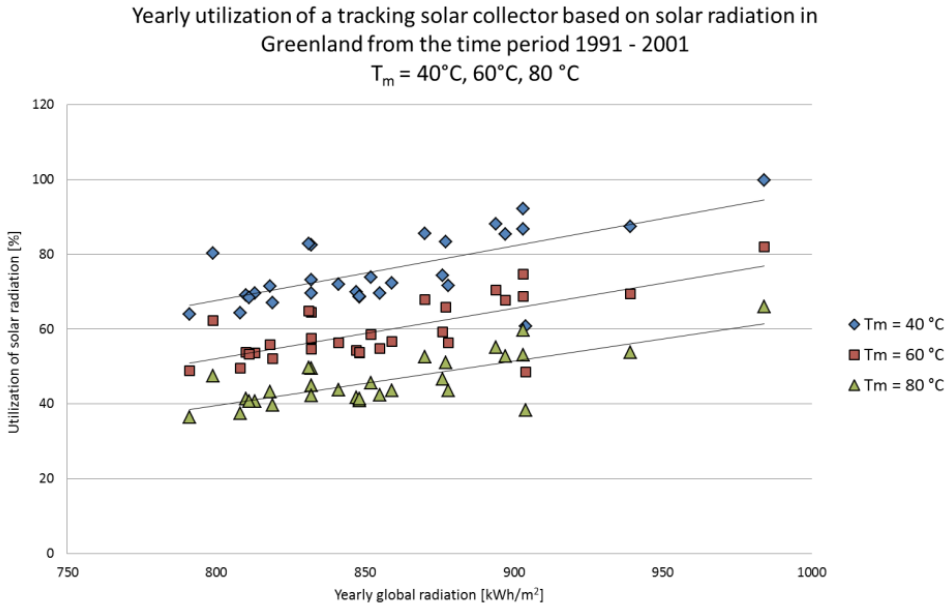

Figure 4.24 Yearly utilization of solar radiation in Greenland for1991-2003 for a tracking solar collector with a mean solar collector fluid temperature Tm=40°C, 60°C, 80°C.

4.5 Conclusions

The calculated thermal performances of solar collectors using the new local reference years from Denmark are higher than the calculated thermal performances of solar collectors using the old Danish reference year. This is due to the increased solar radiation (Skalík et al. 2012). The comparison of the calculated thermal performance with the old Danish reference year and the thermal performance based on the measured weather data revealed a deviation of up to 39 % for a mean solar collector fluid temperature of 80 °C. The deviation is mostly due to the large difference in solar irradiance at different locations in Denmark.

The maximum deviations of yearly thermal performance of solar collectors for real weather data years compared to yearly thermal performance for the new reference years are between -25% and +29%. That is: Relative large deviations in thermal performance of solar collectors can be expected. Furthermore, the variation in yearly thermal performance from year to year is strongly depending on the location, even in Denmark, which is a small country.

For Greenland the maximum deviation between the thermal performance of solar collectors for real years compared to yearly thermal performance for the reference years are between -

2% and +24%. The variations are the same range as the variations in Denmark.

The results have shown that using the old reference year and the new local reference years for Denmark and Greenland will leave out the significant deviations in the thermal performance of the solar collectors that occur in untypical meteorological months.

The investigation also shows that the utilization of the solar radiation increases with the global radiation. This means that in addition to the obvious increase in thermal performance with increasing solar radiation, the utilization of the solar radiation also increases. This increase in utilization is higher in Greenland than in Denmark.

4.6 References

Dragsted, J. Solar heating in Greenland – Resources assessment and potential. PhD Thesis 2011.

Furbo S, Dragsted J. Solar radiation and thermal performance of solar collectors for Denmark. DTU Civil Engineering Report R-275; 2012.

Jensen J M, Lund H. Design reference year, DRY –et nyt dansk referenceår. Laboratoriet for varmeisolering, Technical University of Denmark. Meddelelse Nr. 281; 1995.

Kragh J, Nielsen T, Svendsen S. Grønlandsk vejrdata Nuuk Uummannaq, Technical University of Denmark, November 2002

Kragh J, Pedersen F, Svendsen S. Weather Test Reference Years of Greenland, Technical University of Denmark.

Skalík L, Lulkovicova O, Furbo S, Perers B, Dragsted J, Nielsen K. P, Scharling M, Carlund T, Evaluation og long-term global radiation measurements in Denmark and Sweden. Eurosun, Rijeka Croatia, 2012.

Skartveit A, Olseth J.A., An hourly diffuse fraction model with correction for variability and surface albedo, Solar Energy Vol. 63 No. 3, pp. 173-183, 1998.

5. Extension of the Danish Design Reference Year (DRY) with directional horizontal diffuse irradiances

5.1 Introduction

This section describes the work carried out in WP7 'Extension of the Danish Design Reference Year, DRY with directional horizontal diffuse irradiances'. The aim is here to derive mathematical equations for the directional diffuse solar irradiance measurements from the different parts of the sky dome and replace the existing isotropic equation in DRY with the new directional equations.

The mathematical equations are derived from the analysis of 1-minute fractional measurements from the (1/8) pyranometers for one year from March 2015 to February 2016.

5.2 Results

The results of the investigation are presented in graphs showing the diffuse fraction, Id/I against the clear sky index, 〉. Further the results are presented in tables showing the mathematical equations for different intervals of the clear sky index, 〉 and the distance between solar azimuth, SA and dome azimuth, DA.

The mathematical equations are obtained by fitting the measured data for different intervals of 〉. Due to shading from the domes, the measured data are only given for certain distances between solar azimuth, SA and dome azimuth, DA. Measured data from the areas shaded by the domes are ignored. Instead, these areas are represented by mathematical equations derived as average of the mathematical equations derived from the unshaded measurements. The mathematical equations are given for the following distances between solar azimuth, SA and dome azimuth, DA:

-15.3° ≤ SA-DA ≤ 15.3°:	equation derived from measured data
|15.3°| < SA-DA < |29.7°|:	equation averaged from measurements from -15.3° ≤ SA-DA ≤ 15.3° and |29.7°| ≤ SA-DA ≤ |60.3°|
|29.7°| ≤ SA-DA ≤ |60.3°|:	equation derived from measured data
|60.3°| < SA-DA < |74.7°|:	equation averaged from measurements from |29.7°| ≤ SA-DA ≤ |60.3°| and |74.7°| ≤ SA-DA ≤ |180°|
|74.7°| ≤ SA-DA ≤ |180°|:	equation derived from measured data

Note that the number of intervals of the distances between solar azimuth, SA and dome azimuth, DA has been reduced from 16 possible intervals to only 5. The reason is that the diffuse fraction does not change from one interval to the next when the distances between solar azimuth, SA and dome azimuth, DA is larger than 75°.

Figure 5.1 – 5.3 show the graphical representation of the mathematical equations of the diffuse fraction against 〉 for the different intervals of the distances between solar azimuth, SA and dome azimuth, DA.

Table 5.1 – 5.5 show the mathematical equations of the diffuse fraction against 〉 for the different intervals of the clear sky index, 〉 and the distances between solar azimuth, SA and dome azimuth, DA.

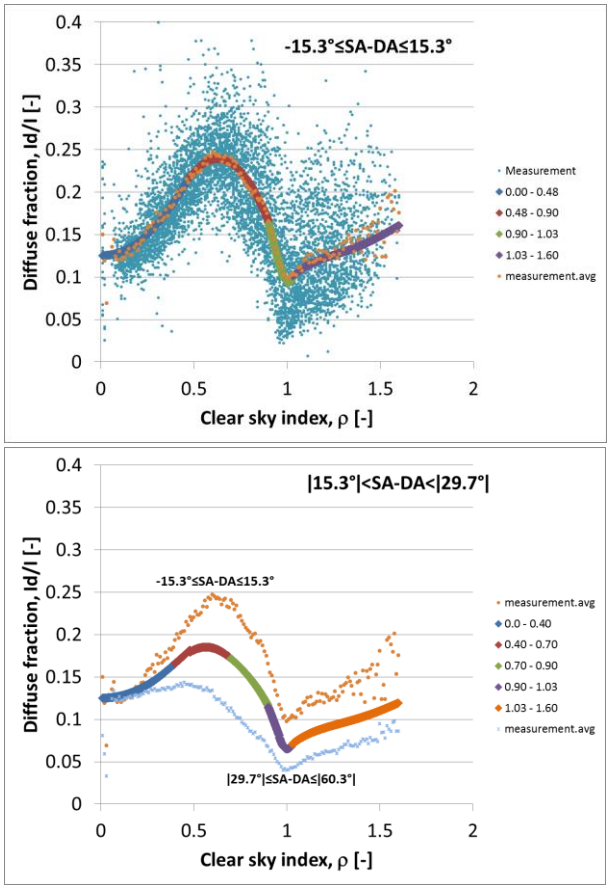

Figure 5.1: Diffuse fraction as function of clear sky index for different distances between solar azimuth, SA and dome azimuth, DA. Left: -15.3° ≤ SA-DA ≤ 15.3°. Right: |15.3°| < SA-DA < |29.7°|.

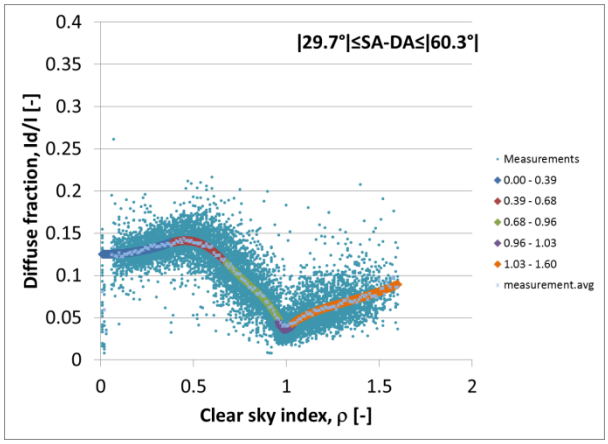

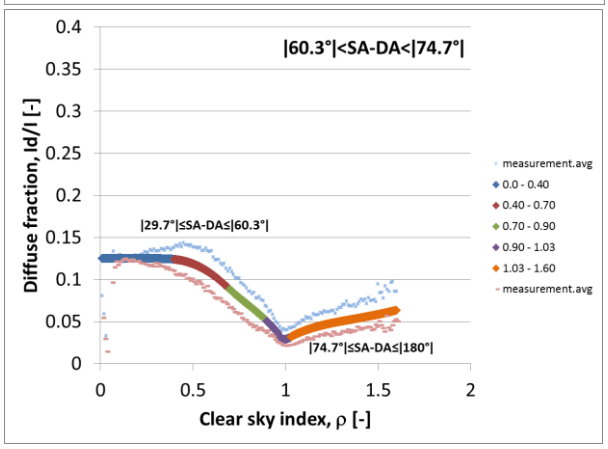

Figure 5.2: Diffuse fraction as function of clear sky index for different distances between solar azimuth, SA and dome azimuth, DA. Left: |29.7°| ≤ SA-DA ≤ |60.3°|. Right: |60.3°| < SA-DA < |74.7°|.

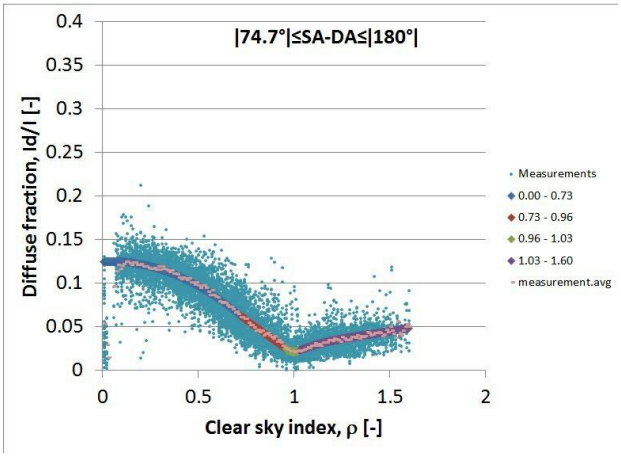

Figure 5.3: Diffuse fraction as function of clear sky index for the distance between solar azimuth, SA and dome azimuth, DA: |74.7°| ≤ SA-DA ≤ |180°|.

Table 5.1: Parametrizations of the diffuse fraction for distances between solar azimuth, SA and dome azimuth, DA in the interval: -15.3° ≤ SA-DA ≤ 15.3°.

These are also plotted in Figure 5.1.

-15.3° ≤ SA-DA ≤ 15.3°	
$0 \leq \rangle \leq 0.48$	$0.4372 \cdot \rangle^2 - 0.0081 \cdot \rangle + 0.125$
$0.48 < \rangle \leq 0.90$	$-0.9877 \cdot \rangle^2 + 1.2392 \cdot \rangle - 0.1497$
$0.90 < \rangle \leq 1.03$	$47.0464 \cdot \rangle^3 - 131.02 \cdot \rangle^2 + 120.75 \cdot \rangle - 36.682$
$1.03 < \rangle \leq 1.50$	$-0.7449 \cdot \rangle^4 + 4.294 \cdot \rangle^3 - 9.1154 \cdot \rangle^2 + 8.5756 \cdot \rangle - 2.912$

Table 5.2: Parametrizations of the diffuse fraction for distances between solar azimuth, SA and dome azimuth, DA in the interval: |15.3°| < SA-DA < |29.7°|. These are also plotted in Figure 5.1.

|15.3°| < SA-DA < |29.7°|	
$0 \leq \rangle \leq 0.40$	$0.2729\cdot\rangle^2 - 0.0069\cdot\rangle + 0.125$
$0.40 < \rangle \leq 0.70$	$-0.7277\cdot\rangle^2 + 0.8217\cdot\rangle - 0.0471$
$0.70 < \rangle \leq 0.90$	$-0.5349\cdot\rangle^2 + 0.5821\cdot\rangle + 0.0259$
$0.90 < \rangle \leq 1.03$	$47.928\cdot\rangle^3 - 135.04\cdot\rangle^2 + 126.18\cdot\rangle - 39.006$
$1.03 < \rangle \leq 1.50$	$-0.5439\cdot\rangle^4 + 3.163\cdot\rangle^3 - 6.8102\cdot\rangle^2 + 6.51\cdot\rangle - 2.2538$

Table 5.3: Parametrizations of the diffuse fraction for distances between solar azimuth, SA and dome azimuth, DA in the interval: |29.7°| ≤ SA-DA ≤ |60.3°|. These are also plotted in Figure 5.2.

|29.7°| ≤ SA-DA ≤ |60.3°|	
$0 \leq \rangle \leq 0.39$	$0.1112\cdot\rangle^2 - 0.0064\cdot\rangle + 0.125$
$0.39 < \rangle \leq 0.68$	$-0.1748\cdot\rangle^3 - 0.2697\cdot\rangle^2 + 0.356\cdot\rangle + 0.0512$
$0.68 < \rangle \leq 0.96$	$-1.9519\cdot\rangle^3 + 4.6054\cdot\rangle^2 - 3.8156\cdot\rangle + 1.1933$
$0.96 < \rangle \leq 1.03$	$-99.314\cdot\rangle^3 + 301.62\cdot\rangle^2 - 305.22\cdot\rangle + 102.95$
$1.03 < \rangle \leq 1.50$	$-0.3401\cdot\rangle^4 + 2.0442\cdot\rangle^3 - 4.5335\cdot\rangle^2 + 4.4731\cdot\rangle - 1.6063$

Table 5.4: Parametrizations of the diffuse fraction for distances between solar azimuth, SA and dome azimuth, DA in the interval: |60.3°| < SA-DA < |74.7°|. These are also plotted in Figure 5.2.

|60.3°| < SA-DA < |74.7°|	
$0 \leq \rangle \leq 0.40$	$-0.0133\cdot\rangle^2 + 0.0029\cdot\rangle + 0.125$
$0.40 < \rangle \leq 0.70$	$-0.3375\cdot\rangle^2 + 0.2527\cdot\rangle + 0.0765$
$0.70 < \rangle \leq 0.90$	$-0.1841\cdot\rangle + 0.2168$

$0.90 < \rangle \leq 1.03$	$29.283\cdot\rangle^3 - 83.006\cdot\rangle^2 + 78.136\cdot\rangle - 24.385$
$1.03 < \rangle \leq 1.50$	$-0.2018\cdot\rangle^4 + 1.2487\cdot\rangle^3 - 2.8549\cdot\rangle^2 + 2.9064\cdot\rangle - 1.0705$

Table 5.5: Parametrizations of the diffuse fraction for distances between solar azimuth, SA and dome azimuth, DA in the interval: |74.7°| ≤ SA-DA ≤ |180°|. These are also plotted in Figure 5.3.

$\lvert 74.7° \rvert \leq$ SA-DA $\leq \lvert 180° \rvert$	
$0 \leq \rangle \leq 0.73$	$-0.1347\cdot\rangle^2 + 0.0114\cdot\rangle + 0.125$
$0.73 < \rangle \leq 0.96$	$-0.1606\cdot\rangle + 0.1788$
$0.96 < \rangle \leq 1.03$	$1.9073\cdot\rangle^2 - 3.8228\cdot\rangle + 1.9369$
$1.03 < \rangle \leq 1.50$	$-0.0637\cdot\rangle^4 + 0.4654\cdot\rangle^3 - 1.2047\cdot\rangle^2 + 1.3684\cdot\rangle - 0.5455$

5.3 Conclusion

16 pyranometers have been installed at the climate station at DTU Byg in Lyngby Denmark. By means of half ball domes with different opening areas that cover different parts of the entire sky dome, the pyranometers receive horizontal solar irradiance from 16 different parts of the entire sky dome.

By means of the fractional measurements, parametrizations have been derived for the horizontal diffuse solar irradiance from different parts of the entire sky.

The parametrizations represent the diffuse fraction given by the fractional horizontal diffuse irradiance over the GHI as function of the clear sky index. The mathematical equations are valid for different intervals of the distance between the solar azimuth angle and the dome center azimuth angle.

The results have been implemented in the Danish Design Reference Year, DRY.

6. Satellite-derived irradiances

6.1 Introduction

Satellite-derived irradiances in recent years have become a main source of solar resource data. In particular it is used to assess the global horizontal irradiance (GHI) resource. Satellite-derived irradiances can be obtained from several sources. An overview of these sources can be found in Chapter 5 of the Task 46 midterm report by Sengupta et al. (2015). These sources have a wide range of quality and should not be used uncritically! In particular, the challenges of 3-D cloud effects, detailed in section 3.6, are a problem for satellite-derived irradiances. For geostationary satellite data such as the images from the SEVIRI multi-spectral camera on the Meteosat Second Generation (MSG) satellite the challenges are particularly large as the pixels in the images are 3x3 km^2 at the sub-satellite point on the Equator and even larger at higher latitudes. In Denmark each pixel covers an area of almost 50 km^2. Thus, it is impossible to evaluate the effect or 3-D cloud variability directly from such images. These effects need to be evaluated empirically by integrating ground-based irradiance measurements with the satellite-derived data. Site-adaptation methods for doing this are being developed currently as described in the report and journal article by Polo et al. (2015; 2016). A main point made by Polo et al. (2016) is that at least 1 year of good quality ground-based data is needed to site-adapt satellite-derived irradiances. 2 years of data is preferable, as this further reduces the uncertainty in the satellite-derived data.

6.2 Data

Since March 2012 satellite-derive irradiances have been produced at DMI. The data are produced every 15 minutes for a domain that covers NW-Europe. The domain is shown in Fig. 6.1.

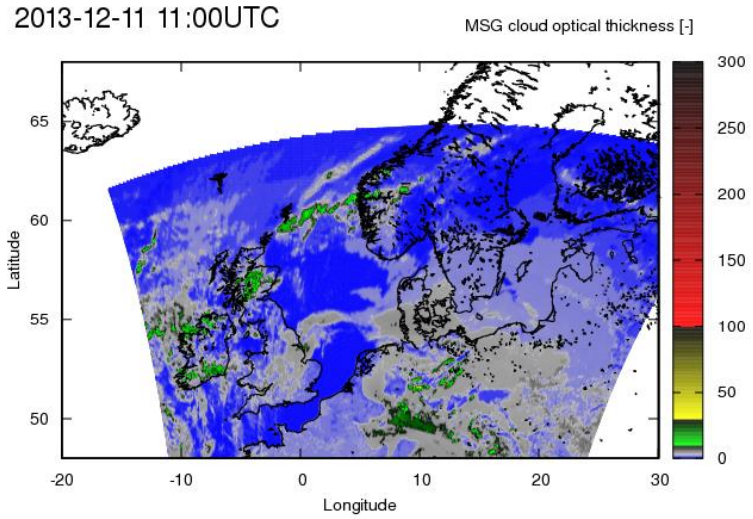

Figure 6.1: Example of retrieved optical thicknesses over NW-Europa from the 11th of December 2013.

Extensive forward radiative transfer simulations of cloud physical properties are combined with *a priori* estimates of the surface albedo. The forward radiative transfer simulations are performed with the Discrete Ordinate Radiative Transfer (DISORT) model (Stamnes et al. 1988; Dahlback & Stamnes 1991; Mayer & Kylling 2005). These are used to retrieve the atmospheric cloud water load and the average cloud particle effective radii from which the cloud optical thickness (Fig. 6.1) can be calculated. Given the cloud optical thickness the effect of clouds on the GHI and DrNI resource can be assessed.

The algorithm for satellite retrievals is especially designed so that it works at both at high solar zenith angles, i.e. down to when the sun is only 2 degrees above the horizon, and low satellite viewing angles. Thus, the Faroe Islands at 62°N are covered even in the middle of December as shown in Fig. 6.1.

The cloud data are available since April 26th 2012.

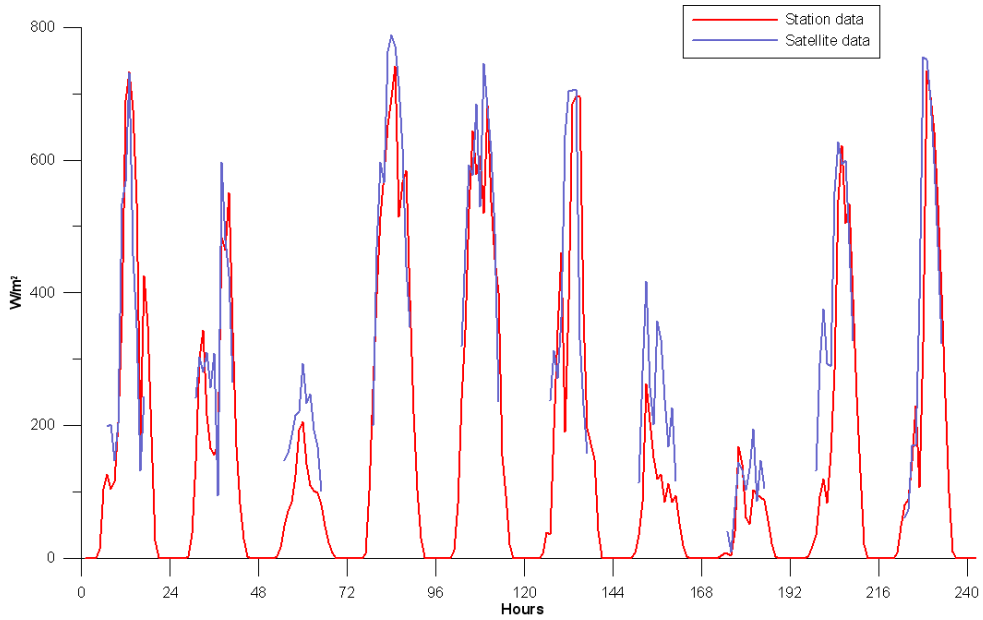

Figure 6.2: Comparison of satellite-derived global horizontal irradiances (GHI) from March for the station WMO 06069 in Foulum in Central Jutland.

In Fig. 6.2 a comparison of GHI retrieved from the satellite cloud data and GHI measured at one of DMI's meteorological stations is shown. The satellite-derived data shown here have not been site-adapted.

6.3 Specific challenges with satellite-derived irradiances

Besides general challenges with satellite-derived irradiances, several specific issues exist. One of these is the parallax effect, where a tall cloud appears to be in a different position than it actually is due to the satellite sun viewing geometry. At low solar angles tall clouds will also cast shadows on lower clouds. An example of this is shown in Figs. 6.3 and 6.4. Such errors cannot be corrected with site-adaptation, but will give intermittent errors in satellite-derived irradiance products.

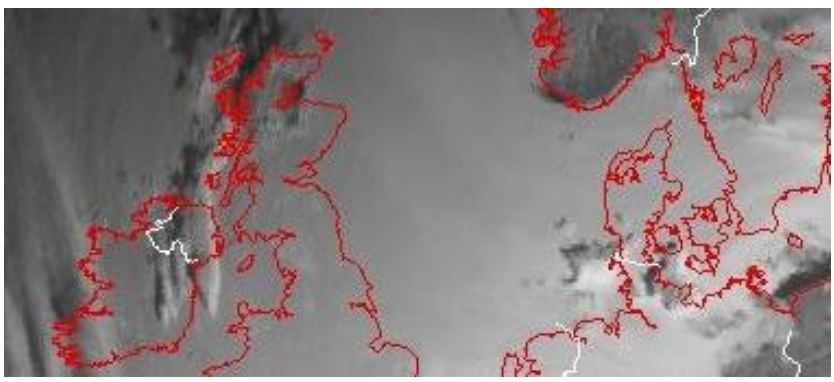

Figure 6.3: Taller clouds casting shadows over lower lying stratus clouds in the morning.

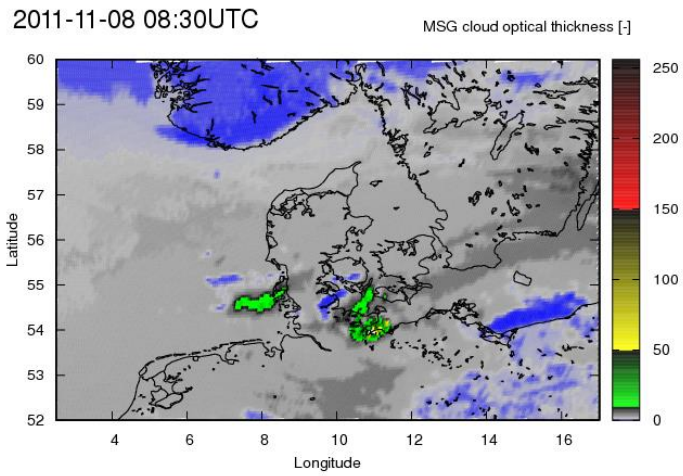

Figure 6.4: Cloud optical thickness derived from the satellite image shown in Fig. 6.3. The lower lying shaded clouds are shown as being cloud free (blue color), which is incorrect.

Freshly fallen snow on the ground below clouds cannot be recognized from satellite images. This will give an error of clouds that appear to be too optically thick. In clear sky conditions, the snow can be recognized in the images. When it is known that snow is on the ground, however, it is possible to correct for this effect. Thus, this is a temporary error.

6.4 Conclusion

DMI has performed retrievals of cloud properties from MSG SEVIRI satellite images and derived irradiances from these since 2012. Examination of these data has shown several quality issues. Satellite-derived irradiances should not be seen as a replacement of ground-based irradiance measurement, which are still essential for proper solar resource assessment!

6.5 References

Dahlback, A. and K. Stamnes. A new spherical model for computing the radiation field available for photolysis and heating at twilight, Planet. Space Sci., 39, 671–683, 1991

Gleeson, E., K. P. Nielsen, V. Toll, L. Rontu and E. Whelan. Shortwave Radiation Experiments in HARMONIE. Tests of the cloud inhomogeneity factor and a new cloud liquid optical property scheme compared to observations, ALADIN-HIRLAM Newsletter, 5, 92-106, 2015.

Mayer, B. and A. Kylling. Technical note: The libRadtran software package for radiative transfer calculations – description and examples of use, Atmos. Chem. Phys., 5, 1855–1877, doi:10.5194/acp-5-1855-2005, 2005.

Polo, J., S. Wilbert, J. A. Ruiz-Arias, R. Meyer, C. Gueymard, M. Šúri, L. Martín, T. Mieslinger, P. Blanc, I. Grant, J. Boland, P. Ineichen, J. Remund, R. Escobar, A. Troccoli, M. Sengupta, K. P. Nielsen, D. Renne and N. Geuder. Integration of ground measurements to model-derived data. IEA Report from SHC Task 46: Solar Resource Assessment and Forecasting, 2015.

Polo, J., S. Wilbert, J. A. Ruiz-Arias, R. Meyer, C. Gueymard, M. Šúri, L. Martín, T. Mieslinger, P. Blanc, I. Grant, J. Boland, P. Ineichen, J. Remund, R. Escobar, A. Troccoli, M. Sengupta, K. P. Nielsen, D. Renne, N. Geuder and T. Cebecauer. Preliminary survey on site-adaptation techniques for satellite-derived and reanalysis solar radiation datasets. Solar Energy, 132, 25-37, 2016.

Sengupta, M., A. Habte, S. Kurtz, A. Dobos, S. Wilbert, E. Lorenz, T. Stoffel, D. Renné, D. Myers, S. Wilcox, P. Blanc and R. Perez. Best Practices Handbook for the Collection and Use of

Solar Resource Data for Solar Energy Applications, Technical Report NREL/TP-5D00-63112, National Renewable Energy Laboratories, Golden, CO 80101, USA, 2015.

Stamnes, K.,S.-C. Tsay, W. Wiscombe and K. Jayaweera. Numerically stable algorithm for discrete-ordinate-method radiative transfer in multiple scattering and emitting layered media, Appl. Optics, 27, 2502–2509, 1988.

7. Verification of numerical weather prediction forecasts of global irradiance

We have focused both on benchmarking the general numerical weather prediction (NWP) models of DMI and on benchmarking specialized weather prediction models. In particular, two specialized NWP models have been tested. The first is a rapid-update cycle (RUC) model (Korsholm et al. 2014) in which both satellite cloud data and radar data are assimilated. The assimilation is done to secure a balanced initial state for the start of the NWP forecast, i.e. that the clouds added to the initial state of the model are not immediately removed when the model is integrated forward in time. Radar data shows the presence of precipitating clouds. This is used to assimilate convective clouds in the RUC model (Korsholm et al. 2014).

The second specialized type NWP models tested are ensemble models. Ensemble models contain several models run in parallel forecast relevant in this project is the DMI HIRLAM ensemble model, which has 25 members, which are all slightly different or perturbed with respect to each other. Thus, the ensemble can provide an estimate of the uncertainty of a given forecast.

7.1 Use of satellite-derived data for improving weather prediction forecasts

The RADAR RUC mesoscale model is optimized for intra-day forecast horizons (2-24 hours). An example of irradiance forecasts with this model is given in Fig. 7.1. The RUC model is run once every hour and is set up to provide irradiance output at a 10 minute resolution rather than the normal hourly resolution of NWP model irradiance output. The horizontal resolution of the model is 3.3 km.

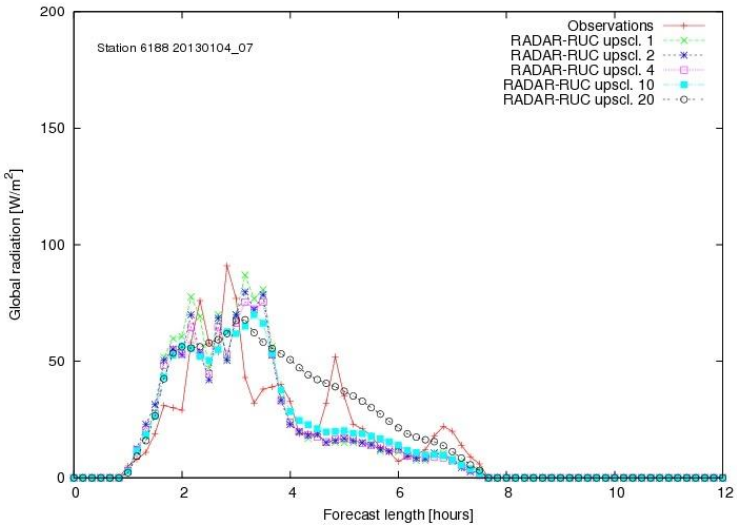

Figure 7.1: Example of irradiance forecasts with the DMI RADAR RUC model in comparison to measurements. The forecast is here compared to observations at the WMO station 6188 (red curve) at 5 different levels of upscaling: Nearest model grid point (green curve), average of 2x2 nearest grid points (blue curve), average of 4x4 nearest grid points (magenta curve), average of 10x10 nearest grid points (cyan curve), average of 20x20 nearest grid points (black curve).

As can be seen in Fig. 7.1 the RUC model without upscaling (the green curve) catches some sub-hourly variability but does not has the same level of variability as the observations. This is a general feature also seen on other variable days. It can also be seen that the variability is smoothened out with increasing levels of upscaling, but that the upscaled forecasts tend to better represent the averages of the observed global radiation. This is also a general feature

and is shown in greater detail in section 7.3. The point of the upscaling is that it is practically impossible to forecast the exact positions of individual clouds several hours ahead. An NWP model may, however, often make good estimates of the spatial distribution of clouds and the frequency of these. Thus, it is reasonable to expect that the upscaled forecast will provide a better average forecast, while the not-upscaled forecast will provide a better forecast of the variability. Depending on the purpose of the forecast, both these can be of importance.

7.2 Ensemble NWP forecasts

A snap shot of the ensemble models run at DMI in 2014 is shown in Fig. 7.2. Here "S05" is a 25-member ensemble prediction system based on the High Resolution Limited Area Model (HIRLAM) 7.3 NWP model. The S05 domain has a resolution of 0.05° (or 5.5 km).

Furthermore, DMI has added HIRLAM and the Integrated Forecast System (IFS) from the GLAMEPS (Grand Limited Area Model Ensemble Prediction System) ensemble to the models tested in the IEA SHC Task benchmarking exercise (Lorenz et al. 2016). GLAMEPS is a multi-model ensemble system that includes ensemble models from the HIRLAM-ALADIN consortium and ECMWF. The resolution of GLAMEPS is 0.15° in rotated latitudinal/longitudinal coordinates. Average GHI is output every 3-hours. The GLAMEPS domain can be seen in Fig. 7.2 together with the other DMI ensemble domains. From the other ensemble domains of DMI both GHI and DfHI are output every hour. The RUC model described in section 7.1 is not shown in the figure, but is slightly smaller than the S05 domain.

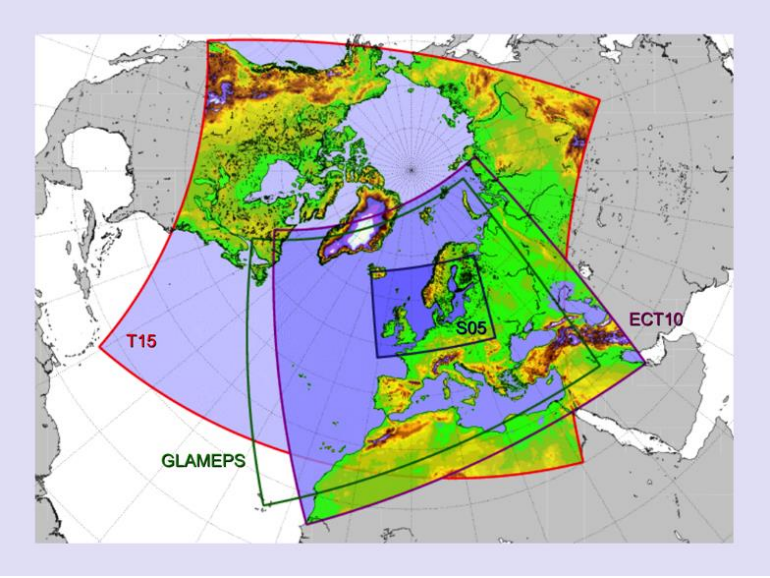

Figure 7.2: Ensemble domains run by DMI in 2014. S05 is a 5 km resolution domain with 25 HIRLAM model members. GLAMEPS is a European ensemble model with 15 km resolution with 26 HIRLAM model members and 15 IFS model members. ECT10 and T15 have not been considered in this project.

Before this project stated the HIRLAM 7.3 S05 ensemble model was tested at DMI for the period from 2011-Aug-05 to 2011-Nov-12. The analysis of the data was done by Dr. Sisse Camilla Lundholm. The GHI output data are tested against measurements from the 28 Danish pyranometer stations. The locations of these stations are shown in Fig. 7.3. The results based on forecast lead times of 2-54 hours showed that the root mean square error (RMSE) were reduced by 15%-20% in the ensemble mean forecast as compared to the control forecast.

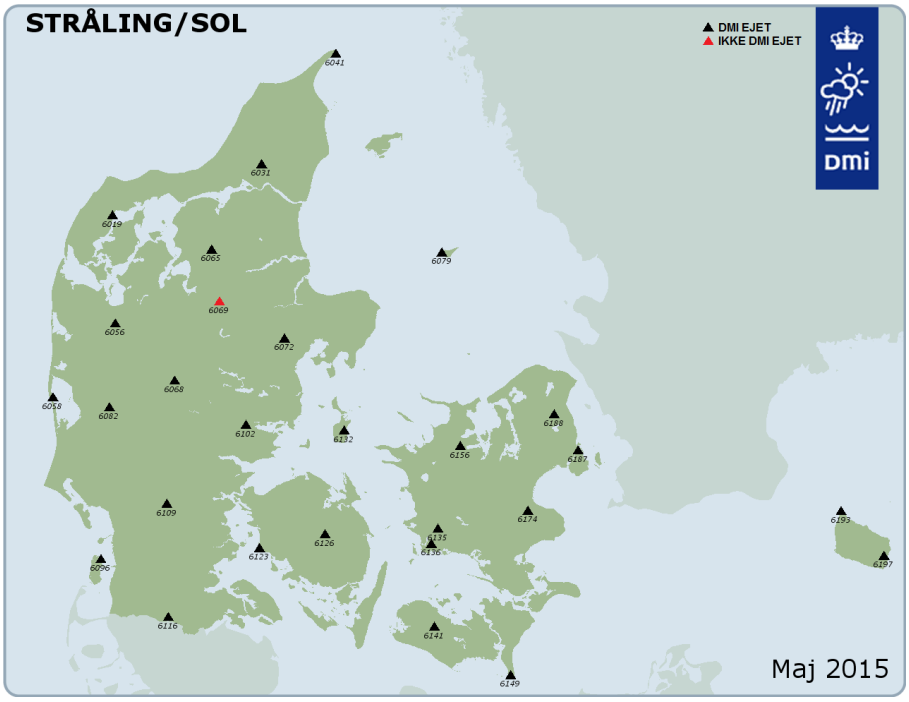

Figure 7.3: The locations of the 28 Danish global radiation stations used by DMI as of May 2015. DMI uses Schenk Star Type 8106 pyranometers to measure global radiation.

7.3 International benchmarking study

In subtask C of Task 46 the main collaborative work has been a benchmarking study of several global and limited area weather models during the 1 year period from March 2013 to February 2014. The benchmarking is done to quantify the typical errors of both NWP models and other types of forecasting methods. Also the benchmarking shows which methods are optimal to use for which forecasting horizons. Briefly summarized extrapolated all-sky camera images give the best forecasts on the minute scale, extrapolated satellite images give the best forecasts on the hourly scale, and NWP models give the best forecasts from a few hours to a few days ahead. Additionally, statistical corrections and combinations of several forecasting methods and models improve the forecasting quality. DMI has only worked with the NWP forecasts. The other forecasting methods are described the report by Sengupta et al. (2015). The NWP benchmarking results are described in the paper by Lorenz et al. (2016). Below a summary of these results is given and specific Danish results that are not included in the paper are shown.

The main conclusion is that the global IFS NWP model of ECMWF gives the lowest root mean square errors (RMSE) in the GHI forecasts for forecast horizons of 7 hours and longer ahead (Lorenz et al. 2016). The IFS model in 2013 and 2014 had a resolution of 15 km. This conclusion also holds when higher resolution models are upscaled to the IFS resolution. If bias corrections to both the IFS model and the 3 km resolution HIRLAM model of DMI, the HIRLAM model has a better GHI forecast than IFS in terms of RMSE. A comparison of ECMWF IFS and HIRLAM SKA forecasts is shown in Fig. 7.4. This is performed for 18 measurement stations in Germany. The focus in was on the effect of different bias correction approaches. When applying spatial and temporal averaging as well as a bias correction in dependence of the solar zenith angle and the clear sky index, SKA forecasts show smaller RMSE values than the IFS forecast with the same bias correction. For IFS forecasts the impact the investigated bias correction schemes is only small with improvement of up to 7.8 % for regional forecasts, while there is a larger improvement for the HIRLAM SKA forecasts around 25% for the regional forecasts (Sengupta et al. 2015).

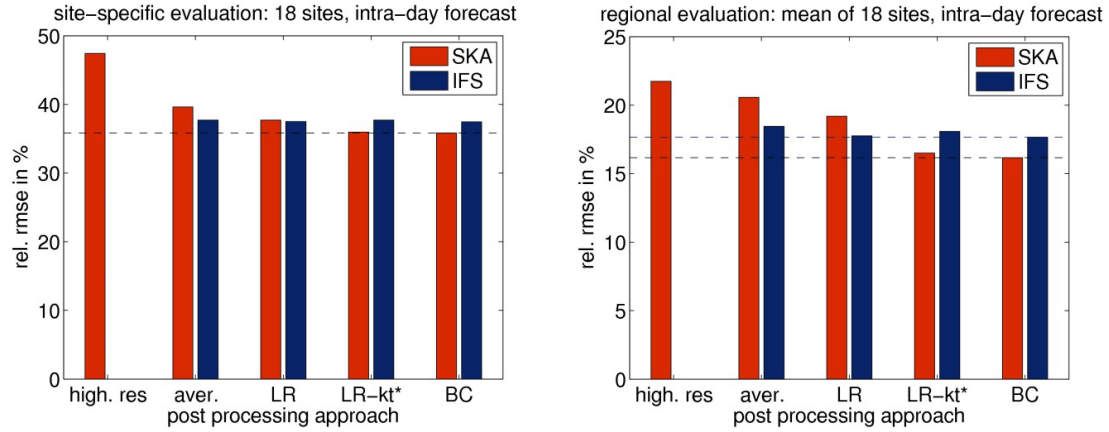

Figure 7.4: Relative RMSE of HIRLAM SKA (red) and ECMWF IFS (blue) forecasts with different bias correction approaches. "high. res." is here the uncorrected HIRLAM forecasts, "aver." is spatial and temporal averaging, LR is linear regression of GHI, LR-kt* is linear regression of the clear sky index, and BC is a method of bias correction where both the solar zenith angle and the clear sky index. The left plot shows relative RMSEs for single site forecasts. The right plot shows the same for regional forecasts, derived as the mean value of all station in a given region of Germany. Database: 18 sites in Germany, 3.4.2013- 28.2.2014 (Training set: last 30 days, all sites). This figure is from the Sengupta et al. (2015) report.

More NWP models were included in the comparison including COSMO-EU of the German Weather Service (DWD), RADAR RUC of DMI, and GLAMEPS. Meteotest also ran a bias corrected version of the global GFS NWP model (GFS-MOS). The latter is included in Fig. 7.5 but cannot be directly compared to the other models in this figure, as they are without bias correction. Fig. 7.5 shows the benchmarking results for Germany. Ignoring GFS-MOS, it is seen that IFS has the lowest RMSE for all forecast horizons despite having a bias that the other NWP models tests. It can also be seen that the RMSEs increase faster as a function of the forecast horizon for the higher resolution models (COSMO and HIRLAM) than for the IFS model.

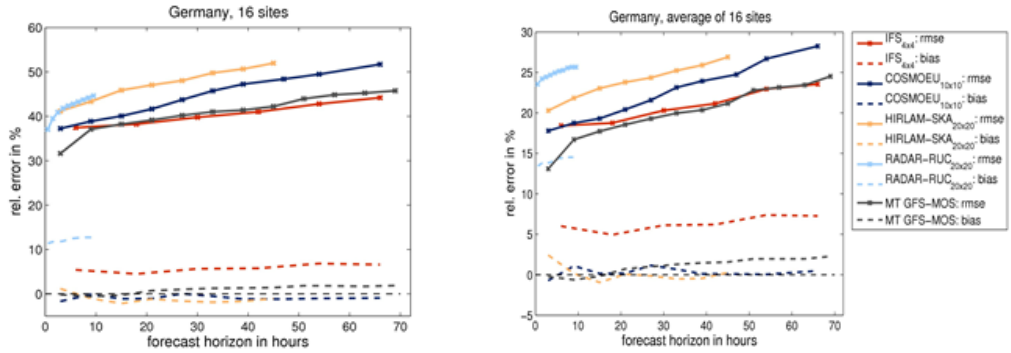

Fig. 7.5: Relative RMSEs (solid lines) and relative biases (dashed lines) of GHI forecasts for different NWP forecast models as a function of the forecast horizon. The left plot shows single station statistics. The right plot shows the average statistic for GHI from all 16 German stations. All the forecasts here are upscaled to cover an area of approx. 60 km x 60 km. The figure has been made by Lorenz et al. (2016).

In Fig. 7.6 the yearly averaged benchmarking results for Denmark are shown. 25 of 28 GHI stations have been used, with 3 stations excluded due to quality issues. The results are similar to the results for Germany (fig. 7.5) with the IFS NWP model having the lowest RMSE. Here the results from the GLAMEPS (ensemble) model are also included. Surprisingly, the average of these has higher RMSE than the deterministic IFS model.

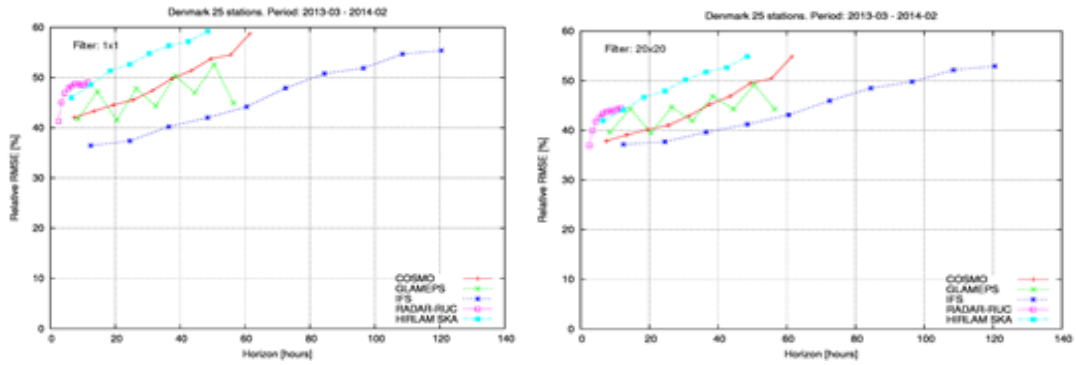

Fig. 7.6: Relative RMSE of GHI forecasts for different NWP models as a function of the forecast horizon. In the left plot no upscaling is made for the forecasts. In the right plot the forecasts have been averages over 20x20 grid points for all models.

The RUC model can be compared with the HIRLAM SKA model, since both are based on the same model. It is clear that a significant improvement occurs in the RUC forecast for forecast horizons until 5-6 ahead. After this the statistics for the two model versions are similar.

Both the RUC model and the HIRLAM SKA model are better at forecasting the intra-daily variability of GHI than IFS and COSMO-EU (Lorenz et al. 2016).

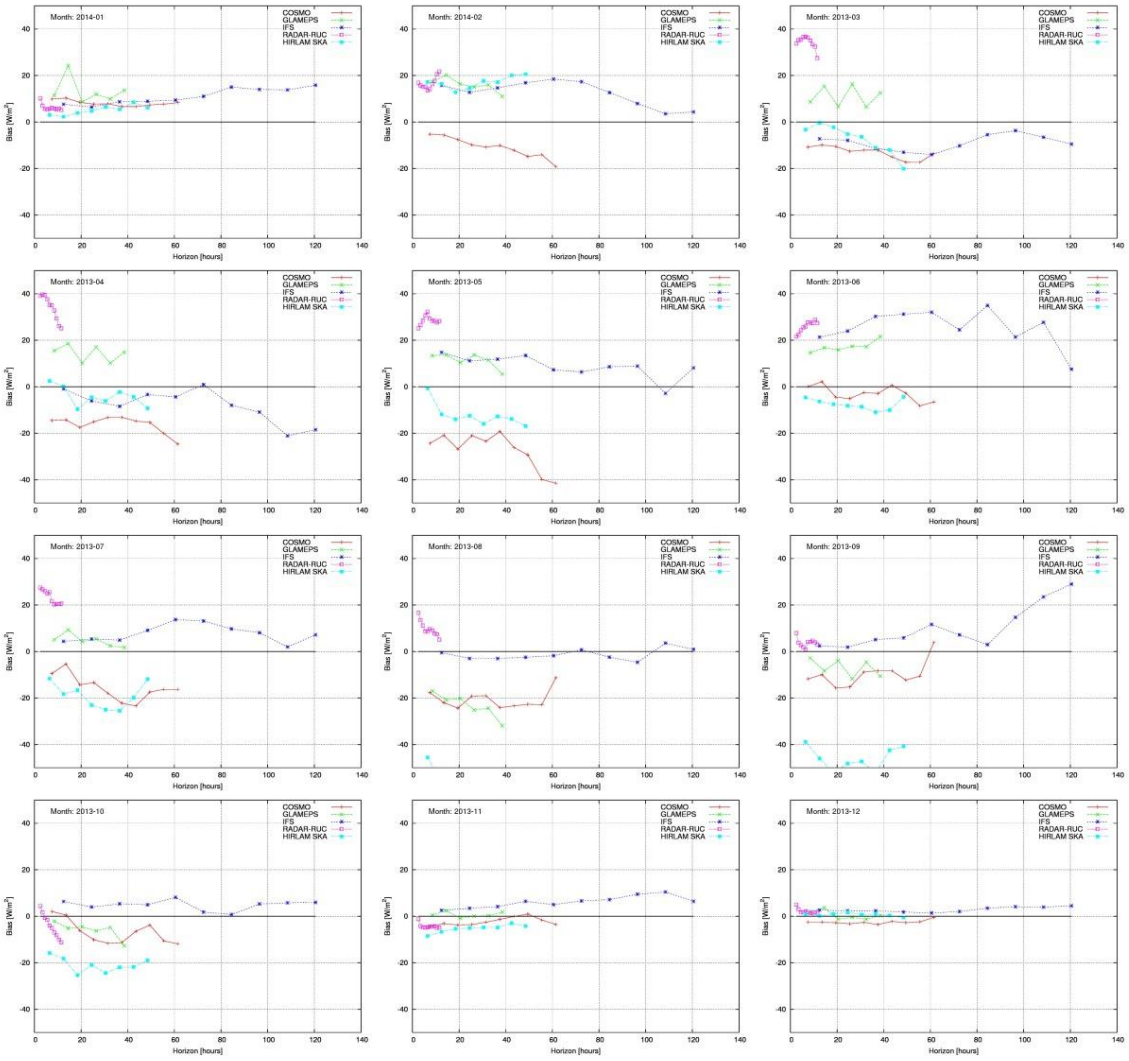

Fig. 7.7: Average GHI monthly biases in W/m^2 as a function of forecast horizon for the Danish GHI stations (Fig. 7.3) for the models: COSMO-EU (red curves), GLAMEPS (green curves), IFS (blue curves), RADAR-RUC (magenta curves) and HIRLAM SKA (cyan curves). The 12 subplots show the months from January (upper left) to December (lower right) from the test period.

In Fig. 7.7 the biases of the tested NWP models for each month from the period from March 2013 to February 2014 are shown. This DMI specific result is not included in the Task 46 report (Sengupta et al. 2015) or the Task 46 NWP benchmarking paper (Lorenz et al. 2016). It shows how the modelled GHI bias varies from month to month and how one model may have the lowest GHI bias during one month, but another model have it during another month. Thus, HIRLAM SKA had the lowest GHI bias in March 2013, COSMO-EU in June 2013 and IFS in August 2013. For the advanced model output user, this is an important feature of the model error statistics to keep in mind.

7.4 Recommendations for how to use NWP GHI forecasts

- If only one NWP forecast model is chosen, the global IFS model should be chosen. In Denmark this model is managed by DMI. In particular if only regional (e.g. DK1 & DK2) forecasts are required.
- For local variability forecasts a high resolution NWP model (1-3 km resolution) should be used. For forecasts from 3 to 6 hours ahead, the DMI RUC model is recommended.
- For forecasts shorter than 3 hours satellite image extrapolation gives the most accurate forecasts (Sengupta et al. 2015).
- For forecasts shorter than 30 minutes all sky camera image extrapolation gives the most accurate forecasts (Sengupta et al. 2015).
- The expert user should combine several NWP forecast models and weigh them according to their performance in the latest month. As illustrated in Fig. 7.7 temporally developing statistical corrections on a per NWP model basis should also be used for the optimized GHI forecasts.

7.5 References

Korsholm, U. S., Petersen, C., Sass, B. H., Nielsen, N. W., Jensen, D. G., Olsen, B. T., Gill, R. and Vedel, H. A new approach for assimilation of 2D radar precipitation in a high-resolution NWP model, Meteorol. Appl., DOI: 10.1002/met.1466, 2014.

Lorenz, E., Kühnert, J., Heinemann, D., Nielsen, K. P., Remund, J., and Müller, S. C. Comparison of global horizontal irradiance forecasts based on numerical weather prediction models with different spatio‐temporal resolutions. Progress in Photovoltaics: Research and Applications, 2016.

Lundholm, S. C. Verification of Global Radiation Forecasts from the Ensemble Prediction System at DMI, PhD Thesis, University of Copenhagen, Denmark, 2013.

Sengupta, M., A. Habte, S. Kurtz, A. Dobos, S. Wilbert, E. Lorenz, T. Stoffel, D. Renné, D. Myers, S. Wilcox, P. Blanc and R. Perez. Best Practices Handbook for the Collection and Use of Solar Resource Data for Solar Energy Applications, Technical Report NREL/TP-5D00-63112, National Renewable Energy Laboratories, Golden, CO 80101, USA, 2015.